Perpendicular Anisotropy in Heusler Alloy Thin Films for CPP-GMR Devices

William Frost

Doctor of Philosophy

University of York
Electronic Engineering

August 2018

Abstract

Heusler alloys are a class of materials with some of the greatest potential for the advancement of magnetic recording and memory. Their combination of high magnetisations, Curie temperatures and spin polarisations make them ideal for device applications. However perpendicular anisotropy is difficult to achieve in GMR devices as an interface with an oxide is required. To develop these materials for GMR application the perpendicular anisotropy must be induced in other ways.

In this work polycrystalline Co_2FeSi and $Co_2FeAl_{0.5}Si_{0.5}$ Heusler alloys have been deposited on body-centred cubic seed layers of vanadium and tungsten. Their magnetic and crystallographic properties have been measured and quantified using a range of techniques, significantly mangnetometry and X-ray diffractometry. With the use of vanadium seed layers Co_2FeSi was deposited with a strong {110} texture out-of-plane, ideal for the crystallisation of the material. In Co_2FeSi layers <5 nm thick perpendicular anisotropy is induced by strain at the interface with vanadium. This is further enhanced by the addition of a top layer of vanadium, doubling the interface area and increasing the anisotropy.

When tungsten seed layers are used instead there is a significant increase in the perpendicular anisotropy of Co_2FeSi. This anisotropy is maintained in films with thicknesses up to and beyond 12.5 nm. When incorporated into GMR stacks both Co_2FeSi and $Co_2FeAl_{0.5}Si_{0.5}$ are found to exhibit layer thickness dependent switching, ideal for device application. The heating of the film pre-deposition is found to heavily influence the structure and anisotropy of the samples, even at modest temperatures <70 °C for less than two minutes. GMR devices were fabricated and a proof of principle for a perpendicular CPP-GMR device based on Heusler alloys presented.

Contents

List of Tables

List of Figures

Acknowledgements

A Ph.D. is a long and laborious process, that would be impossible without the guidance and support of others. To this end I would like to express my sincere gratitude to my supervisor, Professor Atsufumi Hirohata, for all of his help and for pushing me in the right direction. I would also like to thank Professor Kevin O'Grady for his constant support; technical, scientific and personal. Of course a very special thanks to my parents for support on all levels.

There are too many to name individually but a sincere thanks to all the members of the Magnetic Materials Group with whom I have shared A/O/12. Without them it would have been a very dull experience. A special mention to John Sinclair for putting up with me for four solid years. Also to Dr. Marjan Samiepour for her technical help and for fabricating the devices used in this work. Good luck to all future members!

Finally I would like to thank Gabriel McCafferty and Marcus Ormston at Seagate Technology, Derry. Firstly for the financial support offered by Seagate but secondly, and more importantly, for the fruitful discussions and guidance in my Ph.D.

Author Declaration

I declare that this thesis is a presentation of original work and I am the sole author. This work has not previously been submitted for an award at this, or any other, University. All sources are acknowledged as References.

List of Publications

1. W. Frost & A. Hirohata, *Perpendicular Anisotropy in Heusler Alloy Layers induced by a V Seed Layer*, *IEEE Trans. Magn.*, **52** (7), 2-5 (2016)

2. C.N.T. Yu, A. Vick, N. Inami, K. Ono, W. Frost & A. Hirohata, *Exchange Bias Induced at a $Co_2FeAl_{0.5}Si_{0.5}$/Cr Interface*, *J. Phys. D. App. Phys.*, **50**(12), 125004 (2017)

3. W. Frost & A. Hirohata, *Heusler Alloys with bcc Tungsten Seed Layers for GMR Junctions*, *J. Magn. Magn. Mater*, **453**, 182-185 (2018)

4. A. Hirohata, W. Frost, M. Samiepour & J.Y. Kim, *Perpendicular Magnetic Anisotropy in Heusler Alloy Films and Their Magnetoresistive Junctions*, *Materials*, **11**(1), 105 (2018)

1 Introduction

The very first spin sensitive measurements were undertaken by William Thomson, Baron Kelvin, in 1857 when he observed the effects of anisotropic magnetoresistance (AMR) [1]. However Thomson's discovery that the resistivity of iron, and to a greater extent nickel, was dependent upon the angle of an applied field was mostly a curiosity.

This was the case until 1971 when Robert Hunt popularised the idea of a magnetoresistive transducer as a way to read tape [2]. Hunt even proposed two geometries for the device: a horizontal and a vertical arrangement. The available signal strength from a 2% MR head using permalloy was an easily measured 80 mV and required a bias voltage of 80 Oe, much lower than the coercivity of the film. This was also usable of a wide frequency range and the example data is shown in fig. 1.1.

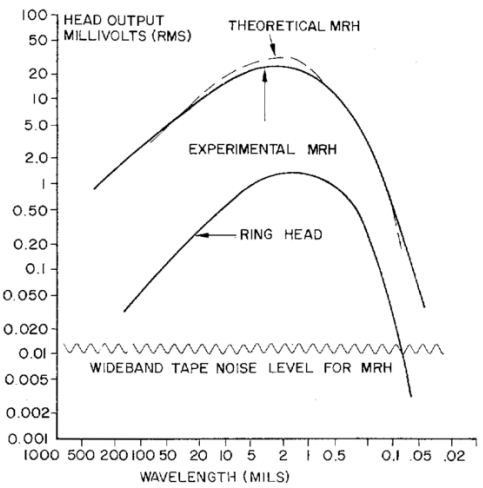

Figure 1.1: Frequency response MR of the first magnetoresistive readhead compared to a ring head [2].

MR sensors were quickly realised to have a range of advantages such as high sensitivity, wide frequency ranges up to MHz and diverse applications, for example as motion sensors, navigation devices and metal detection [3]. Honeywell have used this technology to develop navigational compasses with a resolution as low as 0.1° [4].

In 1990 IBM introduced the first magnetoresistive read head in a hard-disc drive (HDD). This innovation lead to a rapid increase in the areal density of HDDs and between 1990 and 1997 the rate of change was an annual increase of 60% [3]. Eventually a recording density increase was obtained from 1 Gbit/inch^2 to 5 Gbit/inch^2 [5–7]. At the same time as this the term "spintronics" was coined, describing the

addition of the spin degree of freedom to the traditional electronic current [8].

However spintronic research was truly galvanised by the independent discoveries of giant magnetoresistance (GMR) by the groups of Albert Fert and Petr Grünberg [9, 10], whereby alternating layers of ferro- and non-magnetic materials produce a large, field-dependent resistance as shown in fig. 1.2. The change in resistance was orders of magnitude greater than that observed in AMR and the significance of this discovery was acknowledged by the shared 2007 Nobel Prize in Physics.

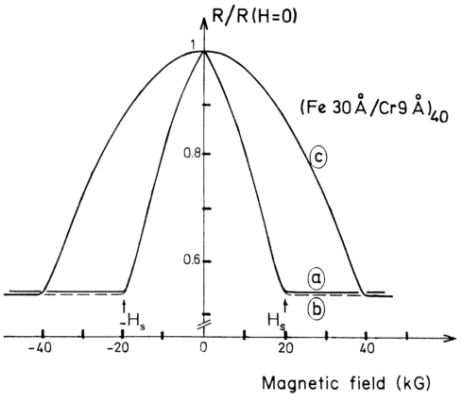

Figure 1.2: GMR data of the group of Albert Fert of a $[Fe/Cr]_{40}$ multilayer at 4 K [9].

The effect lead to the creation of the spin-valve, devices based upon the GMR effect so named for the spin-dependent transport that "flows" through them. These were further enhanced by Dieny et al. in 1990 when it was proposed to exchange-bias one of the layers in the stack, creating a "pinned layer" [11]. This prevents one of the layers reversing at all, so that a sensing layer, or "free" layer, is responsible for all of the field dependence.

GMR read-heads were quickly introduced into the world's hard-disc drives in 1997, once again by IBM. A 7% GMR was used to demonstrate 5 Gbit/inch^2 in 1996 [12] and further increasing GMR ratios lead to a rapid increase in areal density, with densities up to 15 Gbit/inch^2 achieved by the year 2000.

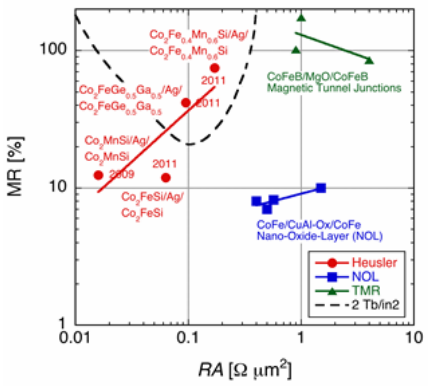

Figure 1.3: Balance of MR-ratio and resistance required to reach recording densities of 2 Tbit/inch^2 [15].

This remained the case until 2004 when the similar effect of tunnelling magnetoresistance (TMR) was incorporated into read-heads by Seagate Technology. Instead of a non-magnetic metallic layer between the ferromagnetic layers there is an insulating layer, typically of MgO [13]. This causes TMR to have a greater magnitude than a typical GMR ratio with records exceeding 200% [13] and as such allows for increased sensitivity in the read-head, leading to higher areal densities surpassing 1 Tbit/inch^2 by 2012 [14].

This increase in signal comes at a price, however. Due to the nature of the tunnel barrier the resistance of a TMR stack is intrinsically high at around $1\,\Omega/\mu m^2$, one order of magnitude greater than that typically found in a GMR device [15]. This limits the element size of the read-head to avoid Joule heating and therefore limits the areal density of the entire HDD. Figure 1.3 shows how the resistance of the device, denoted by its resistance-area product (*RA*), must be minimised while the MR is maximised in order to achieve $2\,\text{Tbit/inch}^2$ recording density [15]. The green symbols denote the devices using TMR and it is immediately clear that the *RA* is simply too high to achieve this goal. As such a switch back to GMR devices must be made.

1.1 Heusler Alloys

As shown in fig. 1.3 there are several options available to attempt to increase the GMR ratio to obtain high areal density. However the most promising, and thus far successful, option is the group of compounds known as Heusler alloys. The family of Heusler alloys traditionally consists of tertiary alloys formed from two transition metals, X and Y, and a third metalloid or non-metal element Z, as shown in fig. 1.4 [16]. Two sub-sets exist called full- and half-Heusler alloys with formulae X_2YZ and XYZ respectively.

These alloys crystallise in a series of complex face-centred cubic (fcc) lattices, ranging from a fully ordered $L2_1$ structure to a disordered $A2$ structure. Many of the desirable properties of the Heusler alloys are only obtained in one of these crystallographic states, not necessarily always the fully ordered one [16].

Ferromagnetic Heusler alloys have several important properties that make them ideal for application in future GMR technologies. Firstly they can have very high saturation moments, for example up to $1400\,\text{emu/cm}^3$ in Co_2FeSi [17]. This is vital as the value of a GMR ratio is directly proportional to the magnetisation in the two layers [18]. Secondly they are extremely thermally stable with high Curie temperatures T_C, meaning that they can survive the heat produced in standard hard dives easily which is around 75 °C. This can be extended into other GMR sensor applications, for example in vehicles, where temperatures can reach 100s of Kelvin, since Co_2FeSi has T_C >900 K [17].

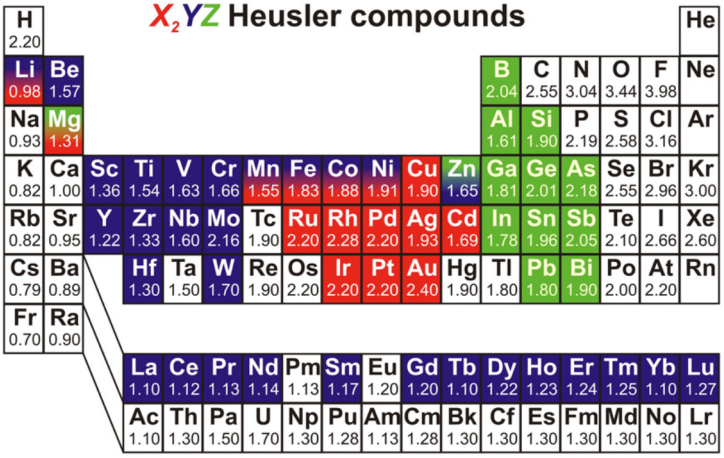

Figure 1.4: The elements that make up the tertiary, full-Heusler compounds [16].

The most important property of some Heusler alloys is that of a theoretical 100% spin polarisation at the Fermi level [19]. All ferromagnetic materials exhibit a spin imbalance at the Fermi energy. However in some rare cases this spin imbalance can be 100%, i.e. the minority spin band is completely empty creating a band gap. Such materials are referred to as half-metals, since one spin band is metallic while the other is semi-conducting or insulating. Many Heusler alloys are predicted to be half-metals, for example Co_2FeSi, $Co_2FeAl_{0.5}Si_{0.5}$ and Co_2MnSi [16, 19]. This gap is created by hybridisation of the atomic orbitals in the material of the *X-Y* and *X-X* atoms, shifting the energy levels asymmetrically in the spin-up and spin-down density of states as shown for Co_2FeSi in fig. 1.5.

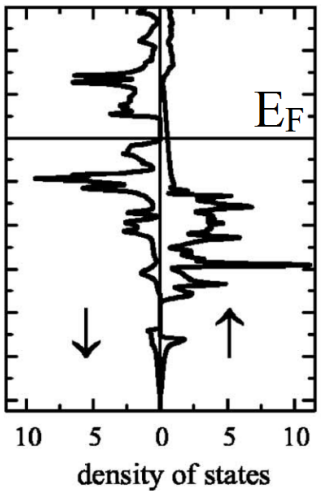

Figure 1.5: DoS for Co_2FeSi showing the minority band gap [17].

As shown in fig. 1.3 this combination of properties leads to some Heusler alloy GMR structures meeting the criteria for 2 Tbit/inch^2. However these films are not industrially compatible. They are often single-crystal films, grown via a slow process such as molecular beam epitaxy [20] or epitaxial films on expensive, single-crystal substrates likes MgO [21]. Alternatively the full crystallisation of the Heusler alloy requires annealing temperatures up to 1000 K. As such while these idealised structures meet the physical requirements for HDD areal density increase, they are not economically or mechanically viable.

It is therefore required to optimise Heusler alloy materials using sputtering growth techniques at low temperatures, ideally below 325 °C. This temperature

is the maximum to maintain the magnetic components of the read-head earlier in the process as well as for efficiency [22]. One possibility to achieve this is using seed layers, which has met with some success in the past for example with chromium/silver dual seed layers [23, 24].

Alternatively the GMR ratio can be improved using Heusler alloys that are not fully crystalline but can operate with perpendicular anisotropy. Perpendicular magnetic anisotropy increases the GMR ratio of a device but is difficult to achieve in Heusler alloys due to their cubic structure - they have no intrinsic anisotropy to exploit. Perpendicular anisotropy also improves the scalability of a device [25].

1.2 Heusler Alloys with Perpendicular Anisotropy

A single crystal, thin-film Heusler alloy sample will have a fourfold anisotropy in the plane of the sample due to its cubic structure [26]. However a perpendicular anisotropy can be induced in the sample by interfacing the Heusler alloy film with MgO [27], leading to anisotropy energy densities up to 4×10^6 ergs/cm^3 [28]. This is caused by the hybridisation of the oxygen p-orbitals with the d-orbitals of the X atom of the Heusler alloy [29]. However the presence of the oxide layer will always create a high resistance-area product,RA, above 1 $\Omega/\mu m^2$ compared to 10^{-2} $\Omega/\mu m^2$ in GMR devices, since it is used a tunnel barrier, and is therefore incompatible with a GMR device.

Previous work has shown that heavy metal interfaces can also induce a perpendicular anisotropy in CoFe, most likely due to the strong spin-orbit interactions in these metals [30, 31]. Therefore seed, spacer and capping layers of materials with high spin-orbit coupling such as platinum, tungsten or tantalum could be a simple route to perpendicular devices with Heusler alloys.

Additionally strain can be used to modify the crystallographic properties of a material to induce an anisotropy [32]. Many seed layers have already been used with Heusler alloys to improve texture and crystallinity such as silver [23, 33] and TiN [34]. However perpendicular anisotropy has only ever been obtained in extremely thin layers, for example 0.9 nm on TiN.

Due to the fcc crystal structure of Heusler alloys many fcc metallic seed layers have been employed. However the strain induced by a body-centred cubic (bcc) structure could be they key to obtaining perpendicular anisotropy. Therefore Heusler alloys with bcc metallic seed and capping layers have great potential to exhibit strong perpendicular anisotropy for application in GMR devices by exploiting these two phenomena [25].

Heusler alloys have been successfully incorporated in TMR junctions [35–37], including those with perpendicular anisotropy and TMR ratios up to 90% [25, 38]. Therefore perpendicular CPP-GMR devices must be highly competitive in terms of magnetoresistance and the resistance kept as low as possible to maximise the advantages offered by GMR. However many of the advantages of these TMR devices once again make use of high annealing temperatures and expensive substrates to create epitaxial, well-ordered Heusler alloy layers. Therefore there is even great potential for improvement in applicability if this level of performance can be obtained in polycrystalline TMR devices.

1.3 Other Applications

One of the seminal examples of GMR application is the alternative memory format magnetic random access memory (MRAM). Figure 1.6 shows an extended version of fig. 1.3 which includes the requirements for 1 Gbit and 10 Gbit MRAM. It is clear that 10 Gbit MRAM has already been realised with magnetic tunnel junctions (MTJs) with an in-plane magnetisation [39]. However, perpendicular anisotropy is required in MRAM cells for several reasons.

Perpendicular anisotropy in MRAM cells enables a faster switching time, vital for high-speed applications in computers [40, 41]. Heusler alloys are a perfect candidate for this orientation due to the low Gilbert damping term, with values below 0.002 [42]. As in perpendicular recording media, perpendicular orientation also reduces the stray field and therefore cross talk between MRAM bits. Perpendicular MTJs have therefore been able to achieve 1 Gbit MRAM as shown by the solid blue triangles in fig. 1.6 [29].

However this is still not capable of reaching the requirements for 10 Gbit MRAM due to the intrinsic high *RA* caused by the tunnel barrier. A low *RA* is required here for impedance matching to a transistor that is attached to one MRAM cell. There-

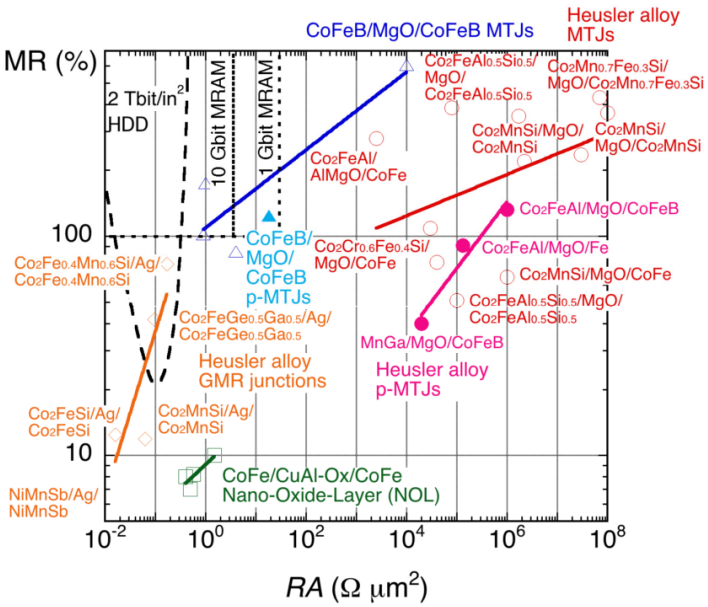

Figure 1.6: Current state-of-field for the potential structures to achieve high recording densities in HDDs and MRAM [25].

fore the high MR-ratio offered by half-metallic Heusler alloys implemented with perpendicular anisotropy makes for an ideal candidate for the future of MRAM.

1.4 Outline of the Thesis

The motivation for this project was primarily driven by the desire for low-*RA*, thermally-stable devices which do not sacrifice the properties that are enjoyed by MTJ devices currently in use. Heusler alloy devices with perpendicular anisotropy are an exciting prospect to realise this due to ideal combinations of material properties, availability and compatibility with current fabrication techniques.

In Chapter 2 the overarching physics that governs the behaviour of magnetic thin-films is discussed. This includes the origins of the hysteresis, magnetic domains and magnetic anisotropies. Chapter 3 then applies this to Heusler alloys while introducing this complex group of materials and the origins of their properties. How these properties are tested and developed is then discussed in chapter 4, where descriptions of and the physics of experimental techniques used in the thesis are presented.

The results of the development of a CPP-GMR device base on the Heusler alloy $Co_2FeAl_{0.5}Si_{0.5}$ are shown in chapters 5 and 6, culminating in the presentation of

a working perpendicular GMR device with a modest GMR ratio. These are divided into two chapters based on the seed layer used, namely vanadium and tungsten. Finally chapter 7 summarises the thesis and presents the future challenges for follow up work.

1.5 Note on Gaussian Units

Due to the nature of the work in this thesis, and how it relates to the recording industry, Gaussian-c.g.s. units have been used throughout. These are the industry standard for magnetic recording, and are therefore ubiquitous throughout the field of magnetism. However data reproduced from previous work may unavoidably be presented in S.I. units.

It also must be noted that the majority of magnetic measurements in this thesis were performed out-of-plane. This presents the issue of a demagnetising field with values up 10 kOe. Whilst in many systems this can be corrected for using a factor of $4\pi M$, where M is the magnetisation; the films in this work have an added intergranular exchange coupling field. As such loops cannot be accurately or reproducibly corrected for the demagnetising field. Hence all magnetic measurements presented in this thesis are given as function of the applied field , H_{app}.

Secondly it is often beneficial to plot normalised magnetic measurements, i.e. where the magnetisation of the film is normalised to its saturation. This allows for easy comparison of samples, especially for properties such as the loop squareness and reversal mechanisms. Magnetic measurements presented herein are therefore plotted on axes of $\frac{M}{M_S}$ vs H_{app}.

2 Magnetic and Electrical Properties of Thin Films

2.1 Magnetic Properties of Thin Films

In general thin magnetic films are in one of two forms. The first are epitaxial, single crystal materials deposited by slow, controlled methods such as molecular beam epitaxy (MBE) in ultra-high vacuum. The properties of these films strongly mimic those of the bulk material whereby magnetic domains form in order to minimise the magneto-static energy. As a single crystal is by definition extremely uniform, there are very few domain wall pins and therefore the domain walls move easily through the crystal. As such the hysteresis loop of the material is extremely square as shown in fig. 2.1.

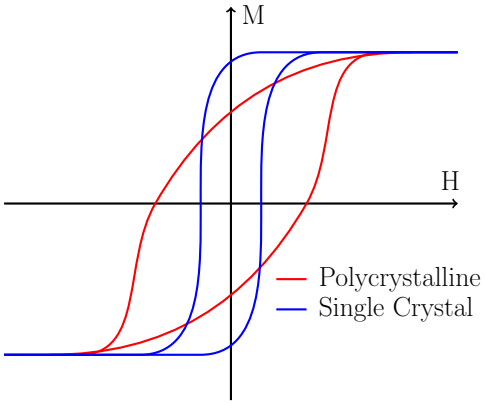

Figure 2.1: Schematic *M-H* loops for single and polycrystalline iron films demonstrating the increase in coercivity and the loss of loop squareness [43].

The second type of thin film are the more common polycrystalline thin films. While some elements of epitaxy may remain the magnetic properties become dominated by the granular nature of the film. In samples with large grains the domain walls now have a high density of pinning sites at grain boundaries. The squareness of the hysteresis loop is dramatically reduced as the propagation of the domain walls is limited while the coercivity is similarly increased as shown in fig. 2.1. At grain sizes of less than ~30 nm the grains act as single domain entities. In this regime the particles behave according to the Stoner-Wohlfarth theory.

In this work the films are sputter deposited with a median grain diameter <20 nm and as such discussion of thin film properties will be solely regarding polycrystalline samples with single domain grains.

2.1.1 Stoner-Wohlfarth Theory

The best understanding of magnetic hysteresis comes from the classic work of Stoner and Wohlfarth; often dubbed the Stoner-Wohlfarth theory [44]. The following discussion follows that of B.D. Cullity in *Introduction to Magnetic Materials* [45]. By treating a thin film as a plane of single domain particles with some anisotropy, this theory can be applied to the hysteretic processes in a thin film with small grains. The small grains criterion is vital as this determines that each of the grains act as a single magnetic entity with no internal domain wall. It is also imperative to note that this theory applies only at 0 K and temperature effects must be considered separately.

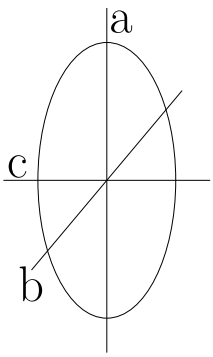

Figure 2.2: Prolate spheroid particle.

The simplest case to consider is that of an ellipsoid of revolution as shown in fig. 2.2, which has a long rotation axis a and two equivalent minor axes b and c. This includes the common particle shapes of spheroids, spheres and discs. When these particles are small enough to be single domain particles, magnetisation reversal can happen only by rotation. Due to the shape anisotropy the a axis is the easy axis. For any rotation to occur there will be an increase in magneto-static energy (E_{ms}) as the north and south poles of the particle must become closer together.

The aligned case is the simplest to consider, i.e. the applied field is parallel to a. No rotation will occur as the field is applied along the easy axis. Reversal will then only occur when the magneto-static energy from the applied field overcomes the anisotropy energy (E_K). When this point is reached all of the particles will reverse simultaneously with their atomic spins parallel, called coherent rotation. The applied field required to do this is the anisotropy field (H_K) which is given by

$$H_K = \frac{2K}{M_S} \tag{2.1}$$

where K is the anisotropy constant and M_S the saturation magnetisation. This

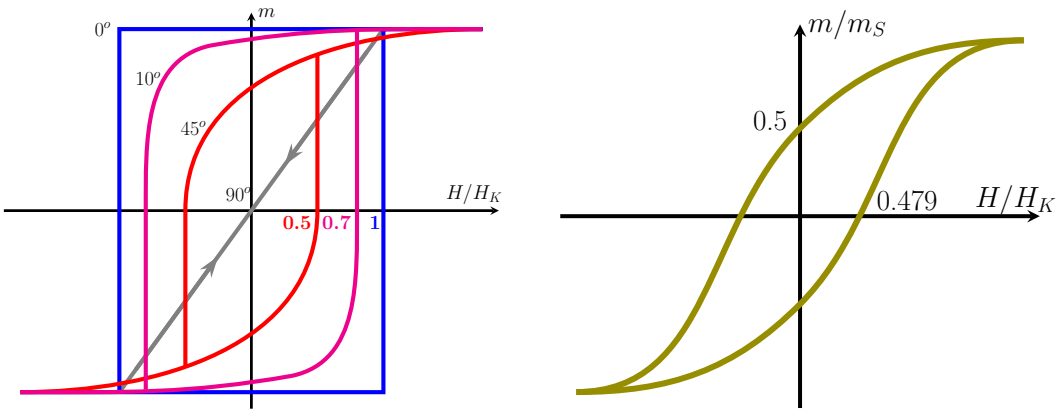

(a) The effect of applied field angle in the Stoner-Wohlfarth model.

(b) Randomly oriented particles with applied field in the Stoner-Wohlfarth model.

Figure 2.3: Misaligned and randomly oriented particles with an applied field in the Stoner-Wohlfarth model, showing how the applied field angle affects the values of $\frac{H}{H_K}$ and $\frac{m}{m_S}$.

yields a hysteresis loop as shown in fig. 2.3(a).

If there is an angle θ between the applied field and the moment of the particle, which lies along a , then there will also be a torque

$$\overline{\tau} = \overline{m} \times \overline{B} \tag{2.2}$$

on the particle $\overline{\tau}$ which is a cross product of the sample moment $\overline{m}$ and the applied field $\overline{B}$. This results in a rotation of the moment which reduces the coercivity. The effect is drastic at even low angles, with a 10° misalignment resulting in a 30% reduction in the coercivity and a reduction of 50% at 45° as shown in fig. 2.3(a). If this angle is increased to 90° then the particle simply follows the field and the magnetisation curve goes through the origin as the particle reverts back to its original position with the removal of the field.

If the particles are randomly aligned the result is the hysteresis loop shown in fig. 2.3(b). The remanence is reduced to half and the coercivity to 0.479 times that of the aligned case. The value of 0.479 is the root-mean-square (RMS) of the cosine function in three dimensions.

2.1.2 Thermal Activation

Temperature effects must be considered in any real system with a Boltzmann distribution of thermal energies. Some of the thermal energy in the system will be great enough to excite a phonon that flips a moment. In the aligned case the energy barrier that must be overcome is [46]

$$\Delta E = KV\left(1 - \frac{H}{H_K}\right)^2 \tag{2.3}$$

where ΔE is the energy barrier, K the anisotropy constant, V the volume of the particle and H the applied magnetic field. At zero applied field the second term disappears and as such the thermal stability of a particle is dependent upon its volume and its anisotropy.

The statistical probability of a particle reversing its magnetisation in a given time is given by the Néel-Arrhenius Law [47]

$$\tau_r^{-1} = f_0 exp - \left(\frac{\Delta E}{k_B T}\right) \tag{2.4}$$

where τ_r is the relaxation time, given as the time for 37% ($1/e$) of particles to maintain their magnetisation, f_0 the attempt frequency, usually taken as 1×10^9 Hz to 1×10^{10} Hz [48] and $k_B T$ the thermal energy, with k_B as the Boltmann constant and T as the temperature. This however only applies to a system of particles with identical volumes, shape and crystal structure and therefore no distribution of energy barriers due to variations in K or V. Therefore a real distribution of the time o thermal dependence of the magnetisation can only be determined experimentally.

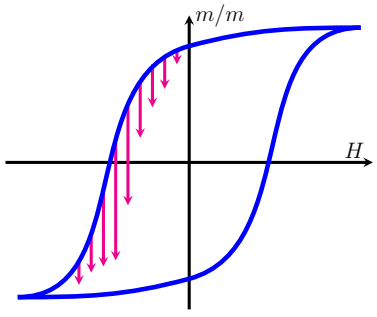

Figure 2.4: Magnetisation decrease as a function of field.

A magnetic material has only two equilibrium states; the positive and negative saturations. When a positively saturated sample is placed in a negative magnetic field the thermal energy will reverse the material towards the negative equilibrium as shown in fig. 2.4. This means that the magnetisation of a material is a time or frequency dependent effect [49]. The rate of the decay is dependent upon the magnitude of the applied field and will be at its maximum at the remanent coercivity [50]. This time

dependence over the switching field region is given by a logarithmic law [49]

$$M(t) = M(0) + S(H)\ln(t) \tag{2.5}$$

where $M(t)$ is the time dependence of the magnetisation, $M(0)$ the magnetisation at $t = 0$ and $S(H)$ the field specific time dependence coefficient.

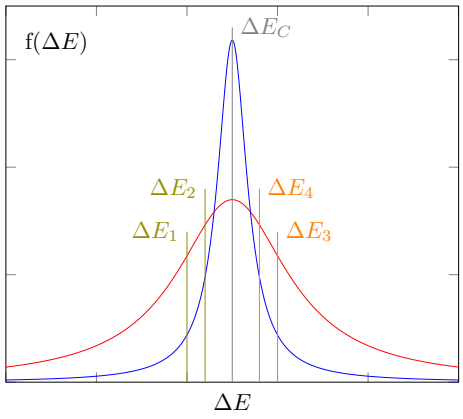

Figure 2.5: Energy barrier distributions for samples with the same median grain volume but different distributions.

Films with strong intergranular exchange (section 2.1.3) however exhibit non-linear $ln(t)$ behaviour [51]. This is due to the rate of change in a switching field distribution ($f\Delta E$) being very high in a narrow distribution (blue) as opposed to a wide one (red), as shown in fig. 2.5. As the time dependence is measured at a field below the coercive energy barrier (ΔE_C), the particles being reversed are those with a barrier ΔE_1. As time passes the reversed entities become those at ΔE_2 which, in a narrowly distributed system, is a large increase in particle number. As such the rate of magnetisation reduction increases from $ln(t)$ [52].

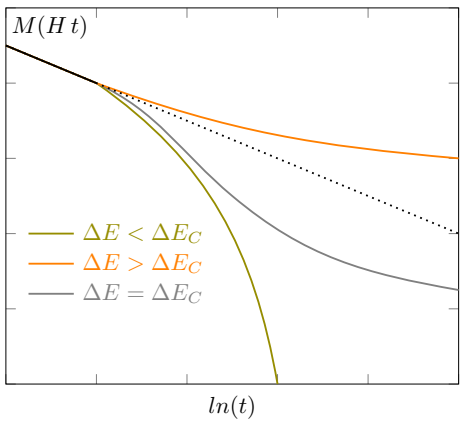

Figure 2.6: $M(t)$ deviating from logarithmic behaviour with different applied fields.

The opposite is true for ΔE_3 to ΔE_4 above the coercivity and has been calculated both as a sum over a series of $ln(t)$ and as an integral [52, 53]. If the reversal is measured at the coercivity and the peak of the distribution, a combination of the two behaviours is seen as shown in fig. 2.6 [54]. However, in a real system with a distribution of energy barriers this occurs most strongly at the remanent coercivity [55]. This is because the small, low energy-barrier particles will decrease the magnetisation and the coercivity is not at the peak of the distribution. Therefore for a more accurate characterisation of a material the remanent coercivity must be used.

This has significant ramifications for measurements of hysteresis loops. The magnetisation and coercivity of a sample are dependent on the sweep rate of the magnet. Therefore care must be taken when comparing the hysteresis loops of materials from different systems. For example the coercivity from a permeameter that runs at 50 loops per second will be very different to a vibrating sample magnetometer with averaging times of 1 s/point to 10 s/point.

It is not possible to couple a thermal bath to a magnetic field, and therefore the modelling of the effects of thermal energy on a magnetic field are complicated. However, the thermal fluctuations due to the energy can be viewed as an added fluctuating field, as proposed by Néel and formulated by Street and Woolley, along with Wohlfarth [54, 56, 57]. This is discussed in detail with regards to the alternating gradient force magnetometer in section 4.3.2.

2.1.3 Interactions

The Stoner-Wohlfarth model is unsuitable for many systems as it assumes that the particles have no interactions with one another. There are two types of interaction that commonly occur which are exchange interactions and dipolar interactions.

Dipolar interactions arise from the stray fields of the particles having an influence upon one another, as shown in fig. 2.7. There is now a potential energy U which is proportional to the two magnetic moments and the angle θ between

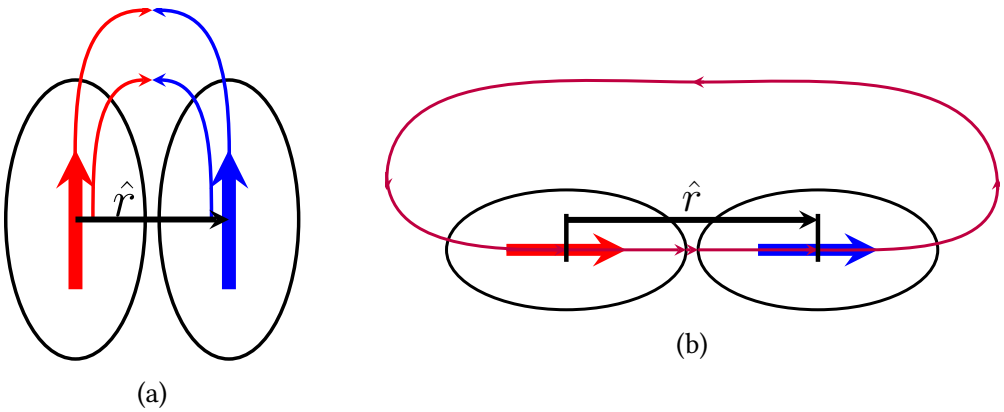

(a) (b)

Figure 2.7: Dipolar interactions due to stray fields for (a) parallel and (b) aligned particles.

them

$$U \propto m_1 \cdot m_2 \cos\theta \tag{2.6}$$

for two moments with their easy axes parallel as in fig. 2.7(a). As such there is a positive energy when the particles are parallel and negative for the antiparallel state. Hence there is now a preferred orientation of antiparallel spins which stabilise each other. If two particles share an easy axis, as shown in fig. 2.7(b), then there is an added term to the energy of the system

$$U \propto \overline{m}_1 \cdot \overline{m}_2 - 3(\overline{m}_1 \cdot \hat{r})(\overline{m}_2 \cdot \hat{r}) \tag{2.7}$$

where $\hat{r}$ is a unit vector between the centres of the dipoles. Obviously this second term is ignored in the first case where $\overline{m} \cdot \hat{r}$ is zero, however becomes dominant when the moments are in-line. Now the antiparallel state has a higher potential since one of the $\overline{m}_x \cdot \hat{r}$ terms is negative and as such the parallel state is the ground state. The moments of the particles aligned parallel support each other, as shown in fig. 2.7(b).

In a dense thin film there are however no, or very few, truly free dipoles due to the proximity of the grains. Therefore dipole interactions are much more significant in perpendicularly magnetised films and in dispersed or segregated media.

This had significant ramifications for the recording industry in the shift from longitudinal to perpendicular recording. In a longitudinal device, bits of opposing sign would attempt to reverse one another, reducing stability in the storage. In perpendicular recording neighbouring bits support one another with their stray fields, increasing the stability.

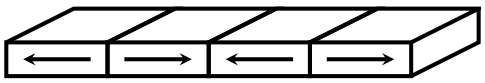

(a) Longitudinal recording media.

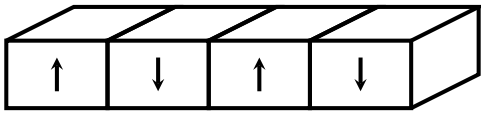

(b) Perpendicular recording media.

Figure 2.8: Magnetisation directions of neighbouring grains in (a) lateral and (b) perpendicular recording media.

Exchange interactions between dipoles can be further divided into three types, one called direct exchange. There are also two types of indirect exchange called RKKY exchange [58] and superexchange [59]. Superexchange has its origin in the antiferromagnetism in oxides where the metal orbitals couple antiparallel via the p-orbital of an oxygen atom. Therefore this is not further discussed in this work.

Direct exchange [60, 61], also called Heisenberg exchange, affects individual

spins at very close distances. The effect is short range as the strength of the coupling falls of as $1/r^6$, where r is the atomic separation, and therefore is significantly affected by structural changes. The exchange energy E_{ex} of two adjacent spins $S_{1,2}$ is dependent upon their orientation and separation and is given by

$$E_{ex} = -2J_{ex}\overline{S}_1 \cdot \overline{S}_2 \tag{2.8}$$

where J_{ex} is called the exchange integral.

For a select few elements, namely Fe, Ni and Co, this is a maximum when the spins are aligned parallel and the material is a ferromagnet. For other atoms perfect antiparallel alignment is preferred, for example Mn or Cr, and is antiferromagnetism. Careful arrangement of atoms in a lattice however can have a large impact on E_{ex}. For instance while Mn is an anitferromagnet, the addition of Pt affects the inter-atomic spacing such that MnPt is ferromagnetic. This is the origin of the magnetism in Heusler alloys, and is further discussed in section 3.2.

Indirect exchange must be considered in electrically conductive materials like Heusler alloys. As shown in fig. 2.9 electrons entering a magnetic grain will be polarised by the magnetisation of that grain. As these electrons conduct to another grain with a misaligned magnetic moment, the electrons are scattered and a torque applied to the magnetic moment of the second grain. This couples the moments of neighbouring grains together in a metallic system, leading to a preferential parallel alignment.

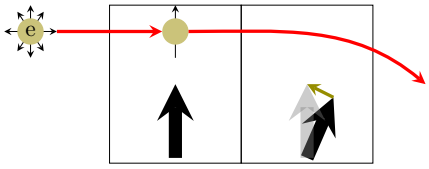

Figure 2.9: RKKY coupling of two grains via conduction electrons.

2.1.4 Domain Wall Effects and Motion

The stray field from a magnetised material acts to demagnetise the material itself as shown in fig. 2.10(a), and is named the demagnetising field, H_D. This has significant effects on perpendicular anisotropy, which will be further discussed in section 2.2. This external field creates a magnetostatic energy E_{ms}

$$E_{ms} = \frac{1}{2} H_D M \tag{2.9}$$

In order to reduce the energy the field is contained within the material in domains as shown in fig. 2.10(b).

The regions between domains are now regions of change in magnetic order called domain walls. In a domain wall the spins of the system must rotate through an angle up to 180° throughout the width of the wall depending upon the relative orientation of the neighbouring domain.

Within the domain wall the exchange energy E_{ex} attempts to keep the angular divergence between spins as narrow as possible, leading to walls of near infinite width. However, the anisotropy energy E_K

$$E_K = KV \tag{2.10}$$

seeks to have instantaneous reversal and therefore a very narrow domain wall. The origins of this anisotropy are discussed in section 2.2.1. The domain wall width is therefore a balance between E_{ex} and E_K. If the domain wall energy of a system is lower than E_{ms} then a fully flux-closed system can be formed as shown in fig. 2.10(c). Here the flux of the system is entirely contained within the material.

This is true in a perfect crystal. However, in a real system there are defects caused by dislocations, grain boundaries and impurities. Since E_{ex} is so sensitive to the relative atomic spacing these regions disrupt the energetic equilibrium and domain walls will preferentially form at these locations. These are called domain wall pins.

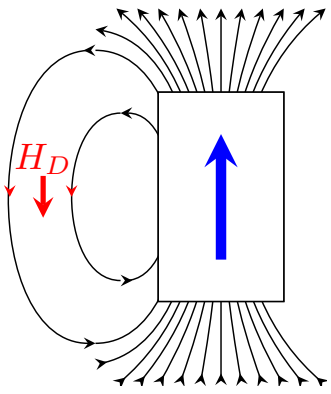

(a) The demagnetising field of a body.

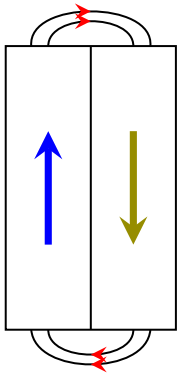

(b) Domain formation.

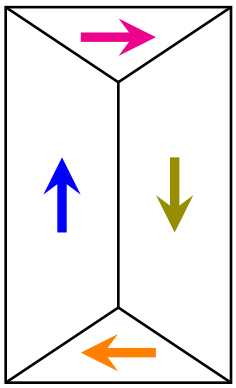

(c) A perfect flux closure.

Figure 2.10: The origin of the demagnetising field and the reduction in the stray field from a magnetised body by the formation of domains.

In a polycrystalline sample with large domains of the order of 100 µm there are many domains. The arrangement of the domains is not perfect, as in fig. 2.10(c), but a stochastic arrangement of domains which integrate to a zero net magnetisation without an applied field. With the application of a field the domain walls move easily through the crystal only getting pinned infrequently. As such a sample with low coercivity is obtained, known as a soft material as shown in fig. 2.11(a).

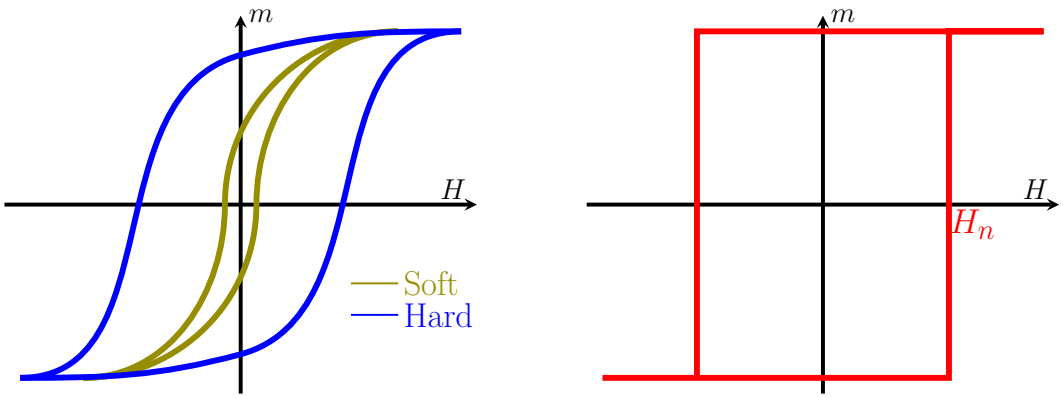

(a) Soft and hard magnetic materials.

(b) Nucleation in a strongly coupled film.

Figure 2.11: Comparison of magnetisation reversal in (a) soft and hard materials and (b) a nucleation controlled material.

A material with a high density of pins or small grains will have smaller domains <0.1 µm. Therefore a lot of energy is required to move domain walls through the crystal and the magnetisation does not easily relax upon removal of the field. Therefore a high coercivity sample called a hard material is obtained, as shown in fig. 2.11(a). There is no exact definition of the boundary between soft and hard materials and this has changed significantly over time with the development of high energy product magnets, for example Alnico and NdFeB. However, for most purposes a soft material can be defined as one with a coercivity <100 Oe.

Additionally if the sample has strong intergranular coupling then the reversal becomes dominated by nucleation and propagation effects. Reversal of the sample occurs at the nucleation field H_n when just one domain reverses and causes an avalanche reversal of the whole film. A highly square hysteresis loop is obtained as in fig. 2.11(b) as is the case for permanent magnets such as NdFeB.

2.2 Perpendicular Magnetic Anisotropy

Anisotropy is the directional dependence of a measured property. Magnetic anisotropy is an energy density along a given crystal or sample direction, most often quoted in ergs/cm^3. Magnetic anisotropy, or the lack thereof, is a major limiting factor for the progress of spintronic devices.

For antiferromagnetic materials the anisotropy values of new materials, for example Mn_3N, cannot compete with $IrMn_3$ which has an anisotropy value K of up to 3×10^7 ergs/cm^3 [62], which they try to replace. In thin film ferromagnets the anisotropy generally lies within in the plane of the sample. In order to overcome this for high-density applications manipulation of the material must often take place. A thorough mathematical treatment of the anisotropy can be found in "*Introduction to Magnetic Materials*" by B.D. Cullity [63], chapter 7, page 197.

2.2.1 Types and Origins of Anisotropy

Anisotropy in a magnetic system can be broken down into two major types: the magnetocrystalline anisotropy arising from the lattice itself and shape anisotropy from the shape of the grains.

In any system there are two contributions to magnetic moment. The orbital motion, L, of an electron in an atom constitutes a current loop which in turn produces a B-field. The second source is the intrinsic spin angular momentum of the electron S, acting in a similar way. Magnetocrystalline anisotropy is due to the spin-orbit (LS) coupling present in all materials, also called Russell-Saunders coupling. There is also *j-j* coupling in heavier elements in the lanthanide and actinide series, however these do not effect the Heusler alloys and as such the LS coupling is dominant.

The orbits of an atom in a lattice are defined by the lattice itself and pinned in place by the bonding. As such the L contribution to the magnetisation is pinned and is commonly referred to as being 'quenched.' As such the spin moments control the magnetisation in an external field. However, these are coupled to the lattice directions by the LS-coupling. The result of this is the formation of easy and hard magnetisation crystal directions where the energy required to break the LS-

coupling varies. In body-centred cubic (bcc) iron, this results in an easy axis along the <100> directions, a medium direction in the <110> and a hard axis on the <111> as shown in fig. 2.12.

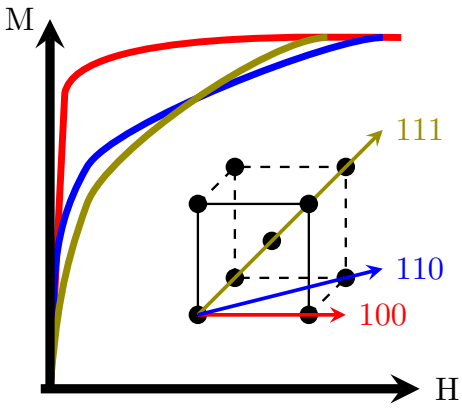

Figure 2.12: The magnetisation with applied field in easy and hard directions for e.g. Fe.

Shape anisotropy is a result of the minimisation of magnetostatic energy E_{ms} due to the self-demagnetising field H_D of a grain, as discussed in section 2.1.4. As shown in fig. 2.13 the anisotropy of an elliptical particle will be uniaxial along its major axis because this minimises the energy by having the greatest north-south pole-to-pole separation. This is due to the different demagnetising factors along the major a and minor c axes which defines H_D

$$H_D = -N_{a,c}M \tag{2.11}$$

where $N_{a,c}$ are the major and minor demagnetising factors.

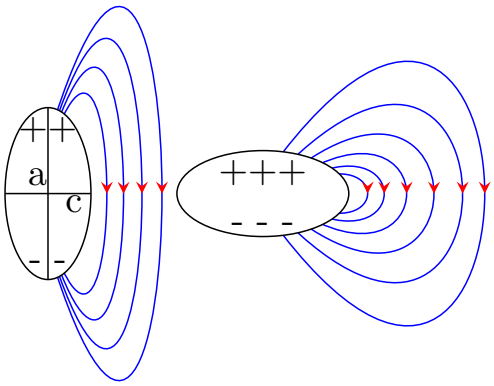

Figure 2.13: The demagnetising fields along the easy and hard axes of an ellipsoid.

In a thin film if the magnetisation lies in the plane of the sample then the B-field of the sample is mostly contained within the sample. The result of this is that the value of H_D in the plane of the sample is zero whereas perpendicular to the plane

$$H_{D_\perp} = -4\pi M \tag{2.12}$$

resulting in a large "tilt" in the hysteresis loop that must be corrected for.

Anistropy in a material can also be induced at interfaces with another material

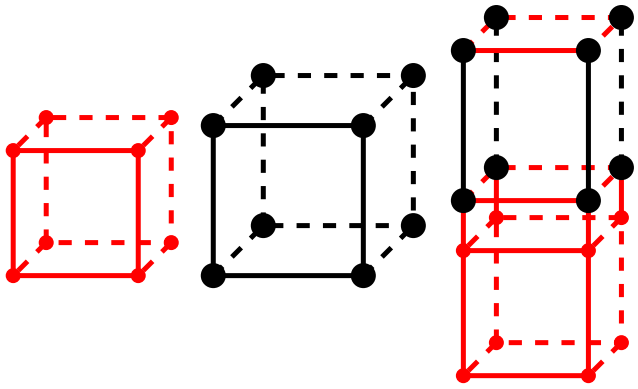

Figure 2.14: The strain induced in a layer (black) by a seed layer (red) in order to match the lattice constant causes a tetragonal distortion.

[64]. This occurs in one of two ways. Firstly a strain can be induced in a material by a seed layer and lattice matching. When materials are deposited there is an energetically favourable arrangement whereby the atoms in subsequent layers sit in well defined positions, with equal separation from neighbouring atoms. However at interfaces between two different materials this will be difficult as the ideal atomic separation for the atoms of the two materials is different. The system can therefore minimise its energy by modifying the atomic separation of one or both of the layers to better match the other as shown in fig. 2.14.

This change in lattice parameter has a significant effect upon the magnetic properties of a film. For example a cubic material, which has three equal directions in [100], [010] and [001], can be strained into a tetragonal lattice with a basal plane of smaller lattice constant than the out-of-plane direction as shown in fig. 2.14. This can result in an anisotropy out of the plane of the sample [32].

Interfaces also induce anisotropy due to the interactions between electron structures in the two layers [64]. At the interface of an oxide and a Co- or Fe-based ferromagnet there is a hybridisation of the $3d$-orbitals of the ferromagnet and the $2p$-orbitals of the oxygen. This hybridisation induces a perpendicular anisotropy. This has found extensive usage in magnetic tunnel junctions (MTJs) where an MgO/CoFeB interface at the tunnel barrier allows for perpendicular devices to be fabricated [29].

Additional anisotropy in these systems is introduced at the capping layer [30]. A MTJ with the structure MgO/CoFe/Ta will have a higher anisotropy than that with a ruthenium capping layer, but lower than that of one with an hafnium capping layer. The origins of this anisotropy are still under investigation but are thought to come from the strong spin-orbit interactions in heavy metals. Thus

the same outcome is observed for underlayers and the anisotropy can be induced at both [31]. This must be balanced with the crystallographic influence of a change in seed layer, especially as annealing has been shown to either increase or decrease the anisotropy in a sample depending on the materials used [31].

2.2.2 Materials with Perpendicular Magnetic Anisotropy

In thin-film, polycrystalline samples, the magnetisation lying in-plane will remove the stray fields of the grains by coupling, as shown in fig. 2.7(b) and as such for most materials an in-plane easy-axis is observed. In a single crystal this anisotropy will be fourfold along the symmetric easy axes, usually along two of the symmetry axes of the substrate. Additional easy axes can also be present with interfacial conditions; for example a Heusler alloy such as Co_2FeSi on a GaAs substrate will have fourfold anisotropy along the <100> directions but also an additional easy axis in the <110> directions due to interfacial effects [26, 65]. However this anisotropy is still in the plane of the sample.

The simplest material to exhibit perpendicular magnetic anisotropy is hexagonal close packed (hcp) cobalt. As shown in fig. 2.15(a) there is a large asymmetry in an hcp lattice leading to an easy direction along the *c*-axis. If a seed layer or suitable substrate is used then the *c*-axis will grow out-of-plane and consequently the anisotropy will be out of the plane. This is in spite of the high M_S of 1400 emu/cm^3 of cobalt.

The anisotropy is strong with a K of 4.1×10^6 ergs/cm^3 but still low for ideal

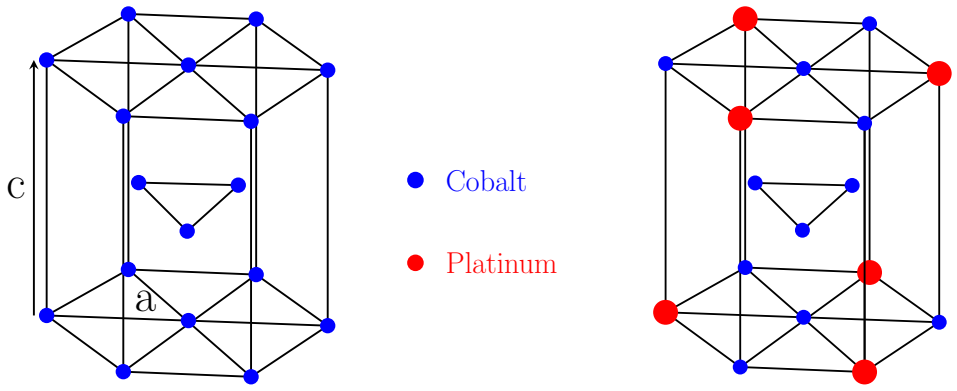

(a) Hexagonal cobalt lattice. (b) $L1_0$ CoPt lattice.

Figure 2.15: The hexagonal structures of cobalt and CoPt which exhibit perpendicular magnetic anisotropy.

device application. Alloying of the cobalt with large platinum atoms gives an $L1_0$ structure as shown in fig. 2.15(b). This enhances the anisotropy to $>1 \times 10^7$ ergs/cm^3 and is used in a hard-disc drives [66]. In reality the lattice must be poisoned with chromium to reduce M_S in order to reduce the value of H_D.

Cobalt and platinum also exhibit a strong perpendicular magnetic anisotropy when placed in a multilayer structure $[\text{Co/Pt}]_n$ with values of K of the order of 2×10^6 ergs/cm^3 [67]. This is due to the interfacial anistropy discussed in section 2.2.1 where the combination of a ferromagnetic and heavy element induces perpendicular magnetic anisotropy [68]. It is also possible that alloying at the interfaces will create a CoPt alloy which will enhance the perpendicular magnetic anisotropy.

Perpendicular anisotropy has been induced in Heusler alloys by exploiting the same effects observed in CoFeB-based MTJs discussed in section 2.2.1 [27]. However, the roadmap for spintronic devices to achieve a read-head for recording densities above 2 Tbit/inch^2 prohibits a high resistance area product (RA) [15]. As such alternative means for creating perpendicular magnetic anisotropy in Heusler alloys must be developed. Examples may include heavy metal interfaces or strain induced anisotropy.

Device applications such as read-heads also place requirements on several factors about the system which must be considered. Firstly, edge effects will have a significant effect on the sample. Any change in the anisotropy of the sample at the device edges, especially corners, can significantly change their behaviour from that of the bulk. Secondly the assumption that the lateral dimensions are infinitely larger than the out-of-plane dimension is no longer always valid.

Furthermore the fabrication of devices can have a significant effect on anisotropy and magnetisation [69]. This is caused by milling or lithography, where interlayer mixing is caused by high energy impacts and heating of the sample. As such the demagnetising field and reversal properties of devices must be carefully considered and the thin-film behaviour cannot always be directly translated into device performance.

2.2.3 Demagnetising Effects

The origins and magnitude of the demagnetising field have been discussed previously in sections 2.1 and 2.2. H_D can have several effects on a material other than defining its easy axis. The most significant of these affect the measurement of properties of a material, especially in relation to the hysteresis loop.

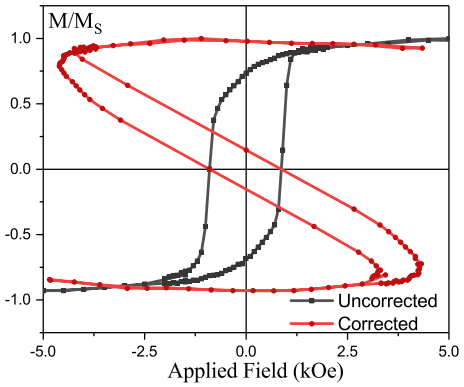

Figure 2.16: Over-correcting for H_D in a film with strong intergranular exchange coupling.

As mentioned in section 2.2.1 the result of H_D is to create a tilt in the hysteresis loop of a measured sample. This appears to decrease the remanance of the material and the squareness of the loop. It appears trivial for a thin film to simply subtract the calculated value of H_D from eq. (2.11). This is the case unless there is any intergranular exchange coupling present whereby the subtraction of the theoretical value of H_D will over-correct the loop as shown in fig. 2.16.

A DC demagnetising (DCD) curve allows for the measurement of the interactions between grains giving an activation volume (V_{act}), which describes how the material reverses its magnetisation. In these measurements it is necessary to apply zero field after a negative field is applied in steps from saturation in order to measure the remanence. However, for a perpendicularly magnetised sample there is no access to zero field due to the presence of H_D. As such the true DCD curve for the sample cannot be obtained. The measurement determines the effective activation volume seen by the material.

In a device application this would be the real activation volume that determines the switching properties of the device. As such while the fundamental DCD curve and consequent properties cannot be determined the measurement remains valid for characterising materials as they would be applied. A true value for the activation volume can be determined using a waiting time method [70, 71]. By

measuring at a constant magnetisation the effects of the unknown demagnetising field can be ignored. These methods are discussed in more detail in section 4.3.3.

2.3 Magnetoresistance

The discovery of magnetoresistance marked the beginning of spintronics. A change in the resistance of a system can be induced that is not dependent on the current or voltage applied but on the spin orientation of the current. This added an extra degree of freedom to electronic measurements that has become technologically indispensable.

Magnetoresistance most commonly occurs in the three forms of anisotropic, giant and tunnelling magnetoresistance; these are discussed in detail below. However there are several other, less common forms of magnetoresistance such as colossal [72] and extraordinary magnetoresistance [73].

2.3.1 Anisotropic Magnetoresistance

Anisotropic magnetoresistance (AMR) is a property of all ferromagnetic materials and was first observed by Lord Kelvin [1]. AMR causes an increase in the resistance of the material when the current is oriented in the same direction as the magnetisation and a decreased resistance is observed when applied orthogonally. The effect is typically smaller than 1% but magnitudes of up to 50% have been observed in exotic compounds [74].

The net effect is generally a small increase in resistance when the magnetisation and current are parallel and a decrease for perpendicular alignment. AMR has many applications in devices such as electronic compasses and traffic sensors. AMR was also exploited for the first magnetoresistive read-head in hard-disc drives.

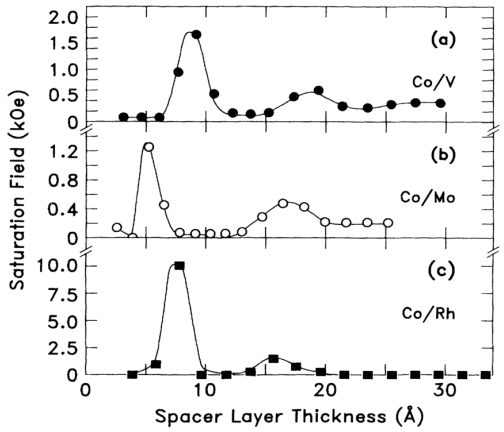

(a) Oscillating antiferromagnetic coupling of Co through metal layers.

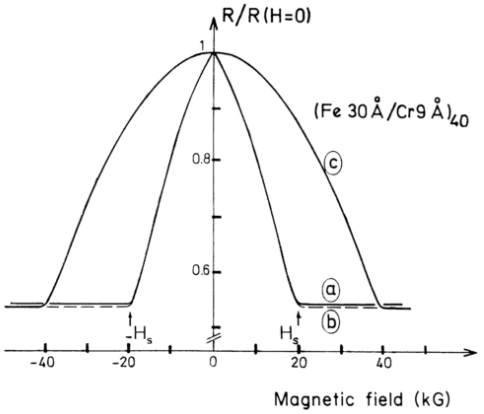

(b) GMR data of the group of Albert Fert of a $[Fe/Cr]_{40}$ multilayer at 4 K.

Figure 2.17: (a) The antiferromagentic coupling of two FM layers [75] and (b) the GMR data for the 2007 Nobel prize [9].

2.3.2 Giant Magnetoresistance

Giant magnetoresistance (GMR) was discovered independently by the groups of Fert and Grünberg in 1986/8 [9, 10], for which they shared the 2007 Nobel Prize. GMR is observed in samples of alternating ferro- and non-magnetic (FM and NM) layers, depending strongly on the thickness of the layers as shown in fig. 2.17(a). Grünberg, and later Parkin, found that there was an oscillating ferro- and antiferromagnetic coupling between alternating FM layers with NM layer thickness [10, 75].

This discovery was a marked improvement on the AMR discovered by Thomson. AMR effects are typically on the order of 1% and yield low-sensitivity devices. The work of Fert, however, found the magnetoresistance to be 20% at room temperature in an alternating Fe/Cr structure as shown in fig. 2.17(b), and as such was named giant magnetoresistance [9].

A detailed discussion of the theory of GMR can be found in Chapter 16 of *Heusler Alloys* edited by Felser and Hirohata [76]. The arguments laid out here closely follow the discussion found there. A GMR device can be operated in two geometries with the current applied either in or perpendicular to the plane, named current-in-plane (CIP) and current-perpendicular-to-plane (CPP) GMR respectively. The original investigations of the effect were in the CIP regime as this is much easier to fabricate.

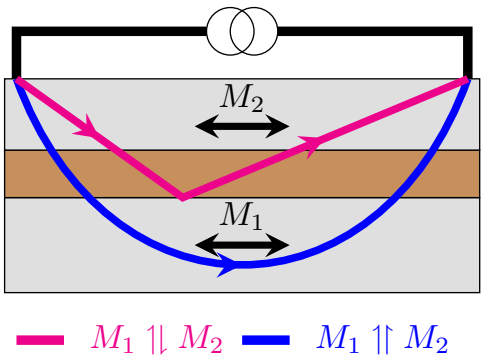

Figure 2.18: The interfacial reflection of current in CIP-GMR geometry.

In the CIP geometry the magnetoresistance is purely due to an interfacial resistance from asymmetric spin-scattering. As such for this to occur the thickness of the NM and FM layers must be much less than the spin-diffusion lengths λ_{SD}. GMR is also highly dependent upon the layer thickness due to current penetration. The bulk of the current does not contribute to the signal, simply conducting along the sample surface. As shown in fig. 2.18 there is a low resistance state when the magnetisation of one layer M_1 is parallel to the other layer M_2. Electrons polarised in layer two will easily conduct into layer one. However, when the two are antiparallel then a scattering will occur due to the misalignment of the electron spin and M_1.

Much larger GMR ratios are obtained in a CPP geometry. The reason for this is two fold; firstly all of the current must pass through both layers of the stack. As such the entire current contributes to the GMR signal and a much larger ΔRA is observed.

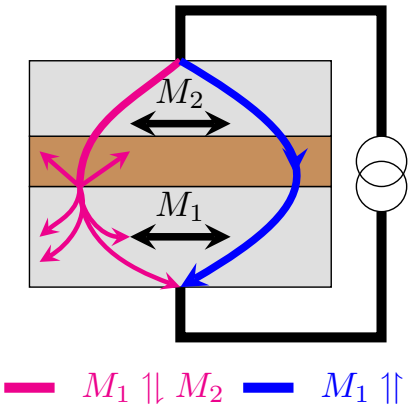

Figure 2.19: The interfacial and bulk scatterings of current in CPP-GMR geometry.

Secondly the bulk of both FM layers now contributes to the spin-dependent resistance; in addition to the interfacial spin dependence in CIP-GMR. The net magnetisation of the layer contributes a spin-dependent scattering term to the resistance. The total ΔRA for an alternating NM/FM multilayer can be described by the Boltzmann equation

$$\Delta RA = \frac{\left(2\beta\rho^*_{FM}t_{FM} + 2\gamma AR^*_{FM/NM}\right)^2}{2\rho^*_{FM}t_{FM} + 2AR^*_{FM/NM} + \rho_{NM}t_{NM} + 2AR_{FM/NM}} \tag{2.13}$$

where γ and β symbolise the interfacial and bulk spin-asymmetry coefficients. These can be expressed in terms of the spin-dependent interfacial resistance

$R^{\uparrow(\downarrow)}_{FM/NM}$ and the bulk resistivity $\rho^{\uparrow(\downarrow)}_{FM}$

$$\gamma = \frac{R^{\downarrow}_{FM/NM} - R^{\uparrow}_{FM/NM}}{R^{\downarrow}_{FM/NM} + R^{\uparrow}_{FM/NM}} \qquad \beta = \frac{\rho^{\downarrow}_{FM} - \rho^{\uparrow}_{FM}}{\rho^{\downarrow}_{FM} + \rho^{\uparrow}_{FM}} \tag{2.14}$$

These expressions give rise to the shorthand in eq. (2.13)

$$R^{*}_{FM/NM} = \frac{R_{FM/NM}}{(1-\gamma^2)} \qquad \rho^{*}_{NM} = \frac{\rho_{FM}}{(1-\beta^2)} \tag{2.15}$$

2.3.3 Tunnelling Magnetoresistance

As similar effect to GMR can be obtained using an insulating oxide barrier in place of the conducting layer. This was first observed by Jullière in Fe/GeO/Co multilayers in 1975 [77]. In this case it is the difference in tunnelling probability for parallel and opposite spin orientations that gives rise to the so-called tunnelling magnetoresistance (TMR).

The magnitude of this change was found to be 14% by Jullière at 4.2 K. In 1995 Miyazaki and Tezuka [78] and Moodera [79] found room temperature values of 18% and 11.8% respectively. However in 2004 the groups of Parkin and Yuasa independently managed to produce a TMR of 200% at room temperature using a MgO barrier with Fe FM layers [13, 80]. This has since been optimised with values being reported up to 1100% at low temperature [81], far exceeding GMR values which range from $< 1-100\%$. Calculated room temperature values of 1000% have also been reported [82, 83].

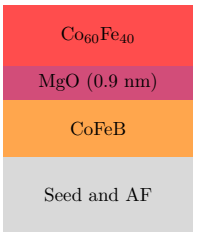

Figure 2.20: Schematic of the read-head stack in current HDD design.

This is the technology currently in place in the read-heads of hard-disk drives (HDD) as it gives a signal change of 125%, as shown in fig. 2.20. The design requires the use of the CoFeB layer in order to crystallise the MgO layer. There are inherent limitations to the concept however. Since an insulating layer is used in the stack, the resistance of the stack is unavoidably high and as such the storage capacity of an HDD is limited to 2 Tbit/inch^2. The *RA* value can be as low as 0.5 $\Omega/\mu m^2$ by reducing the MgO thickness as low as 0.9 Å, the first AF-coupling peak. However

the uncertainty in the layer thickness is very large. Therefore a transition back to GMR devices is a logical step in increasing the capacity due to intrinsically lower resistance-area products (RA).

TMR has a second advantage over GMR besides greater MR ratios. The interface between the MgO and the magnetic layer can naturally induce perpendicular anisotropy as discussed in section 2.2.1. While this can be undesirable for an in-plane application it makes the production of perpendicular devices far simpler. The second benefit of this method is that no extra layer, such as a seed layer, is required to induce the anisotropy since the anisotropy is induced at the tunnel barrier. This helps to keep device thickness, and therefore *RA*, to a minimum.

3 Heusler Alloys

The group of alloys known as the "Heusler Alloys" is numerous and diverse. First proposed by German chemist Fritz Heusler in 1903 [84] they come in two generally accepted "families" of tertiary alloys, the half- and full-Heusler alloys. The first type take the form XYZ and the second X_2YZ and in each case the elements X and Y are d-transition metals and Z a metalloid or non-metal.

The properties of Heusler alloys vary significantly due to greater than 3000 possible combinations of X, Y and Z existing [16]. For example the compound first investigated by Heusler, Cu_2MnAl, is a ferromagnet despite containing no ferromagnetic elements [84]. Since then Heusler compounds have been discovered that are half-metals [85], compensated ferrimagnets [86] and antiferromagnets [87, 88].

3.1 Structure and disorder in Heusler Alloys

The two families of Heulser alloys crystallise in two cubic structures of three or four interlocking face-centred cubic (fcc) lattices for half- and full-Heusler alloys respectively [89]. These two structures are shown in fig. 3.1. As shown in fig. 3.1,

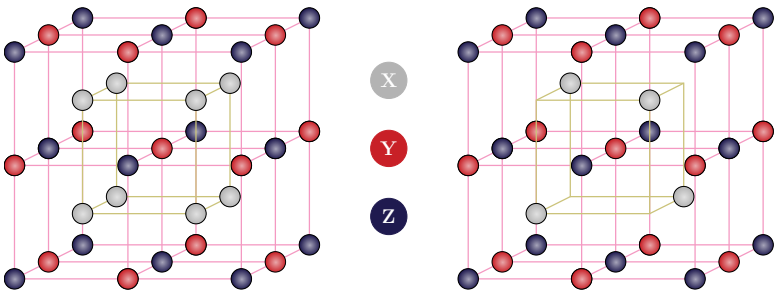

Figure 3.1: The (a) full- and (b) half-Heusler alloy structures denoted $L2_1$ and $C1_b$ where X is grey, Y is red and Z is blue.

in an $L2_1$ lattice the most electronegative material, X, occupies the position $\left(\frac{1}{4}\frac{1}{4}\frac{1}{4}\right)$; the other transition metal Y is in the $\left(\frac{1}{2}\frac{1}{2}\frac{1}{2}\right)$ position and Z is located at the origin (000). By forming eight linked body-centred cubic (bcc) cells with X atoms at the centre and Y and Z atoms at the corners, a supercell of 16 atoms is formed, where every atom is in an fcc ordered state which results in the four interpenetrating fcc lattices. The half-Heusler alloy $C1_b$ lattice is then formed if one of the fcc lattices is left vacant, specifically the second of the X sub-lattices.

It is immediately obvious that disorder in such a complex lattice is going to be: a) prevalent and b) significant in its effects. For the $L2_1$ ordered full-Heulser alloys the disorders are as follows and are shown in fig. 3.2 [90]:

- $A2$-type - full random occupation of the sublattices leading to bcc lattice.
- $B2$-type - free exchange of the Y and Z sublattices.
- $B32a$-type - exchange of both one X sublattice with Y and the other with Z lattice sites.
- DO_3-type - exchange of X and Y or X and Z lattice sites.

In reality the $B32a$ structure is extremely rare. To a lesser extent the same is true of the DO_3-type structures and, as such, the most common ordering of Heusler alloys is in the order of prevalence $A2$-type (disordered), $B2$-type (semi-ordered) and $L2_1$-type (fully ordered).

3.2 Magnetism in Heusler Alloys

Due to the variety of Heusler alloys their magnetic order (at room temperature) can be diamagnetic [76, 91], paramagnetic [76, 91], ferrimagnetic [86], ferromagnetic [16, 76, 88, 89, 91–93] or antiferromagnetic [16, 76, 89]. In this work the focus is on ferromagnetic Heusler alloys for use as the FM layers in a GMR stack.

Whilst many Heusler alloys that contain no magnetic elements are ferromagnetic, such as those discovered by Heusler himself, the most popular ferromagnetic Heusler alloys contain elements with the highest spin moments. These include the ferromagnetic elements and many Heusler alloys are found with formulae such as

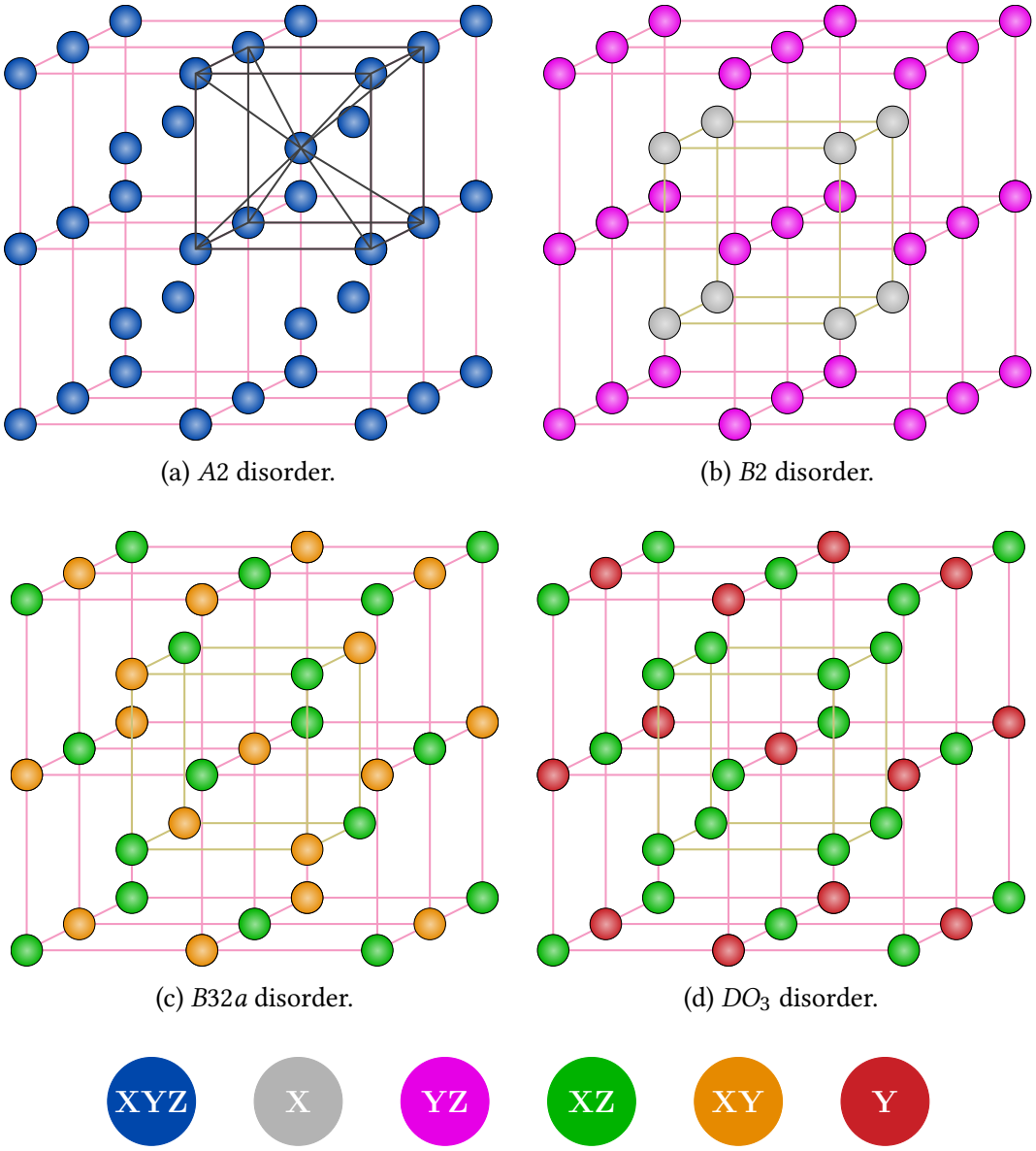

(a) $A2$ disorder.

(b) $B2$ disorder.

(c) $B32a$ disorder.

(d) DO_3 disorder.

Figure 3.2: The various disorders of the $L2_1$ full-Heusler structure.

Co_2FeZ or Fe_2CoZ. However, manganese has the highest moment per atom of the transition metals and is also extremely common in ferromagnetic Heusler alloys, especially in combination with the ferromagnetic elements giving Co_2MnZ and Fe_2MnZ, providing a very large magnetic moment per unit cell.

Magnetism in Heusler alloys is described by general Slater-Pauling behaviour [19] as shown in fig. 3.3. This rule arises from the the occupation of minorty bands in the X, Y and Z elements and represents a half-metallicity rule for full-Heusler alloys given by

$$M_t = Z_t - 24 \tag{3.1}$$

where M_t is the total magnetic moment in units of μ_B and Z_t is the total number

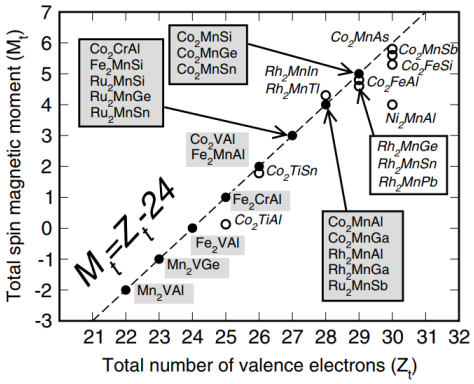

Figure 3.3: The relationship of the magnetism of full-Heuslaer alloys with valence electrons showing basic Slater-Pauling behaviour (dashed line) [19].

of valence electrons. The half-metallicity is further discussed in section 3.2.1.

Since the magnetism of the alloy is controlled by the exchange interactions discussed in section 2.1.3, it is clear that the magnetism is therefore controlled by the crystallography discussed in section 3.1. Firstly the bond lengths are determined by the identity of the three X, Y and Z atoms; i.e. a different inter-atomic spacing will be obtained for Co_2MnSi than for Co_2MnGe due to different electron densities. The stoichiometry of the system is then immediately responsible for the sign of the exchange. This then determines whether the system will be ferro- or antiferromagnetic or non-magnetic.

Secondly the disorder of the system can either create or destroy ferromagnetic ordering depending on the resultant inter-atomic spacings of each of the elements; i.e. X–X, X–Y, Z–Z etc. Therefore it is not clear cut as to the $L2_1$ structure having the strongest ferromagnetic ordering. This is especially true in antiferromagnetic Heusler alloys, where the $B2$ phase can be antiferromagnetic but the $L2_1$ is paramagnetic.

Further complications arise in polycrystalline films where the stoichiometry of grains will be heavily disrupted at grain boundaries. It is unlikely for ferromagnetic ordering to occur throughout the film in such a sensitive system, resulting in magnetically dead regions at grain boundaries. Therefore the net magnetisation of a polycrystalline film will be significantly lower than that of a single crystal.

Interfaces with other elements can also lead to issues due to the variety of Heusler alloys that are energetically stable. An interface between a transition metal seed layer S and a Heusler alloy X_2YZ can easily lead to diffusion if a Heusler alloy of form X_2SZ or S_2YZ is energetically favourable. This can lead to poisoning

of the ferromagnetism of the film. The problem is exacerbated by the requirement of many Heusler alloys to be heavily annealed for crystallisation to occur. This favours diffusion, especially of mobile elements such as Mn or Cr and can lead to magnetically dead layers at the interfaces. Consequently great care must be taken when choosing a seed or capping layer for a Heusler alloy film.

It is important to note that the interfacial layer will also be very sensitive to the termination of the Heusler alloy, i.e. whether the interface consists of X_2 or YZ atoms . This is discussed further in relation to interfacial anisotropy in section 3.2.2.

3.2.1 Half-Metallic Heusler Alloys

All metallic magnetic materials exhibit a spin imbalance at the Fermi energy, E_F. The majority spin-up band will have a greater density of states (DoS) than the minority spin-down band. This in turn gives rise to an unpaired spin-moment which then couples via the exchange interaction to determine the dominant behaviour of the material. Also, in all materials the bonding between all the atoms in the lattice will lead to hybridisation of orbitals, whereby the energy levels of the atoms are adjusted to compensate for the overlap in space of some orbitals and for their degeneracy.

In some materials the hybridisation of orbitals widens the spacing between neighbouring energy levels. If this shift is significant then the DoS of the material can turn from that of a continuous metalloid into a semiconductor with a band gap. This energy shift is not symmetric in the two spin-dependent DoS and as such the band gap only appears in one minority energy bands. Therefore a material is obtained where the majority spin band is a metal and the minority is a semiconductor; this is called half-metallicity. An example of the calculated density of states of a half-metallic full-Heusler alloy is shown in fig. 3.4.

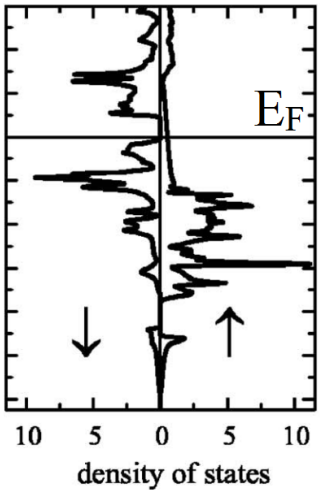

Figure 3.4:
DoS for Co_2FeSi showing the minority band gap [17].

This occurs to a significant degree in the CoMnZ half-Heusler alloys where the

hybridisation of Co-Mn orbitals results in a significant band gap [94]. A seminal material for half-metals is NiMnSb, one of the first materials with measured half-metallicity in a bulk state [76]. However, surface sensitive and low-temperature measurements both failed to yield a half-metallic DoS [95]. It was found that the half-metallic state was only obtained by occupation of interstitial sites by excess Mn [96]. This shows the crucial role of order and stoichiometry in the behaviour of Heusler alloys especially regarding their magnetism and half-metallicity.

Half-metallicity is easier to obtain in half-Heuslers alloys in theory due to there being only one Co atom per cell, and therefore only the Co-Mn hybridisation. However in full-Heusler alloys the Co-Co hybridisation can actually destroy the band gap or reduce it down to as low as 0.001 eV [97]. This behaviour is difficult to predict and model and the selection of Heusler alloys for application is a combination of modelling, e.g. via density functional theory (DFT), and experimental trial and error.

3.2.2 Anisotropy in Heusler Alloys

The origins of the anisotropy in magnetic materials are discussed in detail in section 2.2.1; however the specifics of anisotropy in Heusler alloys are not addressed. Heusler alloys have a cubic structure and as such possess cubic anisotropy. The easy axes of the super-cells lie along the {100} directions of the cube. Therefore in a single-crystal thin film there will be a fourfold anisotropy.

Cubic anisotropy is however rarely discussed in great detail. Depending upon the composition of the material there will be either eight equivalent easy directions along the ⟨100⟩ or the ⟨111⟩ directions. In a bcc materials, such as iron in fig. 2.12, the easy axes lie along the ⟨100⟩ and the hard axes along the ⟨111⟩. The opposite it usually true for fcc materials with the exception of cobalt ferrite or cobalt alloys, such as Heusler alloys [63]. However the presence of face-diagonal atoms in a fcc lattice adds a direction with intermediate hardness. Therefore the rotation of the magnetisation will most easily occur through this medium axis versus a hard one.

The presence of the medium direction reduces the energy barrier of reversal from KV to $\frac{1}{4}KV$ [98]. As such cubic materials are magnetically soft with coercivities below 200 Oe. Cubic materials are therefore inappropriate for applications such as permanent magnets or memory where stability, against both temperature

and field, is of paramount importance. Anisotropy must be induced in these systems for there to be any thermal stability.

This is due to magnetocrystalline anisotropy discussed in section 2.2.1 where anisotropy energy E_K aims to hold the magnetisation in its preferred direction. This can be expressed as a series expansion of the cosines α_{1-3} of the angles a, b and c that the magnetisation M makes with the crystal axes. This is of the form

$$E_K = K_0 + K_1(\alpha_1^2\alpha_2^2 + \alpha_2^2\alpha_3^2 + \alpha_1^2\alpha_3^2) + K_2(\alpha_1^2\alpha_2^2\alpha_3^2) \tag{3.2}$$

where K_{0-2} are the constants for the specific material under given conditions. Specific examples can be found in Cullity [63]. However, K_1 is the dominant term, since K_0 is angle independent and K_2 is often negligible; for example along the $\langle 111 \rangle$ directions K_2 is reduced to $\frac{1}{27}$ of the value of K_1. When K_2 is zero the sign of K_1 alone determines the easy axis, which is the $\langle 100 \rangle$ when K_1 is positive and $\langle 111 \rangle$ when it is negative. This is more complicated for a non-zero K_2, and a table the values can be found in Cullity [63].

The problems are further magnified in a polycrystalline film with no or only 2-D texture, as shown in fig. 2.1. The applied field will be at angles to the lattice directions, with a random distribution of easy, medium and hard directions. Therefore there will be no four-fold anisotropy in the film as every angle will have grains with an even mix of easy, medium and hard directions. The grain size also becomes a significant factor in the hysteresis as $\Delta E = \frac{KV}{4}$ and the distribution of grain sizes leads to a wide switching field distribution. In particular for a sample with a larger average grain size the maximum remanence is achieved for a narrow particle size distribution. This is because all or most of the particles will be blocked. The opposite is true for a sample with smaller grain sizes since small grains be superparamagnetic and a narrow distribution means that most grain will act as such [99].

As discussed in section 2.2.1 one way to induce perpendicular magnetic anisotropy is to use an interface with MgO. In the case of CoFeB the Co-O orbital hybridisation is at least partly responsible for the anisotropy. In a full-Heusler alloy the interfacial layer with the MgO is either X_2, e.g Co_2, or YZ, e.g. MnSi. Therefore the interfacial bond hybridisation is highly dependent on the termination of the Heusler alloy. As such perpendicular magnetic anisotropy may or may not be observed depending upon the layer order of the Heusler alloy [100].

Since the lack of anisotropy in Heusler alloys is due to a cubic symmetry it follows that strain induced anisotropy is a simple route to perpendicular magnetic anisotropy. Indeed a lattice mismatch of the alloy to a substrate or seed layer easily induces a tetragonal distortion in Heusler alloys. However, the anisotropy does not always lie along the c-axis and is frequently independent of c/a ratio.

Some Co-Fe alloys are an exception to the weak anisotropy of cubic materials. The exchange coupling between the Co-Fe atoms introduces a form of anisotropy in the cubic system. It follows therefore that by careful control of stoichiometry a Heusler alloy can be made with greater anisotropy, suitable for hard magnetic material application.

3.3 Role of Seed Layers

The stoichiometry of a Heusler alloy dictates the majority of its properties. However the ideal parameters cannot always be obtained especially with regard to the anisotropy of the system. In these cases there is a requirements for further modification of the system and this can be achieved by creating an interface between the Heusler alloy and another material. This is generally undertaken via the growth of seed layers below the Heusler alloy, but capping layers can be equally influential.

3.3.1 Structural Effects

As discussed in section 3.2 the magnetic order of a Heusler alloy is controlled by its structural order, e.g. $A2$ or $L2_1$. Seed layers can inhibit or improve the level of crystallisation in a Heusler alloy. Firstly, if a substrate is being used that has a significant lattice mismatch to the Heusler alloy layer it is unlikely that strong crystallisation will occur over along range. A seed layer can be introduced to reduce or increase the lattice mismatch. For example a layer with a lattice parameter between those of the substrate and the Heusler alloy could alleviate the problems of mismatch. Alternatively a thick (>50 nm) seed layer with a lattice match to the Heusler alloy can be used, which is able to relax to its bulk lattice parameter from that of the substrate.

This issue is particularly prevalent when application is the goal - while a Heusler alloy may have a perfect lattice match to a single crystal sapphire substrate this is not economically viable. Therefore seed layers play a vital role in industrial samples where cheaper substrates such as Si must be used. Lattice matching and mismatching to the seed layer can also induce strain in a Heusler alloy, as discussed in section 2.2.1. The strain can cause a reduction or increase in the lattice parameter of the Heusler alloy which in turn can cause tetragonal distortions either in or out of the plane [101, 102].

The seed layer can also improve crystallinity by lowering the formation enthalpy of the alloy. Heusler alloys often require extremely high temperature annealing to crystallise fully but the use of a seed layer can produce semi-crystalline Heusler alloys without or with only modest annealing [103, 104]. This is once more extremely beneficial for industrial applications, where a general limit of 350 °C is applied in order to protect devices [22].

Seed layers can also provide a smoothing effect to a substrate. Some substrates are rough due to surface oxidation, crystal steps or defects. A thin layer of material can smooth the surface, reducing the layer roughness of subsequent layers. Additionally some materials deposit in islands, constricting the grain size of the material to that of the islands. This effect can be mitigated by the addition of a smoothing layer, for example 3 nm of Cr under a layer of Ag prevents island growth [105] which is shown in fig. 3.5. Seed layers can therefore be used to alter, introduce or completely destroy a crystal habit in a Heusler alloy stack or device.

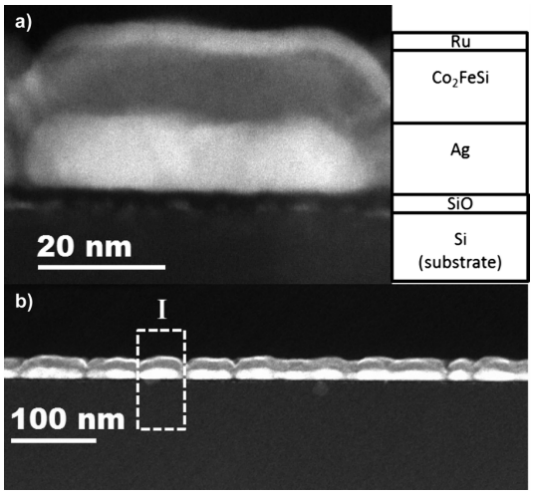

Figure 3.5: High-resolution cross-sectional micrograph of (a) single film island with film structure insert and (b) a low magnification image showing island periodicity [23].

3.3.2 Magnetic Effects

The effects of seed layers on the magnetic properties of a Heusler alloy can be divided into two categories: those directly linked to the structural effects discussed in section 3.3.1 and those due to interfacial interactions as discussed in section 2.2.1.

An increase in crystallinity, e.g. from *A*2 to *B*2 order or higher, due to a seed layer will result in the magnetic changes discussed in section 3.2. This is extremely beneficial if the required magnetic properties of a crystallised Heusler alloy can be obtained without excessive annealing. The magnetic properties of a thin film are also heavily influenced by the surface roughness. A rough interface will induce a large number of domain wall pins, slowing the magnetisation reversal process. A sample with a high level of roughness will therefore exhibit a greater coercivity than one which is smooth.

$IrMn_x$ is a seminal example of a cubic material with a dominant magnetocrystalline anisotropy, whose properties are heavily influenced by seed layers and interfaces. The properties of the material are heavily dependent on the composition, with inconsistent optimum values reported [106, 107]. $IrMn_3$ is a sheet antiferromagnet, with a uniaxial anisotropy in the ⟨111⟩ directions. The crystallinity and texture in the alloy is determined by the seed layer, with Ru, NiCr and Cu all resulting in different outcomes [108].

This anisotropy can also be moved to the out-of-plane direction if the ⟨111⟩ planes can be rotated. A combination seed layer must be used to achieve this however. On top of the conventional seed layer of Pt a 2-atom thick layer of CoFe is added. These stack one on top of the other without a crystal structure to minimise the energy in such a thin layer. Originally it was believed that this induced a crystallographic shift of the IrMn planes from 70° to the film plane to 90°. However X-ray analysis found that the IrMn {111} planes still lay in the plane. Therefore it must be a quantum mechanical exchange interaction between the two-ion anisotropy in the CoFe layer and the IrMn spins. The magnitude of this anisotropy is therefore strongly limited, as the anisotropy energy of the IrMn ⟨111⟩ is still very strong [109, 110].

Seed layers can have a negative impact on the magnetic characteristics of a Heusler alloy due to diffusion or intermixing discussed in section 3.2. If diffu-

sion occurs into the lattice then the exchange interactions within the material are changed, directly upsetting the magnetic ordering. This can either be in the form of an alternative Heusler alloy incorporating the seed layer material or a more amorphous layer; both of which lead to a magnetically dead or reduced ordered layer. Material diffusion can also occur at the grain boundaries which affects the intergranular exchange coupling [105]. Depending upon the diffused material this can either increase [23] or decrease the intergranular exchange coupling. If a decrease occurs to excess, such as in CoPtCr-SiO_2, then the grains of the material can be completely decoupled, drastically changing the magnetic properties of the material [111].

4 Experimental Techniques

4.1 Thin Film Deposition

Many thin film deposition techniques exist giving a wide array of film qualities and properties. These include slow, controlled processes such as molecular beam epitaxy (MBE) or atomic layer deposition (ALD) as well as fast processes such a pulsed laser deposition (PLD).

The different methods give widely varying outputs in terms of the structure and properties of the resulting layers. MBE is used to deposit single crystal, epitaxial layers of soft materials. The deposition rates in the system are extremely low (0.1 nm/s) and as such contamination is a major concern [112]. Therefore MBE requires the use of ultra-high vacuum (UHV) conditions of $<1 \times 10^{-9}$ mbar [113]. Similarly ALD suffers from the same low deposition rates as well as a high cost due to the single-crystal substrates often used and is somewhat limited in deposition materials [114]. This combination of factors make MBE and ALD only suitable for specialised industrial application where thin single crystals are required.

Pulsed laser deposition allows for rapid deposition (>10 nm/s) of alloys from either single, stoichiometric targets or from multiple targets with controlled ablation. Ablation is achieved using powerful laser pulses of approximately 10 W/cm^2 to 500 W/cm^2 which produces a "plume" of material to be deposited as shown in fig. 4.1 [115]. This can rapidly produce thick films of highly controlled composition. However during deposition particles up to microns in size reform after ablation leading to particulate

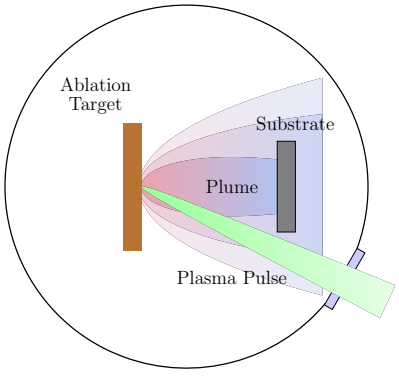

Figure 4.1: Basic schematic of a pulsed laser deposition system.

deposition in the film, severely limiting film quality [116]. PLD has been highly successful in several areas though, most prominently in the production of single-crystal oxide thin films [117, 118].

The magnetic properties of the films are also at risk with the above methods. In MBE and ALD single crystal samples are produced. The magnetisation reversal in these films is controlled by domain wall pinning at defects through the crystal. These are highly unpredictable and impossible to control and as such yield too much variation for mass production. Additionally only around 10% of ablated material is deposited on the substrate and as such waste is a major issue. With PLD the particulate deposition leads to a similar lack of control and therefore reproducibility [115].

Sputtering is a versatile technique allowing for rapid film deposition, high levels of grain size control [119–121] and the deposition of a huge range of materials. The process is much more varied and can be used to produce single crystal, atomically flat samples or highly polycrystalline or amorphous films. The sputtering process involves the surface bombardment of a metal or alloy target with energetic ions which liberate surface material. The presence of a gas in the chamber leads to an operating pressure in the range 1×10^{-4} mbar to 1×10^{-5} mbar. The versatility of this technique means it is commonly used in both research and industry.

By producing polycrystalline films the magnetisation reversal effects in single crystals are mitigated but it is clear that there will still be multiple, stochastic domain wall pins at the grain boundaries. However the reversal of the film can be made efficient and reproducible due to indirect exchange coupling between individual grains. This leads to a nucleation controlled process with a rapid, square magnetisation reversal ideal for applications such as in early coupled granular/-continuous (CGC) perpendicular recording [122] or the free-layer in the read-head of an HDD.

Alternatively a magnetic material can be co-sputtered with a dielectric. If the dielectric is insoluble in the metallic layer it will form a "shell" of insulating material which breaks the exchange between the grains which are then free to act as individual Stoner-Wohlfarth particles. The most prevalent and relevant example of this is

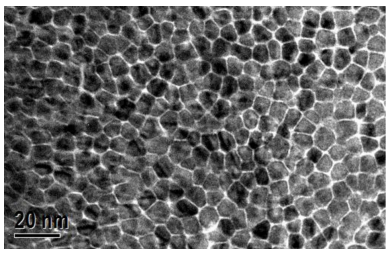

Figure 4.2: In-plane micrograph of CoCrPt recording layer with grains segregated by 1 nm of silica [123].

in perpendicular recording media where silica forms an exchange break between grains of CoCrPt as shown in fig. 4.2 [123].

4.1.1 Sputtered Thin Films

Sputtering has been a known phenomenon for over forty years but has faced many limitations in that time [120]. The first instance of sputtering was DC diode sputtering, where a several kV potential was applied across two plates to generate a plasma. By coating one electrode with target material and the other with a substrate, growth was achieved by the motion of liberated ions towards the cathode [124].

There are many methods for sputtering of thin films with widely varying benefits and challenges. One of the most popular methods for sputter deposition is magnetron sputtering [121]. In magnetron sputtering the confinement of secondary electrons to the target vicinity by a magnetic field is used to drastically improve ionisation probabilities as shown in fig. 4.3. Therefore far higher ion bombardment can occur and deposition rates are boosted.

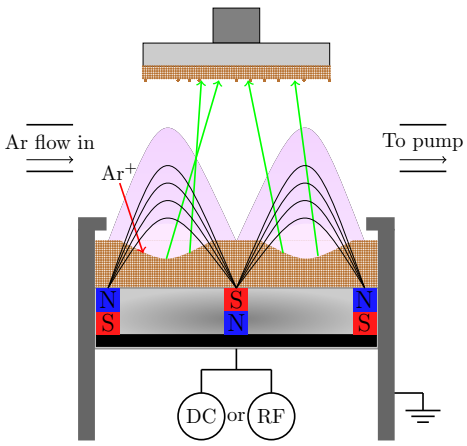

Figure 4.3: Basic schematic for a magnetron sputtering system.

The substrate is positioned just outside the dense plasma region for the deposition process as a high fluence of energetic particles during deposition can have significant effects on their growth [125, 126] but the high deposition rate of several Å/s must be maintained. However this can be exploited by modifying the design of the magnets to so called "unbalanced magnetron sputtering." Stronger outer than inner poles of the magnet array expand the plasma further into the chamber, thus trapping more ionising electrons and creating a secondary plasma at the surface of the substrate. This is then manipulated to control the growth process.

Alternatively, or additionally, a closed field magnetron can be created, caging the plasma and filling the region between target and substrate. This induces a high flux of low energy (<100 eV) impacts while decreasing losses of target material to

the chamber [127].

Magnetron sputtering suffers from severe limitations if magnetic targets are to be sputtered. Since the permeability of the target is so much greater than the chamber the flux is highly concentrated within the target. As such a very thin target must be used. Figure 4.3 also shows how the sputtering processes are concentrated in the intense glow regions of high field intensity.

This leads to an inhomogeneous sputtering which creates a so called "racetrack" which is shown in fig. 4.4. Due to the high cost factors involved in magnetic recording due to precious metal use, especially in $IrMn_3$, magnetron sputtering can become expensive.

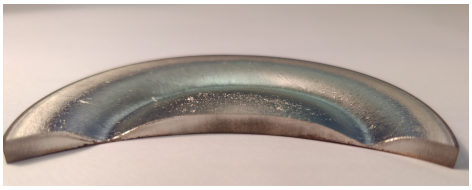

Figure 4.4: A tantallum target following magnetron sputtering.

4.1.2 High Target Utilisation Sputtering (HiTUS)

Remote production of a plasma away from the target simplifies the problem of economic use of targets and plasma control. This is the case in **Hi**gh **T**arget **U**tilisation **S**puttering (HiTUS), a modification of traditional magnetron methods which is shown in fig. 4.5. A side chamber with a 3 kW 13.56 MHz radio frequency (RF) field applied through a three turn coil generates an inductively coupled plasma [119, 128, 129].

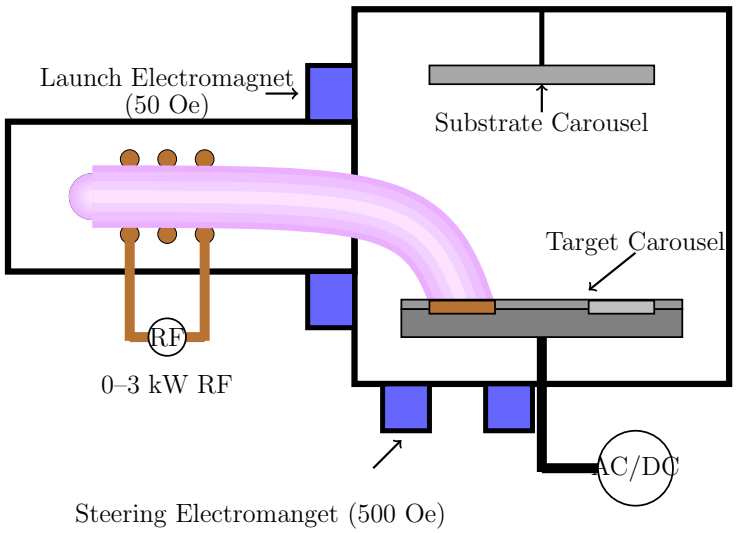

Figure 4.5: Basic schematic of the HiTUS system.

Diffusion of Ar^+ ions into the chamber occurs due to the partial pressure difference. A 50 Oe field applied coaxially to the coil accelerates the liberated electrons in a chiral motion leading to a large number of ionising collisions resulting in a highly intense plasma beam. It has been shown that the typical electron energy in the HiTUS sysytem is on the order of 65 eV compared to an ionization energy of Ar of 15.76 eV [130].

This allows for extremely high ionization densities of 1×10^{12} ions/cm^3 to 1×10^{13} ions/cm^3 compared to a magnetron plasma, where the typical density is 1×10^{10} ions/cm^3, as is shown in fig. 4.6 [130].

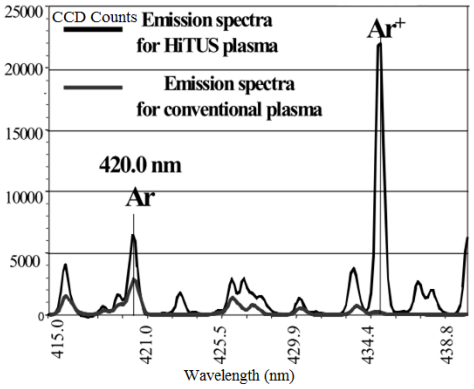

Figure 4.6: HiTUS and conventional magnetron plasma spectra [130].

Target sputtering is achieved by coupling the launch field of 50 Oe to a second "steering" DC magnetic field of strength 500 Oe. This confines the plasma to a beam and diverts it onto the target area of 20 cm^2 with approximately 95% target coverage. However the impact energy of the ions is at this point too low to cause liberation of target atoms.

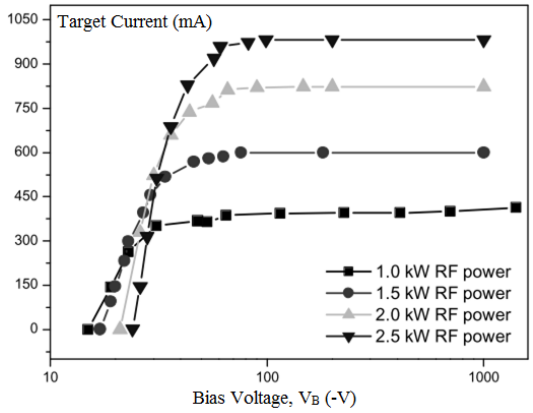

Figure 4.7: Target current vs. V_B for different RF powers showing saturation of at V_B over 100 V [130].

As such a negative bias voltage (V_B) of -1 V to -1000 V must be applied to the target table to accelerate the ion beam further. As shown in fig. 4.7 at all bias voltages >100 V the target current remains constant. Therefore the high plasma density at the target surface is maintained while the impact energy of the ions can be controlled by increasing the bias.

This adds a degree of freedom for controlling the sputtering process. As the target bias is increased the deposition rate increases due to higher ablation rates. The sputtering rate can also be adapted by varying the RF power applied to the argon to increase or decrease ion density. Similarly the process pressure of the argon can be controlled to affect the ion density [119].

This allows for controllable grain size deposition where the median grain diameter (D_m) can be manipulated as shown in fig. 4.8. By increasing the RF power, V_B or the process pressure the energy density of the plasma will grow, increasing the deposition energy. This leads to more mobile atoms being deposited onto the substrate increasing the size.

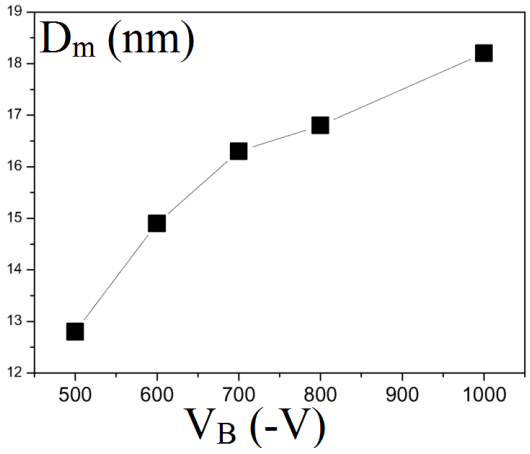

Figure 4.8: D_m vs. V_B showing the control over grain size in the HiTUS system [119].

Up to six substrates with sizes from 5 mm to 20 mm can be positioned above an eight target carousel which allows for multilayer deposition from either metallic, alloyed or, if a RF bias is applied, insulating materials. The RF bias is required as to prevent the charge build up in the surface of the targets. This allows for the deposition of multilayer structures where the properties of the plasma, and thus deposited films, can be varied between layers and depositions without breaking vacuum.

Since a magnetic field is not confining the plasma to a central ring on the target surface, the appearance of racetracks does not occur; hence the title High Target Utilisation Sputtering (HiTUS). As such this method is much more cost effective than magnetron sputtering. A second benefit to total coverage of the target surface is better stoichiometry in the liberated material. The sputtered films are much more representative of the target material. Additionally this allows for doping of the target material by the addition of "pegs" of dopant into the target, for example to modify the Mn content of IrMn for exchange bias measurements.

The large spacing of 30 cm between the target and substrate also offers several advantages. Firstly a large cone of sputtered, mixed material is produced covering a wide area. As such multiple substrates can be included for co-deposition, such as varied sizes or the addition of TEM grids. The deposition at the substrate carousel

is so uniform that TEM grids grown alongside a Si substrate will exhibit exactly the same gain size distribution. Additionally, there is no re-sputtering from the substrates as they are placed 30 cm from the target. This also keeps the deposition temperature low, often below 50 °C monitored by a thermocouple, which allows for controlled deposition.

If no V_B applied and the second electromagnet is turned off, the plasma floods the deposition chamber which has several benefits. Firstly substrates can be cleaned effectively using the plasma itself. The shutter can be opened to expose each of the substrates to the flooded chamber in turn for 60 s to 120 s; effectively cleaning the substrates of surface contaminants. Secondly the chamber walls are exposed to the plasma liberating any surface contamination. Since the Ar flow is constant, this is removed by the pumping mechanism and as such the chamber is effectively cleaned. As such the relatively high base pressure of 5×10^{-7} mbar is more than adequate which in turn allows for frequent target and substrate changes without the need for lengthy pumping protocols.

A 120 W bulb behind the substrate carousel allows for the deposition temperature to be varied up to 500 °C. The sample can be heated before, after or during the growth process. The use of one or more of these heating periods enable variation of deposition energy and hence control over properties, especially crystallisation. The combination of these tuning parameters results in a flexible deposition system where the grain size, roughness and crystallinity can be controlled [119].

4.1.3 Electron-beam Physical Vapour Deposition (E-beam)

Electron-beam physical vapour deposition (e-beam) is an alternative method to deposit thin layers [131]. Similarly to HiTUS there is an external source of energy, however this time it is in the form of an electron beam. Rather than using bombardment to liberate target material, the electron beam is used like a thermal evaporator, heating the surface of the target locally to above the vapour pressure.

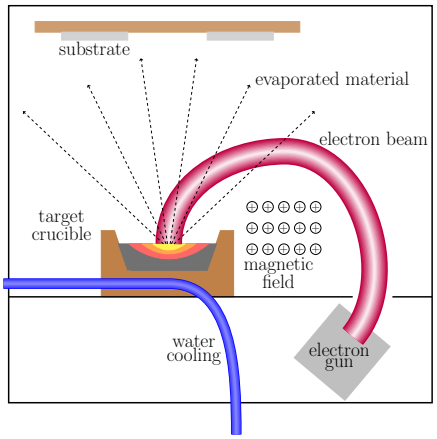

Figure 4.9: Simple schematic of an e-beam evaporator.

The electron beam is generated in the usual fashion from a tungsten filament below the target and is then directed using a magnetic field onto the surface of the target as shown in fig. 4.9. The target is housed in a crucible with water cooling, helping to control the deposition direction and prevent the target over-heating. The filament is kept out of the line of sight of the substrates to avoid contamination or reaction of the filament material.

Deposition rates can be varied from 1 nm/min all the way up to 1 µm/min so the range of applications is broad, from thin films to industrial coatings. Additionally the e-beam is widely used as an etching or fabrication tool due to the high impact energies coupled with very high spatial resolution [132, 133]. In this work a JEOL JBX-6300 FS with a BEAMER attachment from GenISys GmbH has been used to pattern GMR devices and subsequently deposit electrodes of Ti and Au for device measurements and is further discussed in section 4.4.

4.2 Structural Characterisation

As discussed in chapter 3, the structural properties of Heusler alloys are crucial to their magnetic properties and device performance. As such precise and reliable measurements of the crystallographic and material properties must be made. For crystallographic characterisation one of the leading tools is the X-ray Diffractometer (XRD) which allows for determination of the crystal structure of the sample and whether this structure is local, global or somewhere in between. A variant of XRD called X-ray Reflectometry (XRR) has been used to determine a sample's relative density and its substrate, interfacial and surface roughnesses.

Transmission electron microscopy (TEM) can be used to determine the median grain size (D_m) and grain size distribution of a material in order to explain its magnetic properties. Additionally cross-sectional TEM has been used to determine roughness and diffusion in thin-film and device structures.

The discussions of these instruments follow the book *Elements of X-Ray Diffraction* by B.D. Cullity [134] and the Rigaku hand book for XRD [135–142]. *Transimission Electron Microscopy* by Williams and Carter [143] and JEOL releases for the TEMs have also been used.

4.2.1 X-ray Diffractometry

X-ray diffraction is summarised by Bragg's law [144]

$$n\lambda = 2d\sin\theta_B \tag{4.1}$$

where n is the order of the diffraction, λ is the wavelength of the incoming radiation, d is the lattice plane spacing and θ_B is the angle at which diffraction occurs. The lattice spacing d in a cubic structure is given by

$$d = \sqrt{\frac{a^2}{h^2 + k^2 + l^2}} \tag{4.2}$$

where a is the lattice constant and h, k and l are the Miller indices specifying the lattice plane.

The X-rays used in this work are Cu-K_{α_1} with a wavelength of 0.154 059 nm. A tungsten (W) cathode is used to generate an electron beam that is accelerated toward a rotating Cu anode whereby electrons interact with the Cu and generate X-rays. The anode is rotated in order to minimise the heating since the device power is typically 1.76 kW but can be up to 9 kW [145] for the system used in this work which is a Rigaku SmartLab [146].

The X-rays generated in this way are not monochromatic with Cu-K_β, W-L_{α_1} and W-L_{α_2} all being generated as well as both Cu-K_{α_1} and Cu-K_{α_2}. Therefore either a Ni filter must be used or a monochromator added the optics. A Ni filter will remove the Cu-K_β, W-L_{α_1} and W-L_{α_2} lines effectively with the intensity of the Cu-K_β reduced by 90%. However there will also be a loss of 30% in the Cu-K_{α_1} peak and no removal of the Cu-K_{α_2}.

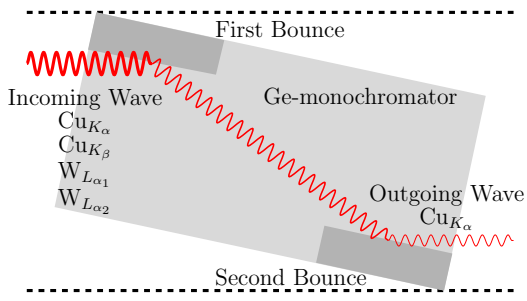

Figure 4.10: A schematic of a 2-bounce Ge monochromator.

The monochromator is a two-bounce, channel-cut Ge single crystal where the incident beam is reflected and diffracted twice from the same set of lattice planes. Since the Bragg condition is so precise, the Cu-K_{α_2} peak is removed in addition to the others. The resultant beam is therefore highly monochromatic and also parallel with

the incident beam and therefore easily aligned. This allows for a resolution of 0.01° but the resultant beam is also a factor of 100 less intense than the incident beam. Resolution of 0.003° can be achieved using a four-bounce monochromator but then the resultant intensity is reduced by another order of magnitude.

To reduce beam divergence a Soller slit can be introduced on both the incident and reflected sides of the optics. A soller slit consists of multiple, parallel foils which are parallel to the diffraction planes. The width of the slits is often quoted as an angle, but can be quoted in mm. The resultant divergence is often on the order of 5° and is generally given by

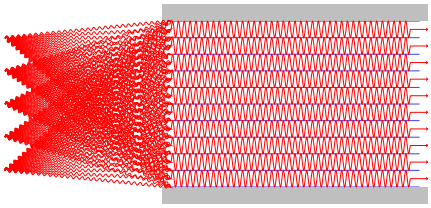

Figure 4.11:
Schematic view of a soller slit.

$$\alpha_{Soller} = \frac{2x_S}{l_S} \tag{4.3}$$

where α_{Soller} is the divergence, x_S the slit width and l_S the length of the soller slit. An example of a Soller slit is shown in fig. 4.11. The effect of this is to improve the peak profile, reducing asymmetry especially at low θ scattering angles.

Additionally a parallel slit analyser (PSA) can be used to determine the resolution of the scan. These differ to soller slits in that the foils are perpendicular to the planes of diffraction, however they are often unnecessary when a monochromator is used, especially given that the beam intensity is further reduced by another order of magnitude by finite slit widths.

There are several selection slits that dictate the beam profile: one on the incident side and two on the receiving side. The incident slit allows for the beam to be focussed onto the sample in order to reduce any signal from the sample mount. The two receiving slits are set as narrow as possible in order to maximise the angular resolution as shown in fig. 4.12. However once more compensation must be made for a reduction in count rate proportional to the slit widths. There are also a possibility of a peak shift if the sample height is incorrect, so accurate alignment is crucial.

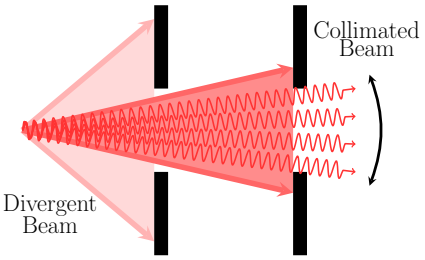

Figure 4.12: Collimation of a beam by receiving slits.

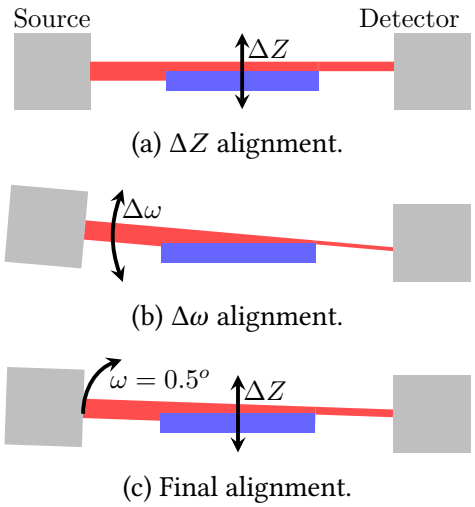

(a) ΔZ alignment.

(b) $\Delta\omega$ alignment.

(c) Final alignment.

Figure 4.13: The three stages of sample alignment.

Sample alignment is paramount to obtain reliable scans with no angular offsets, but also to maximise the signal so that measurement times can be minimised. Sample alignment takes place in three parts as shown in fig. 4.13. Firstly the sample height (Z) is adjusted such that the detector receives half-full beam intensity. Secondly the incident angle (ω) is varied to maximise the intensity at the optimised Z height. Finally Z is then moved to maximum intensity at a grazing incident angle of 0.5°.

XRD measurements are best represented using a concept known as the reciprocal lattice and reciprocal space. This represents a set of planes as a vector. If a set of planes has spacing d_{hkl} then this can be represented by a reciprocal lattice vector g_{hkl} which is normal to the planes and of magnitude $1/d_{hkl}$. This lattice ends in a point known as the reciprocal lattice point. The reciprocal vectors of each set of planes all have a reciprocal lattice point. All of these together form a reciprocal lattice [134].

The incident and outgoing wavevectors k_0 and k_g are related to g_{hkl} by

$$k_g - k_0 = g_{hkl} \tag{4.4}$$

which is easily rewritten back into the form of eq. (4.1) if the wavelengths of the X-rays are λ. In other words when the conditions of eq. (4.1) are met the resultant vector K_R is equal to g_{hkl}.

4.2.2 General XRD Measurements

There are several geometries of measurement possible that give the basic information about a crystal, namely the lattice planes perpendicular to the scan geometry. The most common measurement is a $\theta - 2\theta$ measurement shown in fig. 4.14. The incident beam angle θ

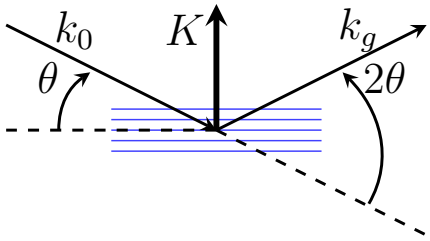

Figure 4.14: The $\theta - 2\theta$ measurement geometry.

and receiving detector angle 2θ are scanned symmetrically with the scattering vector K_R perpendicular to the sample surface. Therefore the Bragg conditions met here are for planes parallel to the sample surface. From these out-of-plane measurements it is therefore possible to identify the lattice constant, strain and crystallographic orientation out-of-plane of a sample.

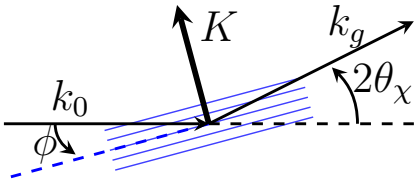

Figure 4.15: Planar view of the $2\theta_\chi/\phi$ measurement geometry.

The equivalent to the $\theta - 2\theta$ for the lattice planes normal to the sample surface is the $2\theta_\chi/\phi$ measurement geometry shown in fig. 4.15 from the top down. The detector arm is moved at an angle of $2\theta = 0$ around the sample on the axis labelled $2\theta_\chi$. In order to maximise the signal the θ axis is set to an angle of 0.5° as in the sample alignment. As the $2\theta_\chi$ axis is scanned the sample is also rotated at half the speed on an axis denoted ϕ. This ensures that the same crystal planes are being measured throughout and keeps symmetry with a $\theta - 2\theta$ measurement. As such this in-plane measurement gives information on the lattice constant, strain and crystallographic orientation in the sample plane.

4.2.3 Textural Analysis

$\theta - 2\theta$ and $2\theta_\chi/\phi$ measurements give a general idea of the crystal structure in a sample. However if more detail is required then further scans must be carried out.

The dispersion of the lattice planes parallel to the sample can be obtained using a rocking curve as shown in fig. 4.16. The 2θ axis is set to the known value from the $\theta - 2\theta$ and the scattering vector is then rocked over the surface normal through Ω. This gives a distribution of the angles of planes relative to the surface normal and as such a measure of the level of texture in the sample. A perfect epitaxial crystal will have a very narrow distribution with a full-width half-maximum (FWHM) approaching zero. For a well-textured film the FWHM should be below 10° and preferably 5°.

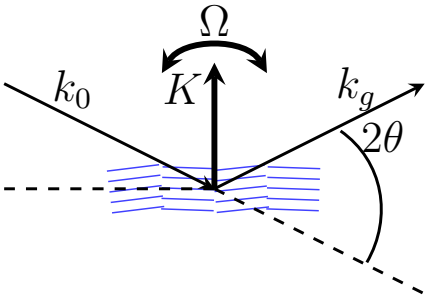

Figure 4.16: The rocking curve measurement geometry.

By adding a second rotation axis to the sample stage χ which is orthogonal to ϕ a pole figure scan can be constructed. This is in essence a 3-D extension of the rocking curve. By fixing K_R with the θ and 2θ axes and rotating the sample through χ and ϕ a 3-D plot can be mapped of the reflections in the sample. A complete random polycrystalline structure will give an even distribution, i.e. there is no preferred orientation. If there is some 2-D random texture whereby a given set of $\{hkl\}$ planes lie parallel but not collinear then a ring will appear at given χ depending on the exact values of $\{hkl\}$. For a single crystal these rings collapse to points at a specified ϕ.

4.2.4 X-Ray Reflectometry (XRR)

The wavelength of the Cu-K_α used is below 0.2 nm and as such has a refractive index <1 for many common materials. Therefore a density dependent critical total internal reflection angle (θ_C) will occur. This allows for precise determination of the density of a thin film when scanning θ in the range 0.2° to 0.5°. Beyond this range refraction occurs and the amplitude of the outgoing X-ray decreases by a factor 4.

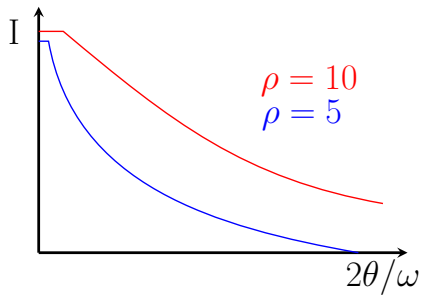

Figure 4.17: The effect of density on the reflectivity of a film.

If θ is then scanned past θ_C a reflectivity profile can be taken. The profile is dependent on several factors. The density of the film, as mentioned above, determines the critical angle for the reflectivity. Furthermore the density determines the rate of decay of the reflectivity with ω, with a greater density leading to a greater reflectivity and as such a longer profile as shown in fig. 4.17.

The periodicity of the profile is controlled by the layer thickness with thicker layers having a higher frequency of oscillation as shown in fig. 4.18. When multiple layers are present the periodicities sum, making determination of layer thicknesses difficult in complex systems. Furthermore there is less certainty of a unique solution, so care must be taken with fitting.

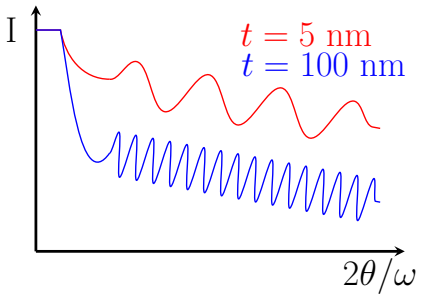

Figure 4.18: The effect of layer thickness on a film's reflectivity.

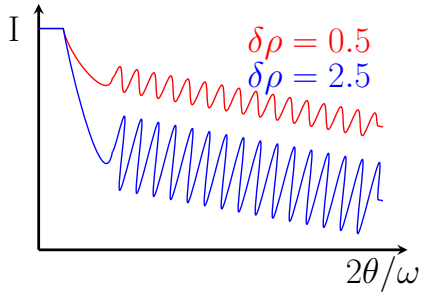

Figure 4.19: The effect of density variation between layers on the XRR profile.

Figure 4.19 shows how density changes from layer to layer affect the amplitude of the oscillations. When two materials of similar density are layered there is very little amplitude oscillation. This adds a further limitation to fitting parameters, especially if both the layer densities and thicknesses are similar.

The surface roughness of the film dictates the rate of intensity decrease at the critical angle. With a rougher surface, the intensity can drop significantly more, by up to a factor 10. The surface roughness also influences the tail end of the reflectivity profile, with a larger roughness causing a loss of periodicity more quickly as shown in fig. 4.20.

Interfacial roughness is also responsible for the rate of decay of both the profile and the amplitudes of the oscillations. A rough film will have a short lived reflectivity profile where the oscillations are extremely weak compared to a film with smooth interfaces.

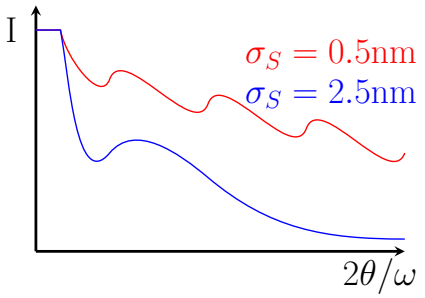

Figure 4.20: The effect of surface roughness on reflectivity.

It is evident that many of these parameters affect the same profile properties. Therefore extreme care must be taken with fitting regimes to ensure that the solution is both accurate and unique. However, despite these limitation XRR remains a powerful tool for identifying long range structure in thin film structures both qualitatively for profile comparison and quantitatively when fitting is performed. Fitting is undertaken using the Rigaku GlobalFit software [147] or GenX [148, 149].

4.2.5 Transmission Electron Microscope

TEM is a powerful tool for analysing structures at the atomic scale. A high-energy electron beam interacting with a thin-film specimen will produce a large array of signals, as shown in fig. 4.21. For TEM imaging it is the direct beam and the elastically scattered electrons that are used. Two sources of interaction

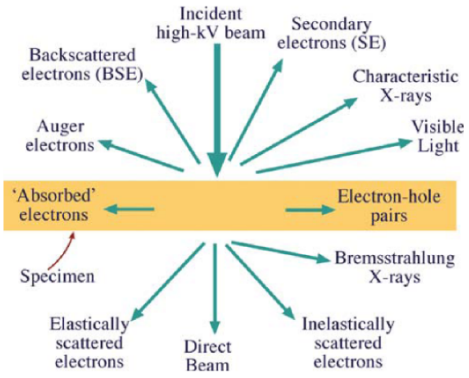

Figure 4.21: Electron interactions with a thin-film sample [143].

dominate generations of contrast in the elastically scattered beam. Firstly mass contrast gives Rutherford-like scattering in the specimen where the scattering is proportional to the proton number squared, Z^2. This is low angle scattering <0.5° and is called mass contrast [143].

Voltage (kV)	Classical λ_e (pm)	Relativistic λ_e (pm)
100	3.86	3.70
200	2.73	2.51
300	2.23	1.97
1000	1.22	0.87

Table 4.1: The relatavistic correction to high-energy electrons.

The second form of contrast is due to the diffraction of electrons. This is directly analogous to X-ray diffraction and eq. (4.1) can be immediately rewritten as

$$n\lambda_e = 2d\sin\theta_B \tag{4.5}$$

where λ_{X-ray} is directly replaced with the electron wavelength λ_e. Since the electrons used in TEM are of a high-energy of the order of 200 kV it is important to note that they must be treated relativistically as shown in table 4.1. In the JEOL TEM 2011 system used in this work the electrons are at an energy of 200 keV.

The construction of a TEM is complicated and a simplified schematic is shown in fig. 4.22(a). Since charged particles are used, the lenses for focussing the beam are electromagnetic. A combination of a copper coil with pole pieces ensure that a focussed, thin-converging lens is created by the flux along the beam direction. Therefore any charged particles travelling off the desired axis will feel a Lorentz force

$$F = e(\overline{v} \times \overline{B}) \tag{4.6}$$

where $\overline{v}$ is the electron velocity and $\overline{B}$ the magnetic field of the lens. This creates a helical motion drawing the electron towards the desired axis. By varying the field strength the focus can be shifted for changing the magnification of the image

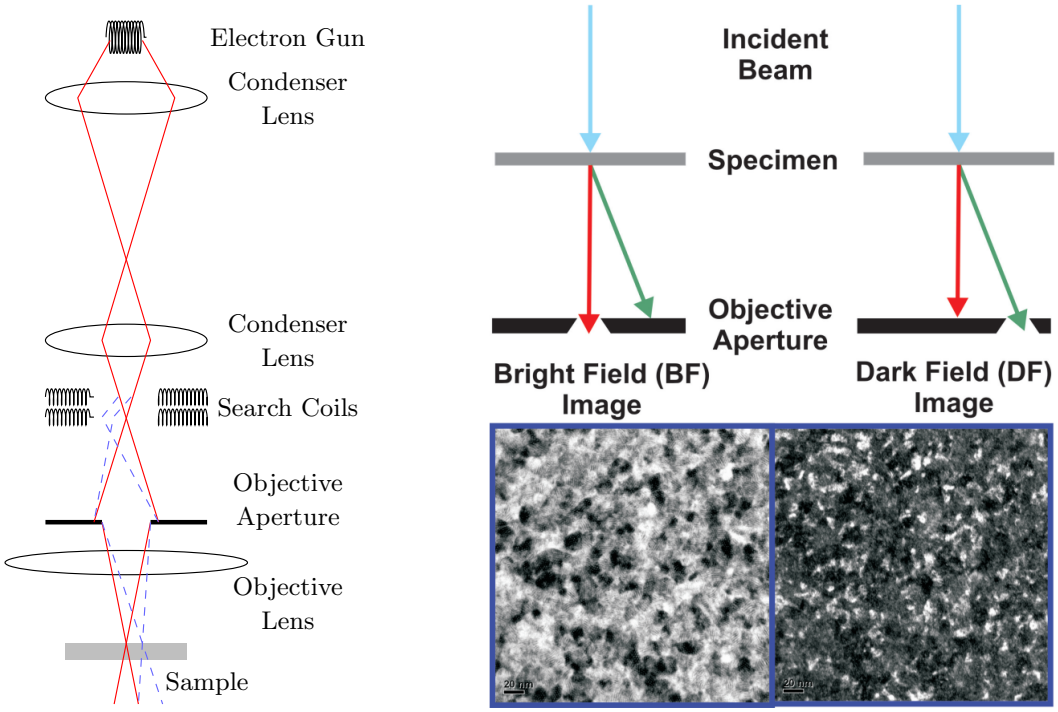

(a) A TEM.

(b) Bright and dark field TEM [143].

Figure 4.22: (a) A schematic of a basic TEM and (b) the bright and dark field operation modes with example imagnes from both.

and for different sample alignments [143]. The beam can be redirected around the sample space by deflecting the beam with a pair of search coils as shown in blue in fig. 4.22(a).

The TEM has two detectors called bright field and dark field, which are two of the possible operating modes shown in fig. 4.22(b). The difference between these modes is achieved by the use of an objective aperture. In bright field imaging only the transmitted electrons are viewed and in dark field only the diffracted. This leads to two opposing contrast techniques where preferential crystal directions are viewed. This is of great benefit for analysis of grain and crystallite sizes and structures [143].

4.3 Magnetic Measurements

Magnetic characterisation of samples comes in many forms. Closed loop magnetic measurements can be performed where the sample completes a magnetic circuit. This is the case for a *B-H* loop tracer, also known as a direct current (DC) or alternating current (AC) permeameter depending on the design. However in

these systems there are often severe limitations such as sample size or shape, the maximum applied field or the inability to vary parameters such as the temperature or applied field angle [45].

The more common and versatile alternative are open magnetic circuit measurements. The open design allows for the use of large, high-field electromagnets with fields upwards of 8 T being commercially available. Two powerful open circuit measurement techniques are the Alternating Gradient Force Magnetometer (AGFM) and the Vibrating Sample Magnetometer (VSM) [45].

4.3.1 Vibrating Sample Magnetometer

The VSM was first suggested by Simon Foner in 1959 [150]. In order to measure a magnetic signal in an open circuit, the VSM utilises Faraday's law of induction [45]

$$\epsilon = -N\frac{d\phi_m}{dt} \tag{4.7}$$

where ϵ is an induced voltage in a coil of N turns when exposed to a changing magnetic flux $d\phi_m$ in a time dt. ϕ_m through a set of coils with area A_C is given by

$$\phi_m = (H + M) \cdot A_c \tag{4.8}$$

where H is the applied magnetic field and M is the magnetisation of the sample. In the Microsense Model 10 VSM used the maximum value of H is either 20 kOe or 30 kOe depending on the pole pieces used and their separation. Since H is non-variant with time then when eq. (4.8) is applied to eq. (4.7) the induced voltage simply depends on the sample magnetisation and the frequency of the vibration

$$\int \epsilon \cdot dt = -NA_c \cdot M \tag{4.9}$$

In order to generate the alternating flux the sample is attached to a vibrating rod. This has the added benefit of enabling lock-in detection methods to be used since the oscillation is at a set, known frequency. This frequency is often in the range 70 Hz to 90 Hz to avoid harmonics of mains electricity voltages, with 81 Hz as a popular choice. The placement of the vibrating sample within the detection coils is shown in fig. 4.23.

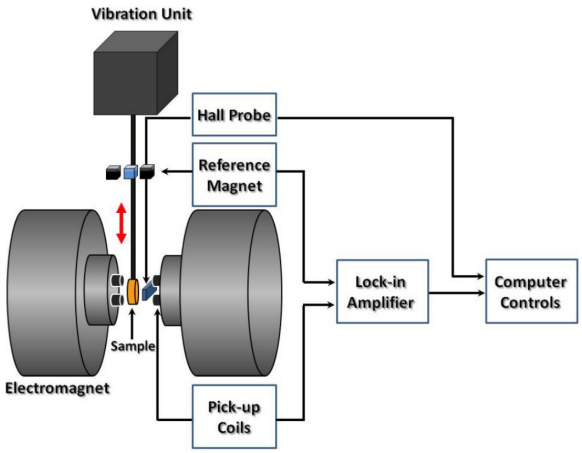

Figure 4.23: Schematic diagram of a VSM.

In order to reduce the noise in the system a reference system with a capacitor is added above the electromagnet with its own detection coils. Since the reference magnet is vibrated identically to the sample comparison of the reference and detection coils is independent of any external changes. Furthermore in the Microsense Model 10 VSM the detection coils are mechanically decoupled from the vibrations by being housed on anti-vibration pads. However since the sample is rapidly vibrating a static charge can build up on the surface. This must be removed to be able to measure a signal and this is achieved by having an anti-static fan blow directly over the sample space. As such the sensitivity of a modern VSM is on the order of 1×10^{-9} emu [151].

For measurements perpendicular to the sample there are two ways to adapt the geometry in the Microsense system. The first and simplest solution is for a sample rod to be used which oscillates the sample in the correct orientation shown as probe (c) in fig. 4.24. However it is also possible to have an electromagnet pair which rotates around the sample itself. This has the added benefit of enabling the sample to be measured in any geometry between in- and out-of-plane whilst also not requiring any change of sample mount, keeping conditions identical on a probe of orientation shown as either (a) or (c) in fig. 4.24. This does require extra calibration steps for the varying applied field angles. A transverse probe as shown in fig. 4.24(a) can also be used for purely in-plane measurements. The rotational degree of freedom allows for determination of preferential magnetisation directions, however this is more applicable for highly textured/single crystal samples.

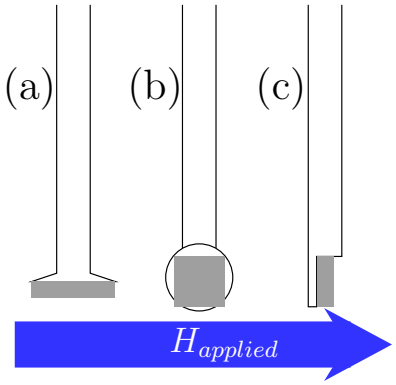

Figure 4.24: The (a) transverse and (b) in-plane and (c) out-of-plane lollipop VSM probes.

Calibration is a key issue in all magnetic measurements. For the VSM a palladium foil with $\chi \approx 5 \times 10^{-7}$ emu/Oe is used to calibrate the detection coils in the

system. Since palladium is a Pauli paramagnet its magnetisation is well defined at any field value. It is also highly corrosion resistant. It is possible to use a nickel sample to calibrate the moment. However this has only one defined point for a given sample at the saturation magnetisation M_S. Furthermore the nickel is prone to corrosion in comparison to palladium and any cleaning of the sample reduces the reliability of the known moment. Field calibration is performed in two steps. Firstly the zero point is set by placing the Gauss probe from the VSM into a zero field shield. The Gauss probe is then comparatively calibrated to a secondary standard Gaussmeter in a series of field sensitivity ranges and field values.

4.3.2 Alternating Gradient Force Magnetometer

The AGFM is a highly sensitive, delicate instrument capable of extremely fast magnetic measurements, making it ideal for thin film characterisation [152, 153]. The principle of the system is extremely simple and uses the force exerted on a magnetic moment when in the presence of a field gradient. This is given by

$$\overline{F}_M = \overline{m} \cdot \nabla \overline{H} \tag{4.10}$$

where $\overline{F}_M$ is the force exerted on the moment $\overline{m}$ by the gradient of an applied AC field $\nabla \overline{H}$ [152]. This gradient field is produced by a pair of small coils within the DC field applied for hysteresis. The deflections caused by $\overline{F}_M$ are extremely small and as such require a highly sensitive probe. This is achieved by the sample being mounted to a piezoelectric bimorph via a pair of quartz fibres whereby $\overline{F}_M$ induces a voltage.

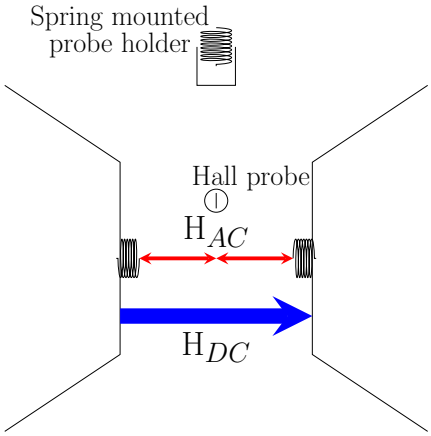

Figure 4.25: DC and AC fields in an AGFM.

In order to increase the signal output an alternating gradient field must be applied within the DC field. As shown in fig. 4.25 the AC field gradient is applied by two small coils within the poles of the electromagnet. The magnitude of the gradient can be set to 0.04 Oe/mm, 0.4 Oe/mm and 4 Oe/mm. The gradient is a maximum at the centre of the pole gap. To achieve this the two alternating coils are aligned north-north. In order to minimise the variation in applied field the smaller the gradient applied the more accurate the result. If a

4 Oe/mm field gradient is applied to a 5 mm sample then the field at the centre of the sample will be 10 Oe smaller than the field at the edge.

This can have significant effects in soft magnetic samples like Heusler alloys [154]. At a given temperature there is an effective field due to thermal energy called the fluctuation field [54, 56] given by [57]

$$H_f = \frac{k_B T}{Q} \tag{4.11}$$

where H_f is the fluctuation field at a temperature T and k_B is the Boltzmann constant. Q relates the field and energy by being an effective magnetic moment, i.e. a magnetisation per unit volume. In this case the volume will be that of an activation volume for the coupled grains which nucleate the reversal process [57].

However as shown in fig. 4.26 this is also the case for CrO_2 fine particle film with no intergranular exchange. In this case the volume will be that of a single particle. This thermal field can be quantified and at room temperature is found to be approximately 16 Oe. Therefore at the edge of a 5 mm sample with a 4 Oe/mm field gradient the alternating field is effectively a 67% increase in the thermal energy. This means that the coercivity of the film at the edge of the sample will become equivalent to that of the same sample heated to 500 K. Experimentally the coercivities of films have been found to fall significantly as shown in fig. 4.26 [154].

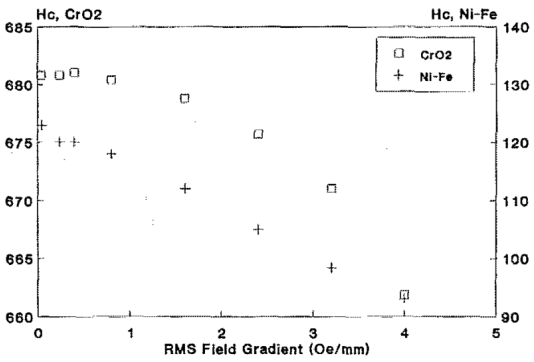

Figure 4.26: Variation of coercivity with field gradient in an AGFM [154].

However this must be balanced with the decrease in $\overline{F}_M$ when using a smaller gradient since F_M is directly proportional to ∇H and as such 0.4 Oe/mm is often the optimised condition for the in-plane direction. When measuring out-of-plane the sample is far thinner and as such gradients of 4 Oe/mm can, and must often, be used.

The AC field can be tuned to the resonance of the system which is in the range 100 Hz to 1000 Hz, with higher frequencies better resisting background vibration [152]. Naturally this has a significant effect on the amplitude of the voltage induced by the bimorph. Since this signal is now at a known frequency, lock in amplifica-

tion can be used to reduce background noise significantly. As such the AGFM is one of the most sensitive magnetometers available with a noise base on the order of 2×10^{-8} emu [152].

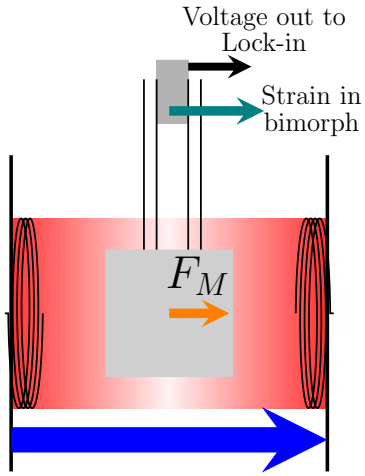

Figure 4.27: The principle of operation in an AGFM.

Since the noise is so low and the aquisition so quick, due to being measured around 400 Hz, a hysteresis loop with a maximum applied field (H_{app}) of 1 kOe and a field resolution of 10 Oe can be taken in 120 s with an averaging time of 100 ms/point. The operation of the AGFM is summarised in fig. 4.27.

The fast, repeatable measurements are ideal for certain parameters [154]. In this work the AGFM has been used to measure time dependent magnetisation effects and nested minor hysteresis loops for the construction of direct current demagnetisation remanence (DCD) curves, an example of which is shown in fig. 4.28. This will be discussed further in section 4.3.3.

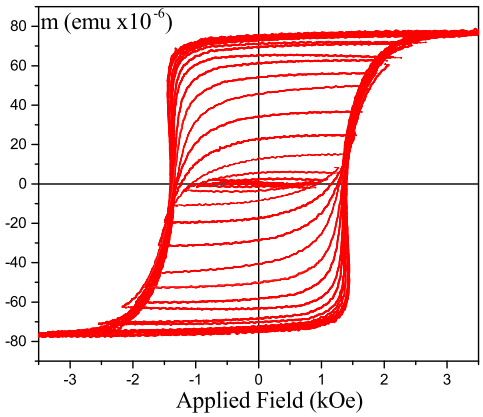

Figure 4.28: Nested minor loops of a CoCrPt-SiO_2 film taken by AGFM.

The high sensitivity of the equipment does add some limitations. Since the piezoelectric is so sensitive to vibrations the measurement must be carried out in a quiet room. Insulation in the form of a shield or expanded polystyrene can also be added to reduce noise. Noise has been reduced even further to a base of 1×10^{-9} emu by placing the assembly inside an evacuated bell jar. Additionally this means that most conventional methods of heating or cooling a sample cannot be applied, meaning that AGFM is unusable to determine temperature effects without significant modification [154]. Furthermore the mass of the total system must be <100 mg as to not totally damp the signal amplitude or to pull the resonance below 100 Hz [152].

Due to the nature of the design the probes for in-plane and out-of-plane geometries are different. For in-plane measurements two legs can be attached to the bimorph, one on each side, in order to apply the torque. This has a significant advantage in increasing both the amplitude and the quality factor (Q) of the

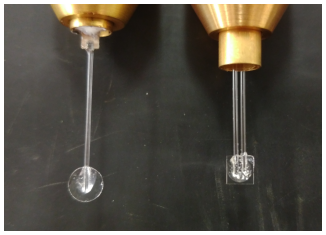

Figure 4.29: Different probes for out-of-plane and in-plane AGFM.

resonance in the probe. This is given by

$$Q = \frac{f_0\,(V_{max})}{f_B\left(\frac{V_{max}}{2}\right) - f_A\left(\frac{V_{max}}{2}\right)} \tag{4.12}$$

where the numerator is the resonant frequency and the denominator the full-width half maximum [152]. However for out-of-plane geometries there can only be one fibre and the fibre must be indented into the bimorph itself. The difference between the two is shown in fig. 4.29. The effect of this is to reduce the previously quoted sensitivity of 2×10^{-8} emu to approximately 1×10^{-6} emu. This is because the resonant of the peak is widened significantly and, as per eq. (4.12), this greatly reduces Q and therefore the signal.

4.3.3 Isothermal Remanent Magnetisation (IRM) and DC Demagnetisation (DCD) Curves

Isothermal remanent magnetisation (IRM) and DCD curves are two routes to determining the irreversible magnetisation of a material. This deconvolves it from the reversible switching and gives a true value for the irreversible susceptibility (χ_{irr}) which is the differential of each curve as shown in fig. 4.30. This also shows the difference between the two measurements - an IRM curve is taken from a demagnetised state and a DCD curve from a saturated one.

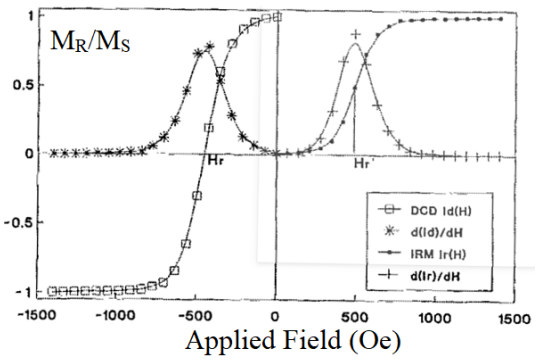

Figure 4.30: Example data for an IRM and DCD curve [154].

A DCD curve us taken by saturating the sample in one direction and then applying sequentially larger reverse field and measuring the moment when the field is removed. However, when measuring samples out-of-plane the demagnetising field becomes significant and must be accounted for. Additionally this must be balanced with the inter-granular coupling field.

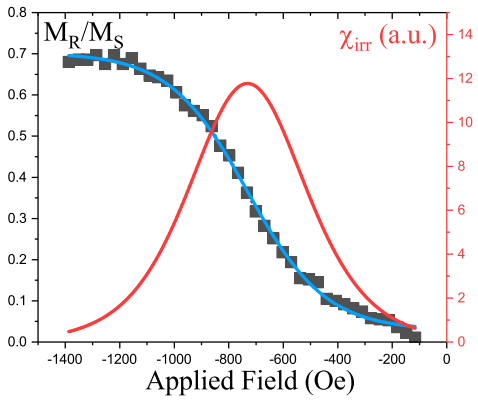

Figure 4.31: Example of a DCD curve of a perpendicularly magnetised Heusler alloy film.

A series of 40 minor loops is taken in decreasing field and the remanence taken in the negative to positive field direction. The remanence as a function of field can then be plotted and fitted with a sigmoidal function. The differential of this gives the χ_{irr} for the film. By normalising the curve to one, the switching field distribution (SFD) of the film is determined. An example of a DCD curve with its fit is shown in fig. 4.31.

4.4 Preparation of Heusler Alloy GMR Devices

Over the past 60 years semiconductor devices such as CMOS circuits have integrated into every aspect of modern life, from laptops and computers to tablets and mobile phones. As a result of this the fabrication methods of these devices have been thoroughly optimised by industry. This has been further amplified by the demand for more and more dense data storage in the form of hard-disc drives. The read-head fabrication has had to become more sensitive, accurate and reliable in order to meet increasing storage and speed demands [155]. For an in depth review of the subject of lithography, the interested reader can refer to *Electron Beam Lithography* by Z. Zhou [156].

In this work GMR devices based on silicon wafers have been fabricated at a joint facility in the University of Leeds. The main tools for the preparation of samples were the JEOL e-beam lithographic tool (JEOL JBX-6300FS) discussed in section 4.1.3 and Ar-ion milling. There are many methods for fabricating devices such as optical lithography, however due to availability of equipment the discussion that follows will focus on the available tools. Due to the remote nature of the equipment and the requirement for expert knowledge and training, the process optimisation and fabrication were undertaken by Dr. M. Samiepour.

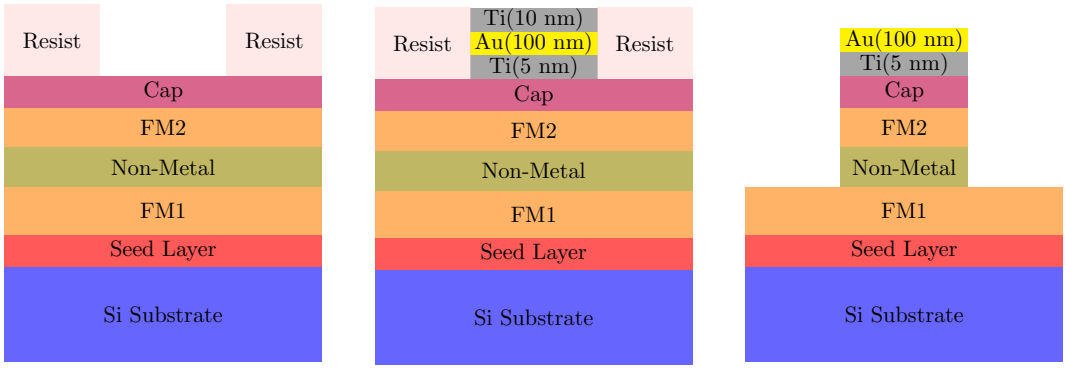

(a) Lithography of the mask for metallisation.

(b) Metallisation of the sample surface.

(c) Ar-ion milled sample, removing top Ti layer.

Figure 4.32: (a) Lithography, (b) metallisation and (c) Ar-ion milling of GMR thin films for device fabrication.

4.4.1 Sample Fabrication and Preparation

The first step of fabrication was to add a metallic mask to the samples using e-beam evaporation. After e-beam exposure and development a metallic mask can be deposited, also using the e-beam. The metallic mask consisted of three layers: Ti (5 nm), Au (100 nm) and Ti (10 nm). The thickness of the top layer of Ti was chosen as to be completely removed during ion milling leaving just a GMR pillar and a Au top contact for device measurement. The process is summarised in fig. 4.32.

Samples were fabricated in 3×3 arrays of chips. Each chip contained 8 elliptical pillars with decreasing dimensions from 1000 nm to 150 nm in the major axis and 500 nm to 100 nm in the minor, as shown in fig. 4.33(a). The elliptical shape of the pillars gave a preferential magnetisation direction or easy axis for in-plane measurements. However in the out-of-plane orientation the film thickness of 10 nm to 50 nm was still significantly below the in-plane dimensions so remained a hard axis unless perpendicular anisotropy was induced. A scanning electron microscope (SEM) image of a typical 300 nm pillar is shown in fig. 4.33(b).

An insulating layer was added to isolate the pillar from the leads to be connected to it. This was achieved by covering the pillar in a layer of crosslinking PMMA into which a hole smaller than the pillar area was bored using an O_2 plasma. E-beam lithography was used to deposit the bottom contacts as $2\,\mu m \times 4\,\mu m$ rectangles of Au. The top contact, insulating PMMA and bottom contacts are shown in the micrograph in fig. 4.33(c).

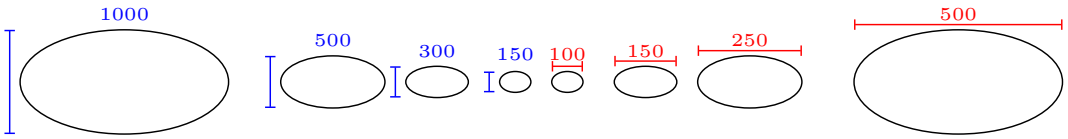

(a) Dimensions of the pillars on a chip, given in nm.

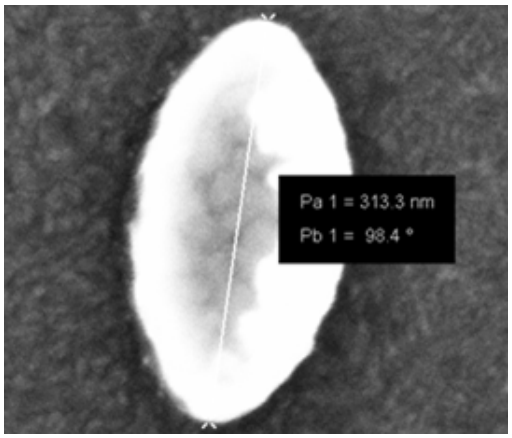

(b) An SEM image of a 300 nm pillar.

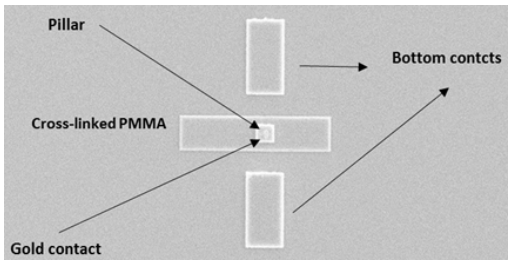

(c) SEM micrograph showing the pillar with top and bottom electrodes.

Figure 4.33: (a) Schematic and (b) SEM images of the elliptical pillar devices and (c) how the electrical contacts for measurement are arranged and bonded.

An insulating layer of SiO_2 was deposited using e-beam and then patterned to expose the top and bottom contacts. Reactive ion etching (RIE) with CHF_3 and Ar was used to expose the contacts. Inner contacts lines of Au were then added using e-beam lithography before finally large contact pads were added using optical lithography. All of the pillars shared bottom contacts with four available contact pads and each pillar had two top contact pads to the top electrode to allow for 4-point measurements, as discussed in section 4.5. This lead to a total of 20 contact points for sample measurement.

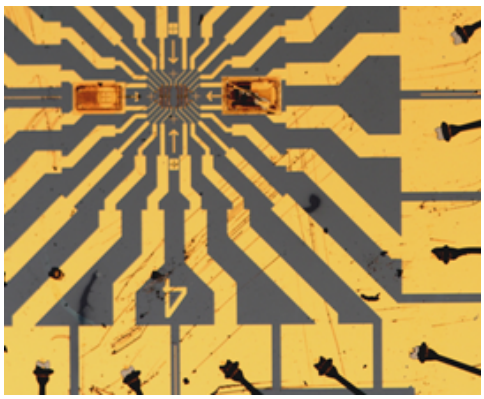

Figure 4.34: The final form of the chip wire bonded to a chip carrier.

The chips were then separated by etching and cutting the sample with a diamond tipped scribe. Each chip was then glued using Ag-paint into a 20-contact ceramic-chip carrier with Au contacts. The chip was then wire-bonded to the carrier using Au wire in a wedge bonder as shown in fig. 4.34. A wedge bonder is advantageous over a ball bonder since it uses only force and heat to bond a wire. The electrical discharge in a ball bonder can be damaging to devices and is as such less desirable.

4.5 Electrical Measurements

Electrical measurements of materials generally are divided into two categories; those of bulk and thin films and those of patterned device structures. In the case of Heusler alloys the variations in density, crystallisation and stoichiometry in a polycrystalline film limit this choice. Effects such as magnetoresistance or spin polarisation are overwhelmed by granular and crystallographic effects in a film. Therefore the measurements undertaken for GMR were of devices.

4.5.1 4-point Electrical Measurements

Device measurements were performed in a four-terminal geometry, as shown in fig. 4.35(a). This measurement, sometimes called the "Kelvin" measurement, aims to remove the parasitic resistances of the leads and contacts in the system. Figure 4.35(b) shows a schematic of the 4-terminal measurement including resistances. If the lead resistances are very small compared to that of the device, i.e.

$$R_{1,2,3,4} < 0.01 \cdot R_D \tag{4.13}$$

where R_{1-4} are the lead resistances and R_D is that of the device, then the only resistance measured is that of the device. Since the pillar resistances were typically in the range 10 Ω to 100 Ω, this assumption was valid.

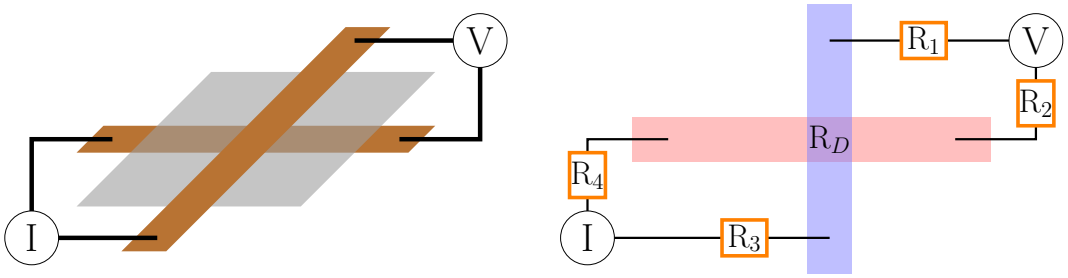

(a) 4-terminal device measurement geometry.

(b) 4-terminal schematic showing resistances.

Figure 4.35: The 4-terminal device geometry to remove parasitic resistance.

4.5.2 DC vs. Pulsed Electrical Measurements

Electrical measurements can be conducted in two ways. The first method is a DC measurement. A direct current is supplied and the voltage drop across the device is repeatedly measured to determine the device resistance. However due to the constant application of a current, there is Joule heating in the device. This causes an error due to the temperature dependence of metallic resistance but also threatens the device itself. The heating can cause annealing effects in the crystal, fundamentally changing the properties of the device. Alternatively there can be enhanced diffusion effects which can either enhance or negate the GMR effect. This is especially true if melting temperatures are reached, most significantly at the edges of the sample. If the two FM layers become connected around the pillar edge no GMR can be observed.

The alternative approach in order to avoid the heating effects is a pulsed measurement. Here an alternating positive and negative current pulse is applied for a short burst. The average of the positive and modulus of the negative voltage drop across the device are taken. This is then repeated a number of times denoted delta (Δ) to reduce the statistical error and such this technique is often called a Delta Pulsed Measurement.

The pillar devices were resistant to Joule heating and as such currents >100 μA could be used. This in combination with a Keithley nanovoltmeter allowed for a signal-to-noise ratio (SNR) of <0.01%. This was vital given that GMR values of <0.02% were recorded. An example of a typical measurement is shown in fig. 4.36 measured with a current of 500 μA for $\Delta = 20$.

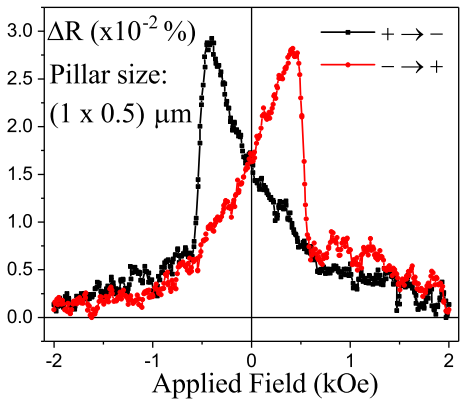

Figure 4.36: An example of a Δ measurement of a 1000 nm × 500 nm elliptical GMR pillar.

4.6 Note on Errors

In this thesis errors have been calculated statistically using standard Gaussian techniques when possible. In other instances the error in limited by the resolution of equipment.

For magnetic measurements the precision of the field values are better than 1 Oe and as such the error in coercivity is small. The same is true for the determination of loop squareness, since the sensitivities of the VSM and AGFM and 10^{-6} emu and 10^{-8} emu respectively. However, there are significant errors when calculating the value of M_S. While the precision in moment is very high there are errors within the films themselves that prevent an accurate determination of film volume. Firstly the thickness as a whole is only known to approximately $\pm 5\%$. Furthermore this thickness is not consistent across the whole film because shadowing occurs at the edges of the sample during deposition. Therefore in this work the error in M_S is estimated to be $\pm 10\%$. However since these uncertainties are consistent samples can be compared to one another with some degree of confidence.

When determining the lattice constants and strain in a material from XRD data the accuracy is very high due to precise alignment procedures, positions of known peaks to calibrate against and a resolution of 0.001°. The only significant error comes from Scherrer analysis to determine crystallite sizes. While the statistical error is highly reproducible and taken as $\pm 2\%$, this does not reflect the true error on the grain size. This is because of limitations of the Scherrer approach, meaning that the true error could be upwards of $\pm 20\%$. However, for comparison between samples and the identification of trends, Scherrer analysis is more than sufficient.

5 Heusler Alloys with Vanadium Seed Layers

Heusler alloys have a pseudo-fcc structure as discussed in section 3.1. Therefore most early attempts to improve their crystallinity and manipulate the crystal structure of Heusler alloys was done using fcc seed layers. This met with some success, significantly with the silver seed layers and Co_2FeSi discussed in detail in section 3.1 [105]. However, while a significant reduction in the crystallisation energy of 50% was achieved [104] along with a 2D texture, there were no instances where perpendicular magnetic anisotropy was induced. In this work vanadium seed layers were used in an attempt to induce a strong texture and a perpendicular anisotropy.

Vanadium (V) is a bcc, metallic element with a significant lattice mismatch to Heusler alloys and a lattice parameter 47% smaller than that of Co_2FeSi for example. This lattice mismatch is reduced to 24% if the growth of the Heusler alloy is at 45° to the vanadium seed layer. This should induce a large strain in a Heusler alloy lattice, leading to a change in the anisotropy. Additionally vanadium seed layers have been shown to promote a strong {110} texture in Heusler alloys [157–159] and as such should be ideal for this work. The thicknesses of the vanadium seed layers used were 5 nm or 42 nm and 50 nm [159, 160] however no reason for this is given. Thus a full optimisation of the use of this seed layer was carried out.

5.1 Crystallisation of Vanadium Seed Layers

Initial experiments were performed to investigate the crystallisation of vanadium seed layers with thicknesses from 5 nm to 30 nm in steps of 5 nm. Additionally the effects of a 3 nm thick chromium smoothing layer beneath the vanadium seed layer were investigated after the success found with silver seed layers [105]. The chromium layer was found to prevent islanded growth of the silver, reducing the pinning at the interface and the results are shown in section 3.3.2. A thickness range must be investigated for two reasons; firstly many materials only crystallise when the layer thickness exceeds several unit cells and secondly the material may be strained at the interface with the substrate or capping layer. Increasing the layer thickness allows the material to relax towards its bulk lattice parameters. The thickness range of 5 nm to 30 nm is equivalent to a range of 16 to 99 unit cells of vanadium. A summary of the samples grown is shown in table 5.1.

Smoothing Layer	Seed Layer	Capping Layer
-	V (5, 10,..., 30 nm)	Al (3 nm)
Cr (3 nm)	V (5, 10, ..., 30 nm)	Al (3 nm)

Table 5.1: Summary table of samples grown for optimisation of vanadium seed layers.

The thickness of the films is monitored using a quartz crystal growth rate monitor. From previous experiments where XRR fitting has been used to determine layer thickness the error is found to be approximately 5%.

From the $\theta/2\theta$ scans shown in fig. 5.1(a) it was found that there is a relaxation in the value of the lattice parameter for the vanadium layer with increasing thickness shown by an increase in the Bragg angle θ_V. The calculated inter-planar separation for the vanadium {110} planes for each thickness is shown in fig. 5.1(c). From fig. 5.1(c) it is clear that an increase in the layer thickness causes a relaxation of the vanadium lattice towards the value in the bulk of $d_{\{110\}} = 0.214$ nm. Therefore the lattice parameter of a vanadium layer is controllable and can possibly be used to manipulate further layers in a stack.

Figure 5.1(b) also shows the effect of the addition of a 3 nm thick layer of chromium on the XRD spectrum. The strain on the lattice is almost entirely removed in layers of vanadium with thicknesses >5 nm as shown in fig. 5.1(c). This implies that there is a change in the growth with the presence of the chromium

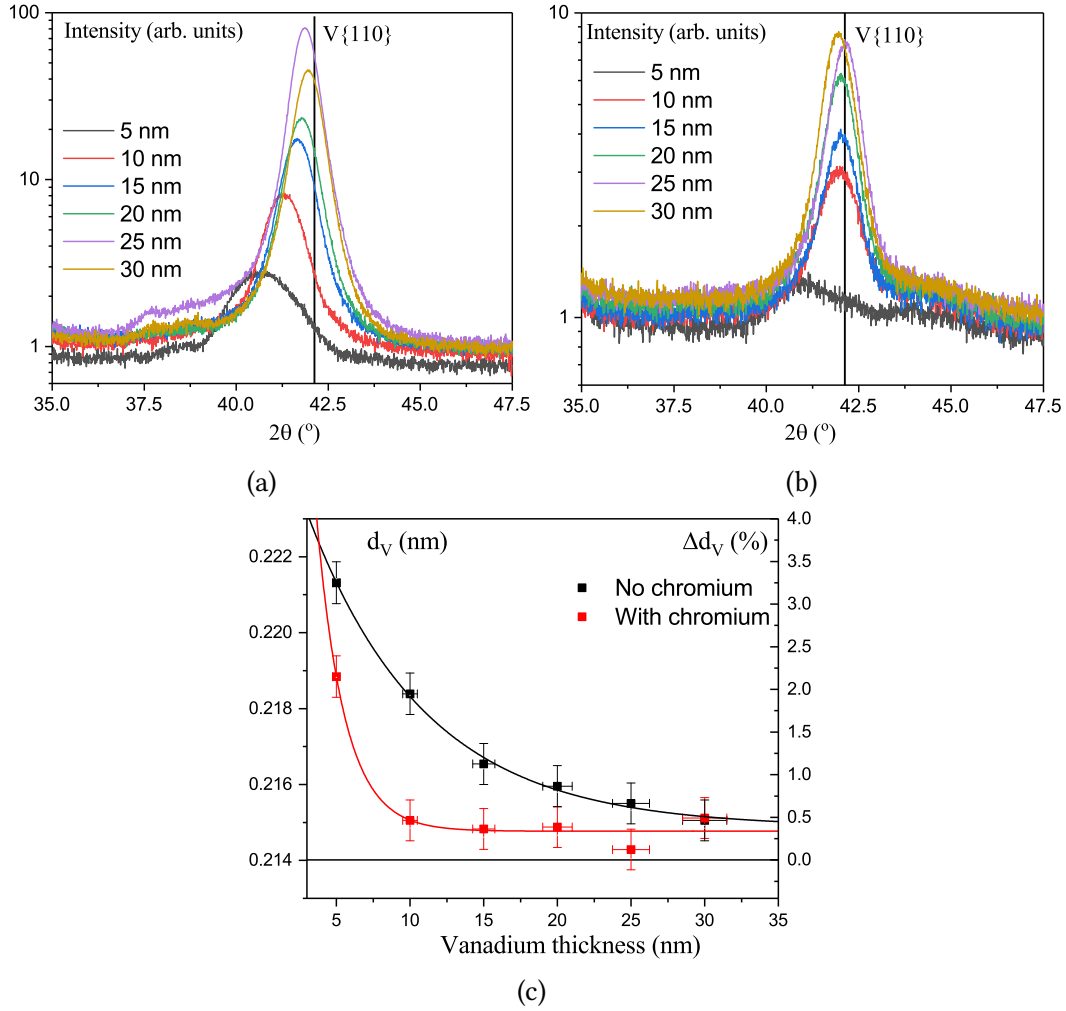

Figure 5.1: $\theta/2\theta$ spectra for vanadium seed layers of thickness 5 nm to 30 nm without (a) and with (b) a 3 nm smoothing layer of chromium. (c) The change in the spacing of vanadium {110} planes (d_V) for a vanadium seed layer with increasing thickness both without (red) and with (blue) a chromium layer.

layer possibly due to a low lattice mismatch of 4%. However the smoother layer with a small lattice mismatch actually prevents the development of texture in the vanadium layer. The chromium {110} reflection is only weakly observed in the sample with 5 nm of vanadium due to the low thickness of 3 nm. The low thickness causes a low intensity reflection, but may also cause a lack of crystallinity in the chromium layer. In samples with reflections of greater intensity of the vanadium {110} planes the chromium peak is hidden by the shoulder of the vanadium reflection. Additionally the vanadium that grows on this wetting layer has very low crystallinity, shown by a low relative intensity in the $\theta/2\theta$ scans which is reduced by approximately a factor of ten.

The texture of vanadium films grown without chromium smoothing layers is shown in fig. 5.2 as the FWHM of the rocking curve of the vanadium {110} peak. In

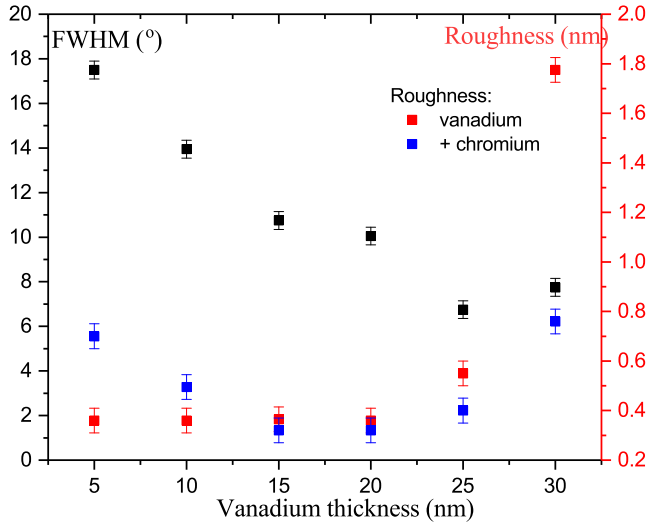

Figure 5.2: The change in rocking curve FWHM of the vanadium {110} reflection for a vanadium layer with increasing thickness without (red) a chromium layer and the roughness of vanadium layers with (orange) and without (purple) a chromium layer.

films with a chromium layer the FWHM was >20° for all thickesses of vanadium. The FWHM of the rocking curve is at a minimum for a layer thickness of 25 nm and as such this thickness is optimal for inducing further texture in a Heusler alloy layer. Figure 5.2 also shows the roughness of the vanadium layer with and without the chromium layer determined by XRR. At low thicknesses the presence of a chromium layer increases the roughness of the film which again shows the changing growth conditions that the vanadium layer experiences. The roughness of the films then increases with thickness with a large change in the roughness from 0.5 nm to 1.75 nm for thicknesses between 25 nm and 30 nm. There is a clear threshold thickness around 25 nm where the sample properties are optimised. This is possibly due to the creation of islands at greater thicknesses which in turn create the increased roughness.

This is the opposite of the case for silver seed layers where the film quality was improved by the presence of chromium. This is likely due to intermixing being more prevalent between chromium and vanadium than with silver. This is because vanadium is small in comparison to silver and very similar in size to chromium, both in terms of lattice parameter and atomic diameter. Furthermore chromium and vanadium are both bcc materials, whereas silver has an fcc structure.

5.1.1 Effects of Annealing of Vanadium Seed Layers

A parallel investigation into the effect of annealing a vanadium seed layer under a Heusler alloy was undertaken. Two samples were grown, one with and one without a chromium smoothing layer. The effects of annealing the samples at 300 °C for 1–3 hours were investigated. The samples structures are shown in table 5.2.

Smoothing Layer	Seed Layer	Magnetic Layer	Capping Layer
-	V (15 nm)	Co_2FeSi (10 nm)	Al (3 nm)
Cr (3 nm)	V (15 nm)	Co_2FeSi (10 nm)	Al (3 nm)

Table 5.2: Summary table of samples grown for annealing of a vanadium layer with a layer of Co_2FeSi.

Figure 5.3 shows the change in the level of strain in the {110} planes of the vanadium and Co_2FeSi lattices calculated from $\theta/2\theta$ scans of the sample without the chromium layer. It is clear from the opposite trends in the lattice strains of vanadium and Co_2FeSi that the annealing process is providing energy to improve the match between the two lattices. As the vanadium lattice is stretched wider with an increasing lattice strain an opposite change is observed in the Co_2FeSi layer.

Pole figure scans provide a more in depth analysis of the texturing of the films for each individual layer. The pole figure scans are performed around the {110} reflection of the vanadium and {220} reflection of the Co_2FeSi layers respectively.

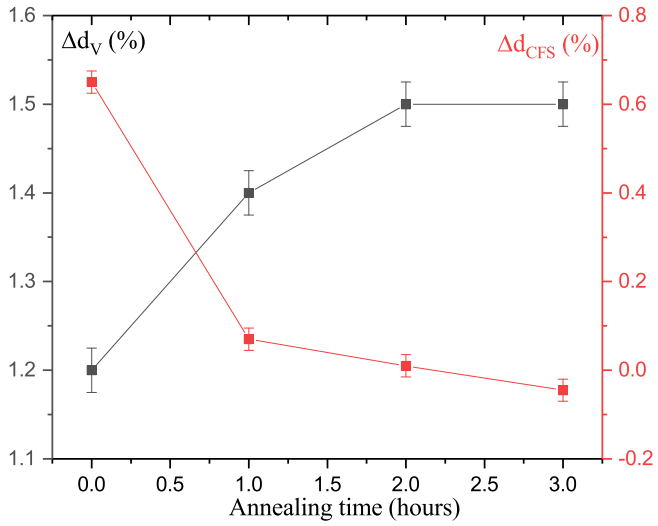

Figure 5.3: The change in the strain in vanadium and Co_2FeSi {110} planes for a samples with increasing annealing time at 300 °C.

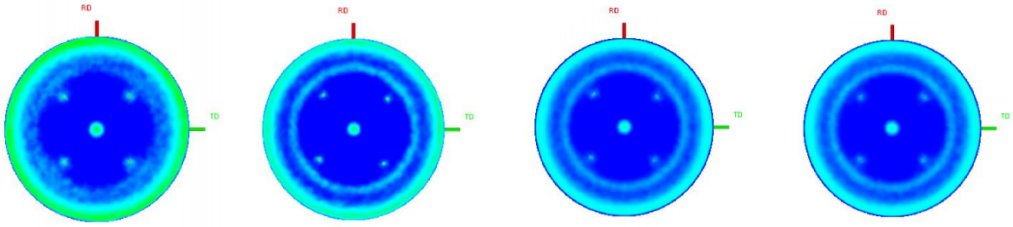

(a) Co_2FeSi as deposited. (b) Co_2FeSi, 1 hour. (c) Co_2FeSi, 2 hours. (d) Co_2FeSi, 3 hours.

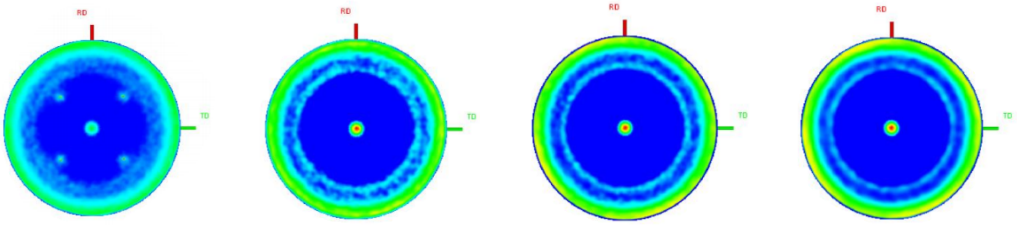

(e) V as deposited. (f) V, 1 hour. (g) V, 2 hours. (h) V, 3 hours.

Figure 5.4: Pole figures of the Co_2FeSi {220} peak (a) as-deposited (a) and after annealing for (b) 1, (c) 2 and (d) 3 hours which show sharpening of the ring at 29° and the same for the vanadium {110} peak (e, f, g & h).

In the data for the as-deposited films shown in fig. 5.4(a) and fig. 5.4(e) there is a diffuse ring at $\alpha = 29^o$. The position of the rings confirms a dominant {110} orientation in the films but the lack of intensity and sharpness are indicative of a low level of texture. The spots are caused by the single crystal Si substrate.

After annealing the sample for 1 hour at 300 °C there is a large improvement in the sharpening of the ring in both the vanadium and Co_2FeSi reflections, as well as an increase in their relative intensities. This is due to an increasing crystallisation in the layers with annealing time and the possible narrowing of the range of lattice parameters in the layer. As the layers crystallise, more of the film relaxes to a consistent lattice parameter, whereas the as-deposited film has a range of strained and non-strained grains.

5.2 Effects of Thickness of Vanadium Seed Layers on Co_2FeSi

Vanadium layers were grown at thicknesses of 15 nm, 25 nm and 30 nm, with and without 3 nm smoothing layer of chromium, upon which 20 nm of Co_2FeSi was deposited. $\theta/2\theta$ scans indicate a clear, strong dependence of the crystal struc-

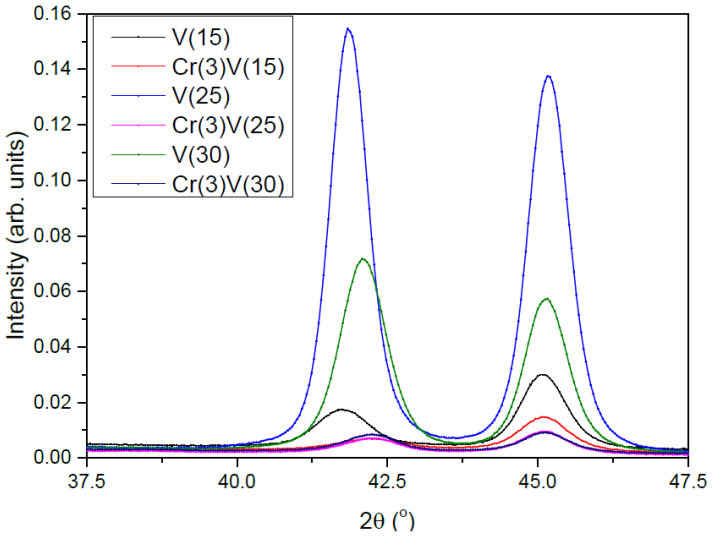

Figure 5.5: $\theta/2\theta$ scans of 20 nm of Co_2FeSi with various thickness of vanadium as a seed layer, with and without a chromium layer.

ture upon the thickness of the vanadium seed layer, as shown in fig. 5.5. As expected there is a very low intensity of the vanadium {110} reflection when a chromium layer is present. This lack of crystallisation continues into the Co_2FeSi layer, the crystallinity of which is highly dependent upon that of the seed layer. The {110} reflections of the untextured vanadium films with chromium seed layers are also not shifted in 2θ and are deposited in a bulk like state, indicating there is no strain from either the substrate or the Co_2FeSi interface.

For the samples without chromium smoothing layers there is a relaxation of the vanadium {110} reflections towards the bulk position with increasing film thickness, indicating the presence of strain at an interface. There is a significant increase in the intensity of the reflection with a 25 nm seed layer showing a large improvement in the crystallinity in both the seed layer and the Co_2FeSi. This is as expected from previous measurements with just vanadium. This thickness lies between the wide range of seed and buffer layer thicknesses used in previous works [157, 159, 160].

The relationship between the crystallisation of the seed layer and the Co_2FeSi is confirmed by rocking curve analysis. The FWHM of the rocking curve of the Co_2FeSi {220} reflection exactly matches that of the seed layer peak implying that the texture in the film is determined purely by the seed layer. This is further confirmed as there is no texture present in the Co_2FeSi when a chromium layer is introduced under the seed layer. Hence texture cannot be introduced without a well crystallised seed layer. Pole figure scans of the Co_2FeSi peak confirm the

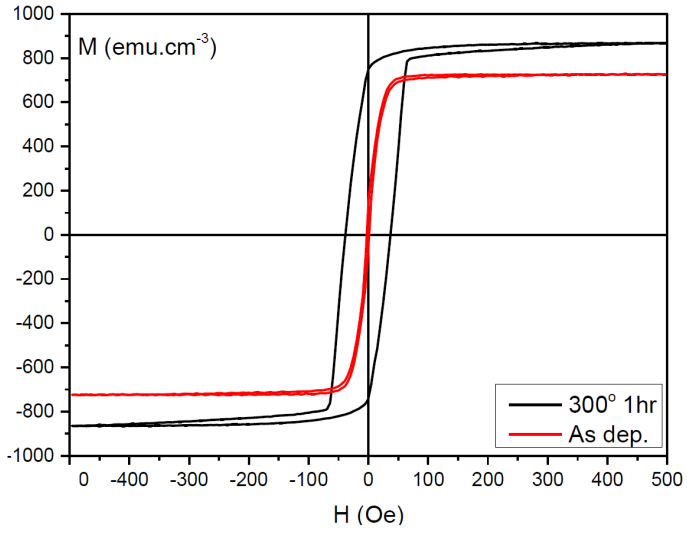

Figure 5.6: *M-H* loops in-plane for a 20 nm Co_2FeSi layer with a 25 nm seed layer of vanadium before and after annealing at 300 °C.

structural differences, with no evidence of a textured film present in the samples with a chromium layer.

Figure 5.6 shows the in-plane hysteresis loop for the sample with a 25 nm seed layer. The anisotropy is strongly in the plane of the sample as indicated by a saturating field of over 10 kOe in the out-of-plane direction. This is due to the large demagnetising field of $H_d \approx 9$ kOe at saturation present in the sample, caused by the high value of M_S of (720 ± 70) emu/cm^3. The material is extremely soft in-plane, with a coercivity of <5 Oe and a loop squareness of $S = 0.2$, where $S = \frac{M_r}{M_S}$. The crystallisation of the sample gives a magnetisation of 720 emu/cm^3 which is 65% of the bulk value of 1100 emu/cm^3 [17]. This reduced magnetisation is found in other work where vanadium seed layers are used [159, 160].

A change in the loop squareness is observed with increasing thickness, whereby the 25 nm sample had a loop squareness of $S = 0.2$ but this increased to $S = 0.7$ with a 30 nm seed layer. This follows the same trend as the rocking curve analysis, indicating that a poorer layer texture increases the loop squareness. This is confirmed by the samples with a chromium layer, and therefore no texture, having a loop squareness > 0.7 for all thicknesses of the vanadium seed layer. There is also a small increase in the coercivity to 20 Oe in the films where a chromium layer is present. These phenomena are caused by a decrease in the interfacial quality and crystallisation in the samples. Firstly, both of these lead to an increased strength or number of pinning sites in the sample, increasing the loop squareness and H_C. Secondly the grain size of the films increases with the improved texture which

reduces the number of pinning sites at grain boundaries.

An investigation was then carried out into the effect of annealing samples at 300 °C for one hour. 300 °C was used as this is approaching the limit for industrial standards to protect temperature sensitive components. Figure 5.6 shows the in-plane hysteresis loop for a 20 nm thick layer of Co_2FeSi with a 25 nm seed layer before and after annealing. The values of M_S, H_C and S all increased significantly after annealing, to (860 ± 90) emu/cm^3, 40 Oe and 0.7 respectively. This is still lower than the bulk value for magnetisation however, so complete crystallisation has not occurred.

The increase in M_S is due to an improved crystallinity in the Co_2FeSi, but does not reach the bulk value. While this is due in part to incomplete crystallisation of the Co_2FeSi layer; it could also be caused by intermixing and interfacial compounds. Vanadium is a small and mobile atom and therefore moves easily between layers in the sample. Heusler alloys are also possible which include vanadium, such as Co_2VSi. Either or both of these circumstances will lead to a decrease in M_S.

5.3 Variation of Co_2FeSi Layer Thickness

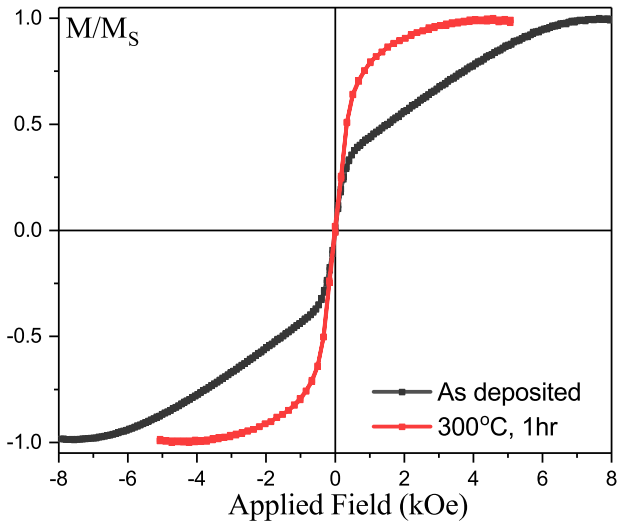

Figure 5.7: Out-of-plane *M-H* loops for a 5 nm Co_2FeSi layer with a 25 nm seed layer of vanadium before (black) and after (red) annealing at 300 °C for one hour.

As is typical for fcc Heusler alloys, the films were found to have no out-of-plane anisotropy. However, it clear that strain was occurring at the interfaces and

therefore anisotropy may be induced in thinner layers where strain should be more significant. Previous work on ferromagnetic resonance FMR studies has shown spin effects at the vanadium-Heusler alloy interface [160] which can rearrange the electronic structure. Since the effects will both be interfacial, thinner films will be more heavily influenced. Samples with Co_2FeSi layers with thickness 5 nm to 17.5 nm were grown on the optimised 25 nm vanadium seed layer to demonstrate this effect.

Figure 5.7 shows the out-of-plane *M-H* loops for the 5 nm thick layer of Co_2FeSi. There is a clear increase in the level of perpendicular anisotropy in the film. Firstly the saturating field is lower with a value of 8 kOe. This is in part due to a smaller demagnetising field caused by the decrease in M_S due to the increased influence of magnetically dead layers at the interface. These can be estimated to be up to 1 nm thick from the reduction in M_S, however it is difficult to estimate how much magnetisation loss is due to a lack of crystallisation compared to dead interface layers. In spite of this it is possible that some interfacial strain is also increasing the anisotropy. This is reinforced by the shape of the hysteresis curve in the low field region. The steep gradient shows a large susceptibility $\chi_\perp$ indicating that perpendicular anisotropy is present. There is then a decrease in gradient as the increasing magnetisation, and therefore H_d, reduces $\chi_\perp$.

Annealing the sample at 300 °C further increases the perpendicular anisotropy. This is shown in fig. 5.7 by a significant increase in the effects discussed above. Firstly the saturating field is approximately halved to 4 kOe in spite of the increased H_d caused by the crystallisation from annealing. Furthermore the value of $\chi_\perp$ is greater followed by a simple domain rotation or domain wall motion process driven curve to saturation.

Further thinning of the Co_2FeSi layer to 4 nm had a significant effect on the anisotropy as shown in fig. 5.8 where there is a large increase in the perpendicular anisotropy. There is a non-zero coercivity in-plane due to the weak domain wall pining in the sample, with a strength of only 2 Oe. Once again the magnetisation reversal showed a large rotational component out-of-plane accounting for approximately 40% of the reversal. This is caused by greater pinning strength of 15 Oe in the out-of-plane direction preventing a nucleated reversal of the film as a whole occurring. A nucleated reversal would be expected in films with strong intergranular exchange coupling. This can be determined using an activation volume, i.e. the volume of the film that acts as a single magnetic entity. In a film with strong coupling this will be far larger than the grain size. Measurements on sim-

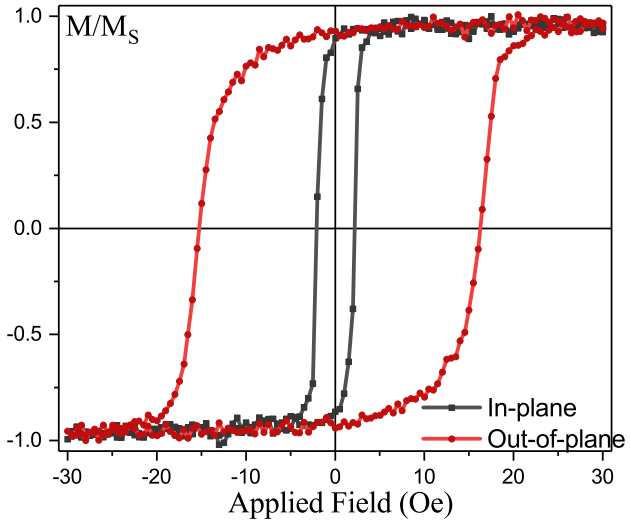

Figure 5.8: In- and out-of-plane *M-H* loops for a 4 nm Co_2FeSi layer with a 25 nm seed layer of vanadium.

ilar films with tungsten seed layers showed that the intergranular coupling leads to activation volumes roughly double the grain size and is discussed in section 6.3.

It is therefore likely that a similar activation volume and therefore strong coupling will be observed in films with vanadium layers. Consequently both the pinning and anisotropy must be strong as they are overcoming the intergranular exchange and preventing nucleation from occurring.

This thickness of these films is comparable or greater than observed in similar systems with perpendicular anisotropy provided by an MgO interface, where the thickness of Heusler alloy layer is often limited to 1 nm [28, 161] but can be up to a maximum of 3.5 nm [162]. In order to achieve this anisotropy a heavy metal interface had to be included at the capping layer, whereby spin-orbit coupling enhances the anisotropy caused by the MgO. Therefore it should be possible to increase the anisotropy in films with vanadium seed layers by varying the capping layer to enhance this coupling.

5.3.1 Effects of a Second Interface

Since the increase in the anisotropy of the Co_2FeSi layer is caused by the interface with vanadium, it is possible that the addition of a second interface on top of the Heusler alloy layer should improve this. This is shown in fig. 5.9 for a 5 nm Co_2FeSi film with a 25 nm seed layer of vanadium which has a second vanadium

layer 1.5 nm on top. The addition of the second vanadium-Heusler alloy interface causes a reduction in the saturating field to <300 Oe as well as an opening of the loop.

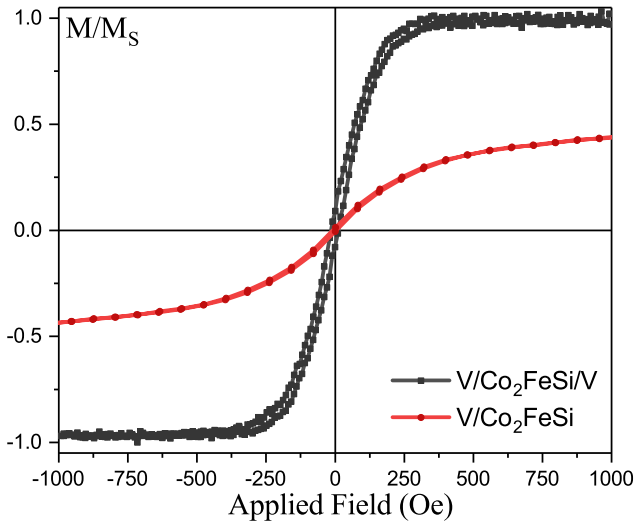

Figure 5.9: Out-of-plane *M-H* loops for a 5 nm Co_2FeSi layer with and without a 1.5 nm layer of vanadium at the top interface.

This is possibly caused by a further increase in the anisotropy induced by interfacial strain. However it is also likely that the pinning is increased in the film if any intermixing of vanadium is occurring at interfaces. Furthermore a 1.5 nm thick layer is likely only nano-crystalline or amorphous, limiting the crystallographic influence. However the changes observed in fig. 5.9 provide further evidence that the origin of the anisotropy in the Co_2FeSi layer is at least significantly interfacial in origin.

5.4 V/Co_2FeSi Multilayers

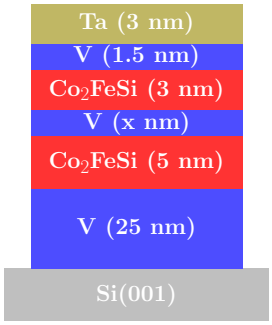

Figure 5.10: Schematic of vanadium based GMR stacks.

Samples in a typical GMR format were deposited in silicon substrates with the structure V (25 nm)/Co_2FeSi (5 nm)/V (x nm)/Co_2FeSi (3 nm)/V (1.5 nm)/Ta (3 nm); where x was varied from 0.5 nm to 2.5 nm in steps of 0.5 nm, shown schematically in fig. 5.10. By using vanadium as a spacer layer it should be possible to maintain the

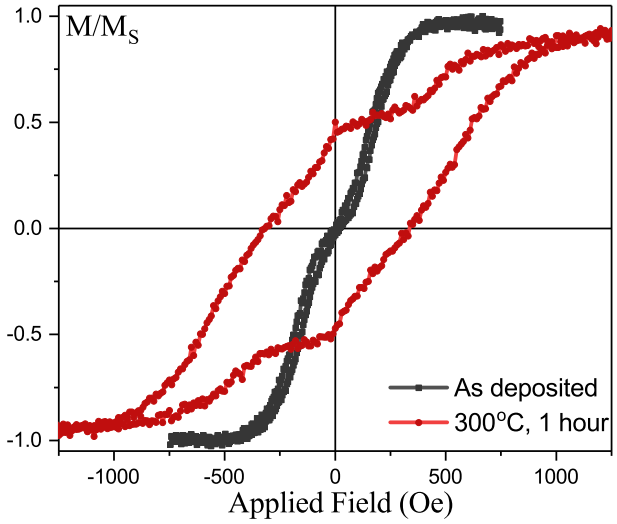

Figure 5.11: Out-of-plane *M-H* loops for a V/Co_2FeSi GMR multilayer before and after annealing at 300 °C for one hour.

interfacial anisotropy throughout the GMR stack. However the spacer layer used in a GMR device is often optimised by matching the energy levels of the conducting valence bands in the ferro- and non-magnetic layers in order to maintain spin-polarisation at the interfaces. In Heusler alloys this is most often achieved using silver spacer layers. Therefore it is possible that maintaining the anisotropy may limit the GMR observed in devices with this structure due to poor energy level matching.

Figure 5.11 shows the out-of-plane *M-H* loop for the sample with a 1.5 nm layer of vanadium. There is some evidence of layer thickness dependent switching in the low field region indicated by the change in $\chi_\perp$, where $\chi_\perp$ is the gradient of the *M-H* loop in the low field region of −250 Oe to 250 Oe. The 1.5 nm sample shown in fig. 5.11 exhibited the largest change in $\chi_\perp$ of any value of x, with a change in gradient of 82%. However while a clear change can be observed a true antiparallel state is never reached due to the lack of remanent magnetisation in either layer. As such while it maybe possible to observe a GMR in a stack with this structure, the magnitude would be very low and a broad peak observed.

There is a significant change in the hysteresis loop after annealing at 300 °C, as shown in fig. 5.11. There is a bimodal switching field distribution; firstly the magnetisation reduces by approximately 40% through a rotation of the 3 nm layer, which has little or no remanence or coercivity. There is then a stable antiparallel region before a rapid switch in the 5 nm layer. This should allow for easy observation of GMR in a device with this structure, as the antiparallel state is wide and

stable.

The increased coercivity and remanence has several possible origins. Firstly crystallisation of the Heusler alloy and vanadium layers may enhance the interfacial anisotropy by providing energy for lattice matching to occur, as observed in fig. 5.3. Secondly intermixing at interfaces and grain boundaries may lead to greater pinning site numbers and strength which therefore leads an increased coercivity.

5.4.1 Silver and Copper Spacer Layers

Samples were also deposited with the structure discussed in section 5.4 and shown in fig. 5.10 but with the vanadium spacer layer replaced by one of silver or copper. The thicknesses of these layers were set at Ag (1 nm and 2 nm) to keep device thickness low and Cu (0.9 nm and 1.8 nm) as these are the respective antiferromagnetic coupling peak thicknesses [75]. It must be noted that these figures are for cobalt ferromagnetic layers. However iron layers show similar results and thus it must be assumed that Co_2FeSi will be close to this value. Silver, and to a lesser extent copper, have a good energy level match at the Fermi surface with a large number of cobalt-based Heusler alloys and are therefore a popular choice for spacer layers in Heusler alloy devices [21, 163, 164].

For the copper spacer layers no layer thickness dependent switching was ob-

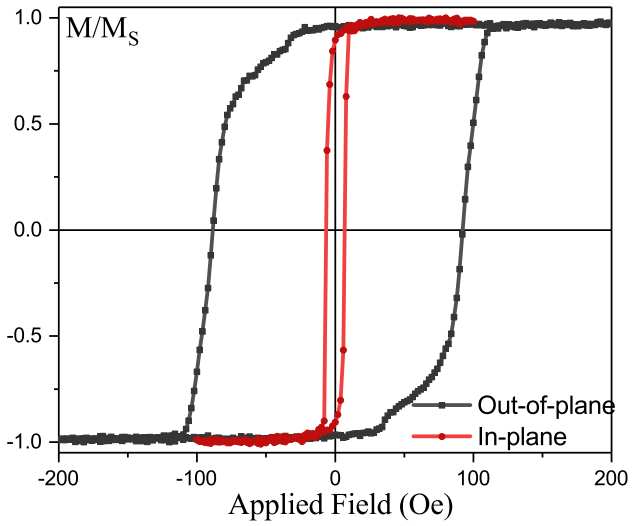

Figure 5.12: In- and out-of-plane *M-H* loops for a V/Co_2FeSi GMR multilayer with a 2 nm spacer layer of silver.

served, nor was this observed in the sample with a 1 nm silver spacer layer. This could be caused by the roughness of the films, at 0.5 nm, being on the same scale as the film thicknesses. This prevents the layers acting independently if the roughness prevents their separation. Secondly the sputtered layers may not crystallise at these low thicknesses. In the previous work cited above the thickness of the silver layer is often taken as 5 nm and is additionally annealed at temperatures up to 500 °C. This will improve the crystallisation of the spacer layer but is not compatible with industrial processes and would result in diffusion of the vanadium seed layer. Furthermore the the alloying and diffusion caused by the high annealing temperature can create a significantly increased resistance [164].

In the sample with a 2 nm silver spacer layer there is a significant change in the *M-H* loop compared to the as-deposited sample using a vanadium spacer layer. Firstly, the squareness of the loop increases to 1 for both layers of Co_2FeSi and an increase in the coercivity to 100 Oe is observed. This is probably due to an increase in the pinning site number and strength at the silver-Heusler alloy interfaces. This could be caused by an increase in the roughness when using a silver spacer, possibly caused by islanded growth of the silver on the Co_2FeSi. Alternatively alloying or diffusion of the silver may occur more readily than with vanadium in as-deposited films. There is a small nucleation event at 40 Oe, most likely created at a corner or edge domain. The lack of propagation and subsequent rotation and domain wall motion confirm the presence of strong pinning in the sample.

Perpendicular anisotropy was been induced in the Heusler alloy Co_2FeSi by using a 25 nm vanadium seed layer. In order to improve on this, however, a heavy metal with strong spin-orbit coupling is required to exploit the anisotropy that is induced at interfaces with ferromagnets. Therefore tungsten seed layers were used as this is an element cryptographically similar to vanadium, but with significantly stronger spin-orbit coupling.

6 Heusler Alloys with Tungsten Seed Layers

Tungsten, like vanadium, is a transition-metal element which crystallises in a bcc structure. The lattice parameter is larger than that of vanadium, with values of $a_W = 0.31648$ nm and $a_V = 0.3030$ nm respectively. This leads to a similar, large lattice mismatch to Heusler alloys; 41% to Co_2FeSi for example, which is reduced to 21% by a 45° rotation in the growth direction. The bulk resistivity is much lower in tungsten with a value of $5.6 \times 10^{-6}\,\Omega/\text{cm}$ [165], approximately half the resistivity of vanadium which is $1.9 \times 10^{-5}\,\Omega/\text{cm}$ [166]. For a low resistance GMR junction this is ideal.

6.1 High Temperature Growth of Tungsten

In order to encourage the crystallisation of a tungsten layer, the substrate was pre-heated to 400 °C prior to deposition. An initial sample with the simple structure W (20 nm) was deposited to investigate the growth of a seed layer without a magnetic layer or a top interface.

Figure 6.1 shows the in- and out-of-plane XRD data for the 20 nm layer of

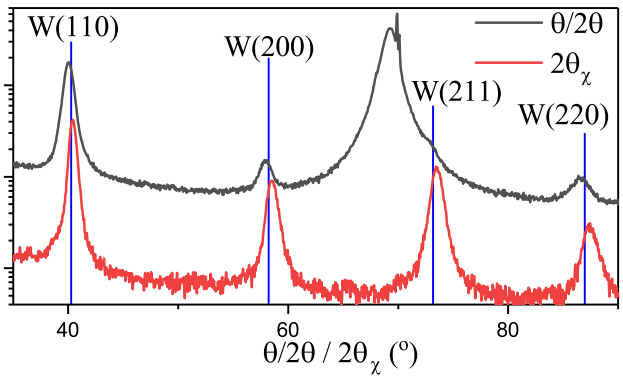

Figure 6.1: $\theta - 2\theta$ and $2\theta_\chi$ scans of a 20 nm W film grown at 400 °C.

tungsten which show reflections from the {100}, {110} and {211} planes. This implies that there is no single 2D texture but the tungsten layer is well crystallised.

The relative intensity of the {110} reflection is 10–11 times greater than that of the {200} and {211} reflections out-of-plane and hence there may be a weak texture. By comparing to XRD database files this is confirmed as in powder tungsten samples the {110} reflection is far less relatively intense. This is reinforced by the comparative relative intensities of the reflections in-plane. The {110} reflection is only five times greater than the {100} and {211} reflections in-plane, implying that the texture is more random in 2D than 3D. Scherrer analysis of the {110} peak gives a crystallite size of the order of 8 nm.

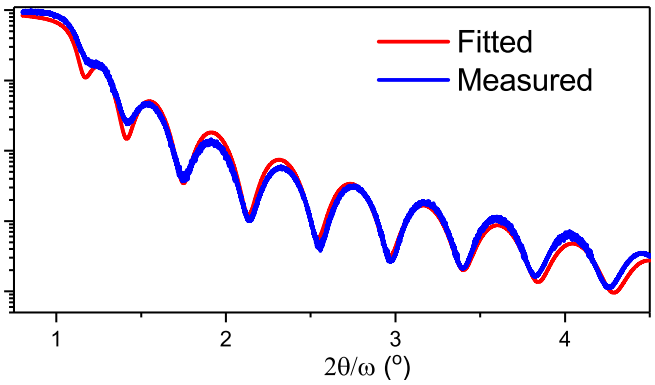

Figure 6.2: XRR scan of a 20 nm W film grown at 400 °C.

Figure 6.2 shows the fitted XRR scan for the sample. The data shows that the tungsten film more than 90% dense with a surface roughness of just 0.2 nm. The tungsten layer is therefore being deposited in a bulk like state with low surface roughness, which is ideal for a seed layer. However the lack of texture will not help to encourage a strong out-of-plane texture in subsequent layers. The lack of precision in XRR fitting comes from the nature of being of being a four parameter problem. There is therefore an issue with uniqueness of solution, especially since the fit shown in fig. 6.2 is not perfect.

6.2 Co_2FeSi Films with Tungsten Seed Layers

Layers of Co_2FeSi were added to a 10 nm tungsten seed layer in thicknesses from 2.5 nm to 12.5 nm in steps of 2.5 nm. Once more the substrate was preheated to 400 °C prior to deposition. Figure 6.3 shows the in-plane XRD data for a 2.5 nm layer of Co_2FeSi. Even at this low thickness there is evidence of crystalline Co_2FeSi

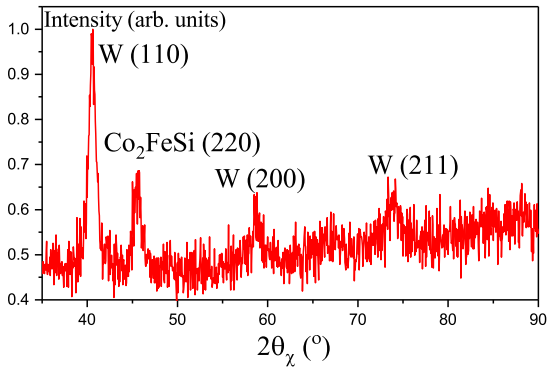

Figure 6.3: $2\theta_\chi$ scan of a 2.5 nm Co_2FeSi film grown on a 10 nm tungsten seed layer at 400 °C.

with a {110} orientation in-plane. As in the previous case without a Co_2FeSi layer, there are still three reflections from the tungsten layer with relative intensities of the {100} and {211} planes around 70% of that of the {110}.

The in-plane spacing of the Co_2FeSi{220} planes was reduced from the bulk value by 2% to 0.398 nm. This shows that a strain has been induced at the interface between the tungsten and Co_2FeSi layers, resulting in a slight tetragonal distortion out-of-plane. Scherrer analysis of the Co_2FeSi{110} reflections gave crystallite sizes that increased from (7.8 ± 0.2) nm to (9.7 ± 0.2) nm from the 2.5 nm to 12.5 nm thick layers of Co_2FeSi. This closely matches the crystallite size of the seed layer, implying that the tungsten seed layer is controlling the growth of the Co_2FeSi.

6.2.1 Magnetic Characterisation of W/Co_2FeSi Layers

The out-of-plane *M-H* loops for the films with increasing thickness are shown in fig. 6.4. All of the films exhibit a perpendicular anisotropy regardless of the thickness of the Co_2FeSi layer, t_{CFS}. None of the loops exhibited hard-axis behaviour. The films reverse through a domain nucleation and wall pinning mechanism, which is expected of a film with intergranular exchange coupling. However, the nucleation only occurs after significant rotation reduces the magnetisation to $0.5M_S$. It is only after this that the reversal becomes a domain wall motion process controlled by pinning. It is not possible to determine the exact field value where the reversal process changes accurately; however fig. 6.4 shows that the rotation increases with t_{CFS}.

There are two possible causes for the increased level of rotation with t_{CFS}.

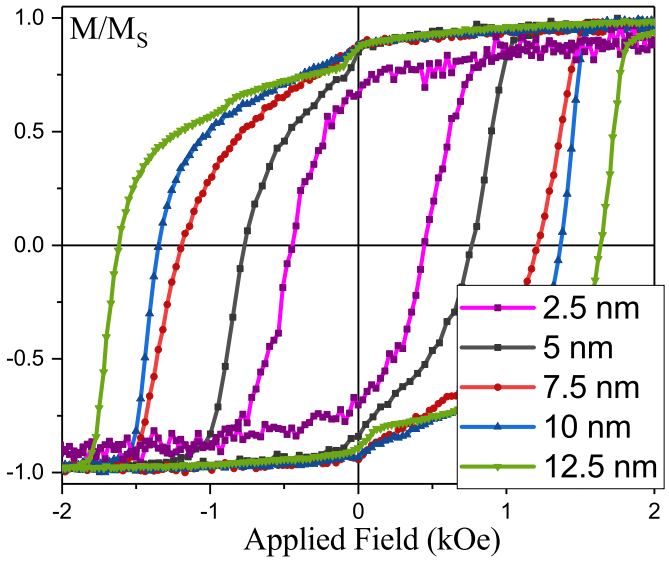

Figure 6.4: Out-of-plane *M-H* loops of 2.5 nm to 12.5 nm Co_2FeSi films grown on a 10 nm seed layer at 400 °C.

Firstly an increase in the anisotropy would lead to more magnetisation rotation, since the anisotropy energy would be greater and therefore overcome some of the intergranular coupling energy which favours a nucleation process. This would suggest that either the value of the anisotropy or the number or strength of pinning sites increases with the value of t_{CFS}.

Secondly both the coercivity and the grain size increase with t_{CFS}, with an increase in coercivity from 500 Oe to 1600 Oe with increasing t_{CFS} from 2.5 nm to 12.5 nm as shown in fig. 6.5(a). From the Stoner-Wohlfarth model discussed in section 2.1.1 the nucleation field H_n is found to be proportional to KV when thermal activation is taken into account. Therefore as the grain volume increases with t_{CFS} there is a corresponding increase in the value of H_n. This effect can be increased or decreased if the value of K changes. The change in grain volume for Co_2FeSi layers 2.5 nm to 12.5 nm thick is an approximate 7.7 times increase, if the grains are modelled as a cylinder. This would imply that the value of K decreases with t_{CFS} and therefore the increase in rotation is caused by an increase in pinning. The increase in the pinning is probably caused by an increase in roughness, which is generally observed with increasing film thickness in sputtered films.

A common method for determining the value of the anisotropy K is to use a coherent rotation model. However, the strong intergranular exchange coupling in these films makes this method invalid. This is because the coupling leads to a small but non-zero value for the coercivity in the plane of the sample. As such the value of the anisotropy field H_K cannot be determined from the hysteresis.

Further investigation of the anisotropy must be undertaken using a method such as ferromagnetic resonance to determine a numerical value of K.

Additionally fig. 6.5(a) shows the values of the saturation magnetisation M_S with increasing t_{CFS}. M_S increases from (480 ± 50) emu/cm^3 to (605 ± 60) emu/cm^3 with increasing t_{CFS} from 2.5 nm to 12.5 nm. This increase in magnetisation is potentially due to magnetically dead layers at one or both interfaces becoming less significant as the thickness increases. Additionally the 7.7 times increase in the grain volume with thickness lead to a greater volume of more bulk-like Co_2FeSi and as such bulk like magnetisation.

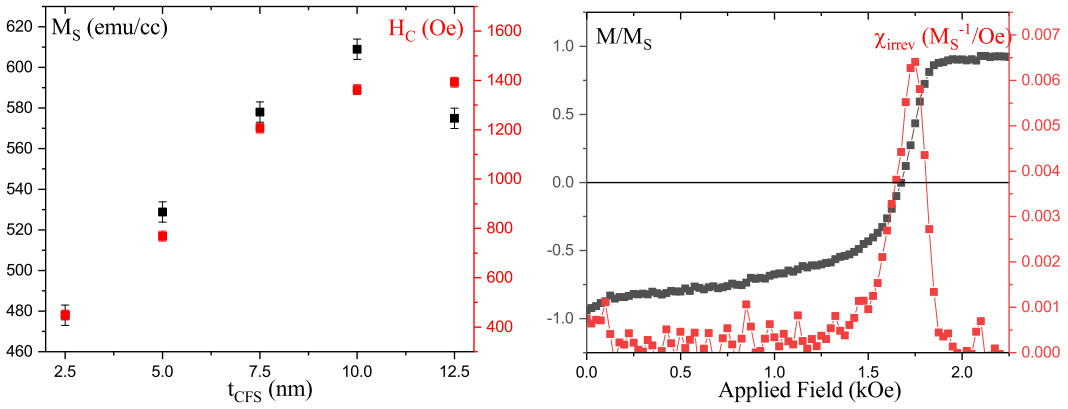

(a) (b)

Figure 6.5: (a) M_S and H_C for 2.5 nm to 12.5 nm Co_2FeSi films and (b) the DCD curve for a 12.5 nm Co_2FeSi films grown on a 10 nm seed layer at 400 °C and the calculated χ_{irrev}.

Figure 6.5(b) shows the out-of-plane DCD curve for the sample with a 12.5 nm layer of Co_2FeSi. As discussed in section 2.2 the intergranular coupling fields in polycrystalline films prevent the demagnetising field from being removed from a sample measurement. As such the DCD curve shown in fig. 6.5(b) is only accurate at the coercivity, where $H_d = 0$. Therefore only the remanent coercivity value of χ_{irrev} combined with a time dependence measurement of $S(H)$ at the same field gives an accurate value for the effective activation volume. An activation volume indicates how strongly the grains in a film are interacting. A large activation volume is caused by strong intergranular coupling which leads to nucleation process driven magnetisation reversal [?].

For the 12.5 nm thick film the diameter of the activation volume was found to be $D_{\mathrm{eff}} = (15 \pm 3)$ nm. This is almost double the crystallite size determined by Scherrer analysis which confirms that strong intergranular coupling is present in the film. However, this is far smaller than previously reported values for Co_2FeSi

activation volumes without a seed layer, which were consistently 50 nm [167].

6.2.2 W/Co_2FeSi/W/Co_2FeSi Multilayers

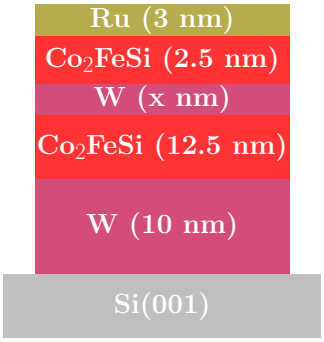

Figure 6.6: Schematic of tungsten based GMR stacks.

Since the coercivity of the Co_2FeSi layers is extremely sensitive to the thickness, a spin valve structure with layers switching individually can easily be constructed. This is ideal for a GMR device which does not necessarily require a layer to be pinned. Samples were deposited as shown in fig. 6.6 with the structure W (10 nm)/Co_2FeSi (12.5 nm)/W (x nm)/Co_2FeSi (2.5 nm)/Ru (3 nm), where x took values of 0.4 nm, 0.5 nm and 0.6 nm. These values are around the first antiferromagnetic coupling peak for tungsten at 0.55 nm [75]. This figure is again for cobalt ferromagnetic layers and must be assumed to be approximately correct for Co_2FeSi. The thickness of the Co_2FeSi were set to give the maximum possible differentiation in coercivity.

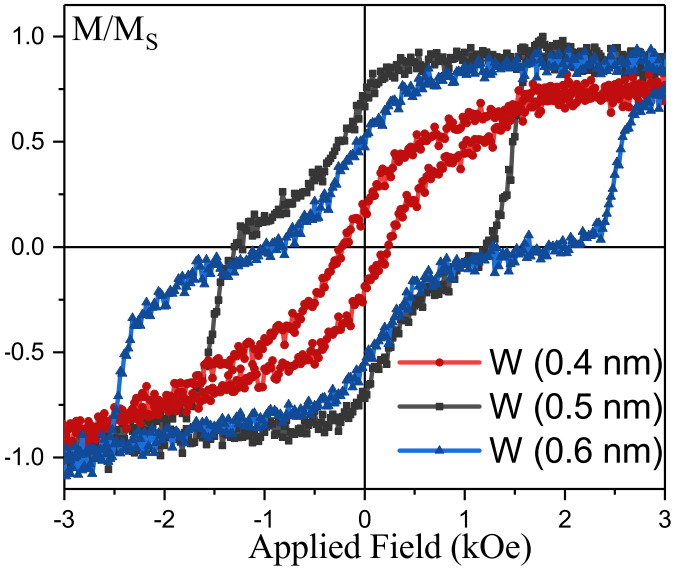

Figure 6.7: Out-of-plane *M-H* loops of W/Co_2FeSi/W/Co_2FeSi multilayer films grown with varying spacer layer thicknesses.

Figure 6.7 shows the *M-H* loops for the three samples. The samples with 0.5 nm and 0.6 nm spacer layers show distinct layer-thickness dependent switching, with two separate switching regions. Furthermore in these samples the coercivity is increased from the single-layer value. This could imply that some RKKY coupling is occurring through the W layer. However there is no direct evidence of strong

coupling between the two layers. The magnitudes of the two switching regions are not proprtional to the layer thicknesses meaning that there must be a very broad switching in the thicker Co_2FeSi layer, as observed in the *M-H* loop in fig. 6.4.

6.2.3 $Co_2FeAl_{0.5}Si_{0.5}$ Magnetic Layers

$Co_2FeAl_{0.5}Si_{0.5}$ is a Heusler alloy with properties similar to those of Co_2FeSi. However it also has a lower crystallisation energy, which should promote greater magnetisation in the film and greater texture. Figure 6.8 shows the *M-H* loops for multilayers where the Co_2FeSi in fig. 6.6 is replaced with $Co_2FeAl_{0.5}Si_{0.5}$. While the shape of the hysteresis loops are similar between the two Heusler alloys, the value of M_S is is approximately doubled in the films with the $Co_2FeAl_{0.5}Si_{0.5}$ layers due to greater crystallisation levels in the film as shown in table 6.1. This should in turn lead to a greater GMR in potential devices due to the direct proportionality between M_S and the MR ratio. The values of magnetisation are approximately half the values found in the single Co_2FeSi layers. This is caused by the high deposition temperature combined with multiple interfaces. This leads to significant alloying and intermixing at interfaces, leading to magnetically dead layers. This is also detrimental to any potential GMR since this in an interfacial effect.

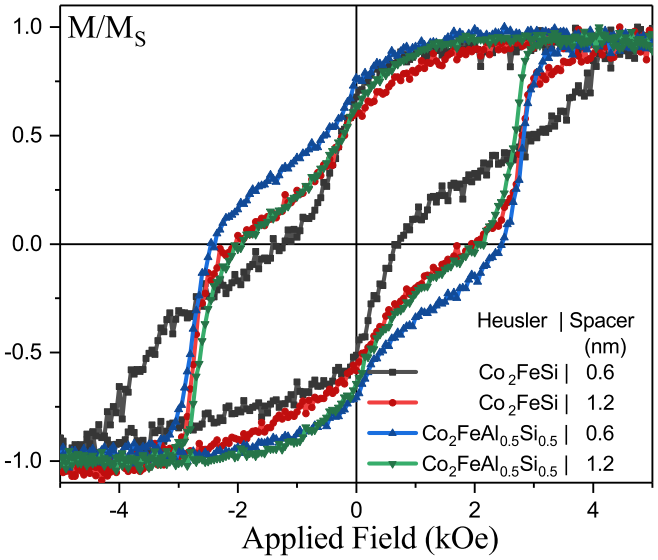

Figure 6.8: Out-of-plane *M-H* loops of multilayer films grown with varying spacer layer thicknesses for Co_2FeSi and $Co_2FeAl_{0.5}Si_{0.5}$.

Additionally the thickness of the tungsten spacer layer was doubled from the previous sample set to 1.2 nm, around the second antiferromagnetic coupling peak. In the samples with $Co_2FeAl_{0.5}Si_{0.5}$ magnetic layers this spacer layer thickness lead

Heusler Alloy	Spacer (nm)	M_S (emu/cm^3)
Co_2FeSi	0.6	230 ± 20
Co_2FeSi	1.2	300 ± 30
$Co_2FeAl_{0.5}Si_{0.5}$	0.6	550 ± 60
$Co_2FeAl_{0.5}Si_{0.5}$	1.2	600 ± 60

Table 6.1: The variation of magnetisation of Co_2FeSi and $Co_2FeAl_{0.5}Si_{0.5}$ multilayers with different tungsten spacer layer thicknesses.

to an increase of 50 emu/cm^3. This is most likely due to the 0.5 nm roughness of the film being on the same scale as the 0.6 nm thick layer. This prevents crystallisation of the tungsten encouraging intermixing and alloying at the tungsten-Heusler alloy interface. As such this thickness of 1.2 nm was used subsequently for GMR structures. This is similar to the thicknesses used in many GMR structures since the average thickness at which antiferromagnetic coupling is achieved through a transition metal is 1 nm [75]. However, in many GMR devices with spacer layers of silver, thicknesses of 3 nm to 5 nm are common [163, 164].

6.2.4 Post-annealing of W/$Co_2FeAl_{0.5}Si_{0.5}$/W/$Co_2FeAl_{0.5}Si_{0.5}$ Multilayers

The structure from section 6.2.2 with a 1.2 nm spacer layer of tungsten was deposited at room temperature to investigate the effects of thermal annealing post deposition. The Heusler alloy used was $Co_2FeAl_{0.5}Si_{0.5}$ due to the observed increase in M_S and layer thickness dependent switching.

Figure 6.9 shows the out-of-plane XRD spectra for the sample before and after annealing at 300 °C for one hour. In the as-deposited sample there is evidence of crystallisation in both layers from the W {110} and $Co_2FeAl_{0.5}Si_{0.5}$ {220} reflections. The peak at $2\theta = 35^o$ is not representative of any of the materials in the stack and may be due to intermixing or oxidation. Furthermore there is an offset of 0.48° in the position of the W {110} reflection from the bulk value indicated by the orange line. This indicates that there is a strain in the sample which increases the lattice parameter by 1% in the as-deposited state.

After annealing at 300 °C the relative intensity of the tungsten reflection doubles compared to the $Co_2FeAl_{0.5}Si_{0.5}$, indicating significant crystallisation. Fur-

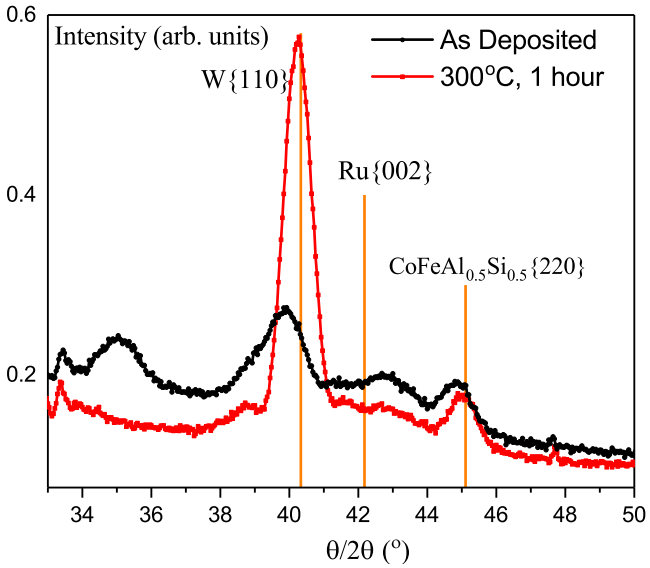

Figure 6.9: XRD spectra for a W/$Co_2FeAl_{0.5}Si_{0.5}$ multilayer deposited at room temperature and after annealing at 300 °C for one hour.

thermore the peak offset is removed, meaning that as crystallisation has occurred the lattice has also relaxed towards its bulk values. The crystallisation of the material is accompanied by an increase in the crystallite size from (6.2 ± 0.2) nm to (9.3 ± 0.2) nm. Additionally the extra peak in the spectrum is removed with annealing, indicating that it was caused by an anomalous phase in the material.

6.3 Low Temperature Deposition of W/$Co_2FeAl_{0.5}Si_{0.5}$ Layers

A lower initial temperature for deposition is desirable for efficiency and protection of device structures. A lower temperature should prevent the high levels of dispersion observed in the multilayers deposited at 400 °C, which reduced the values of M_S. Post-annealing of multilayer lead to little improvement in the crystallinity of the Heusler alloy layer. Therefore a high deposition energy provided for crystallisation may be a better alternative. Hence multilayers with the structure W (10 nm)/ $Co_2FeAl_{0.5}Si_{0.5}$ (12.5 nm)/W (1.2 nm)/$Co_2FeAl_{0.5}Si_{0.5}$ (2.5 nm)/Ru (3 nm) as in fig. 6.6 were deposited at range of initial substrate temperatures, T_S. The preheating was performed via a calibrated lamp behind the substrate immediately prior to opening of the deposition shutter.

Figure 6.10(a) shows the out-of-plane XRD spectra for samples with an increas-

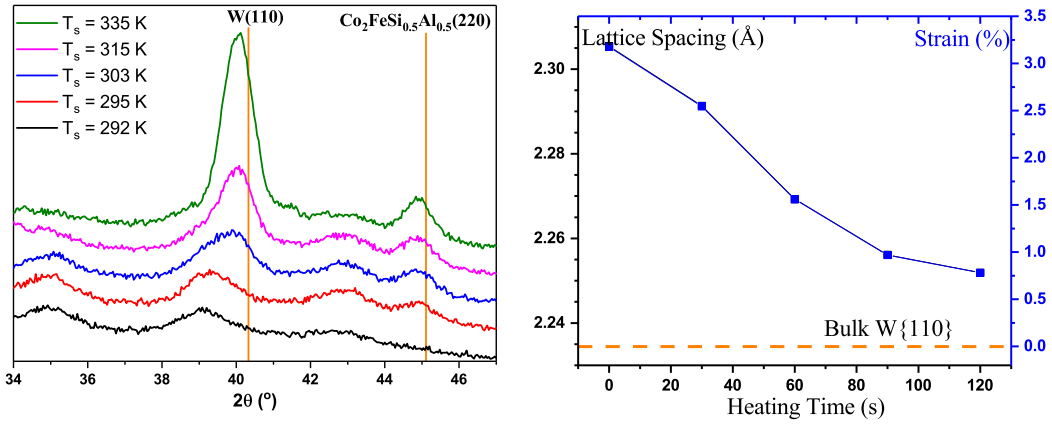

(a) (b)

Figure 6.10: (a) XRD spectra for a W/$Co_2FeAl_{0.5}Si_{0.5}$ multilayer deposited at increasing substrate temperature T_S and (b) the associated lattice relaxation of the tungsten layer.

ing substrate temperature T_S from 292 K to 335 K. In both the $Co_2FeAl_{0.5}Si_{0.5}$ and the tungsten seed layer there is a significant increase in the relative intensity of the reflection despite the low temperature, caused by an increase in crystallinity. This increase is larger in the tungsten layer at around five times, compared to only two times in the $Co_2FeAl_{0.5}Si_{0.5}$. This is accompanied by a relaxation of the tungsten lattice toward the bulk position shown in fig. 6.10(b). This distortion of the lattice is not seen in $2\theta_\chi$ measurements, meaning that the tungsten lattice is deposited with a tetragonal stretch out of plane. A higher deposition energy allows for this strain to relax.

The crystallite size can also be determined from Scherrer analysis of the seed layer and Heusler alloy reflections. In the tungsten layer there is an almost twofold increase in the crystallite size from (5.4 ± 0.2) nm to (9.2 ± 0.1) nm associated with the increased crystallinity. The $Co_2FeAl_{0.5}Si_{0.5}$ layer in the sample which was not heated is non-crystalline or nanocrystalline. However in the samples with T_S = 335 K a crystallite size of (7.9 ± 0.1) nm is obtained. This has significant effects on the magnetisation reversal as shown in fig. 6.11.

Firstly it is clear from fig. 6.11 that antiferromagnetic coupling is not achieved. Furthermore there is no evidence of any layer-thickness dependent switching. The nanocrystalline samples (T_S = <300 K) had very strong interganular coupling leading to a low H_C loop with a squareness of S =0.8. For samples deposited at higher temperatures 50% of the magnetisation reversal is through domain rotation and motion limited by strong pinning up to 1 kOe followed by a nucleation process. The degree of rotation is evidence of an increased anisotropy overcoming the inter-

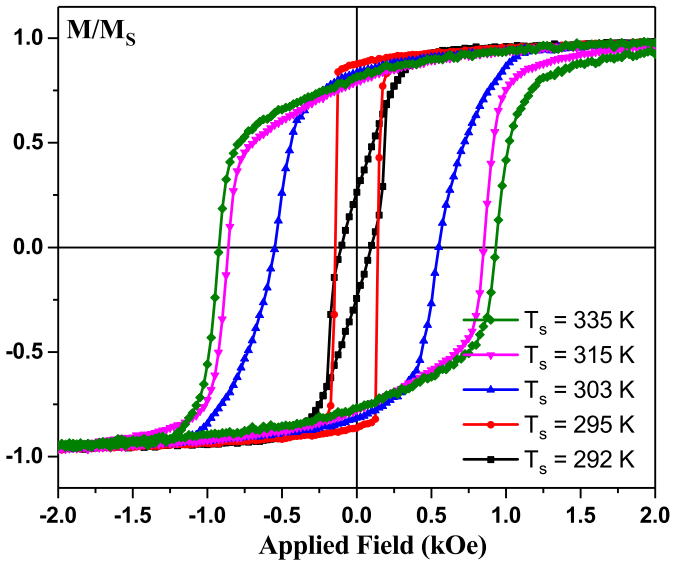

Figure 6.11: *M-H* loops for a W/$Co_2FeAl_{0.5}Si_{0.5}$ multilayer deposited at increasing substrate temperature T_S.

granular coupling energy while the increase in coercivity from 200 Oe to 1000 Oe is due to an increase in H_n from the increase in grain volumes.

The intergranular coupling energy is, however, still significant. This is confirmed by DCD and time dependence analysis as shown in fig. 6.12. Due to the intergranular coupling the field can only be measured as an applied field, so the DCD curve shown in fig. 6.12 is an effective one not the intrinsic. However by taking values for χ_{irrev} and the time dependence factor $S(H)$ at the remanent coercivity the demagnetising field can be ignored and the value for the of the effective diameter activation volume can be found to be $D_{eff} = (31 \pm 2)$ nm. This is four times the value of the crystallite size of 7.9 nm and as such strong intergranular exchange must be present in the film. This is why despite a large rotation in the magnetisation there is still a following rapid nucleation followed by domain wall motion for the remaining magnetisation reversal. The DCD curve also closely follows the magnetisation curve meaning that almost all of the magnetisation change is irreversible. This confirms the strong pinning contribution to the coercivity and level of curvature in th *M-H* loop.

The activation volumes for these materials can be determined using the waiting time method [70, 71]. By measuring at a constant magnetisation rather than field the demagnetising field is also constant. As such it can be ignored and a value for the activation volume obtained. This is further discussed in section 7.3.

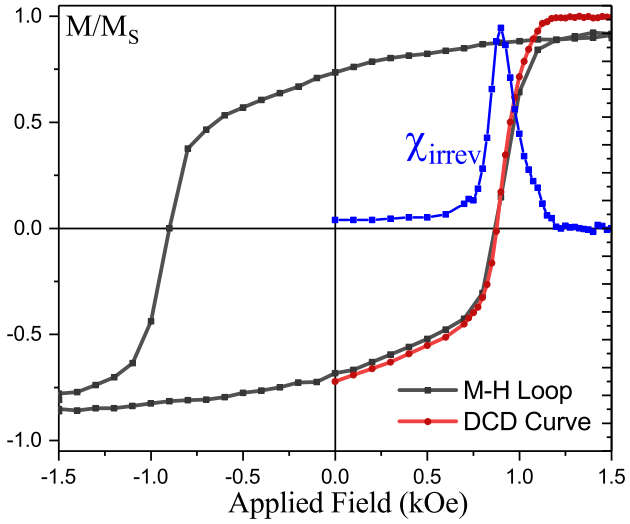

Figure 6.12: Effective DCD curve and the resultant χ_{irrev} for a sample deposited at T_S = 335 K with the out-of-plane *M-H* loop.

6.4 W/$Co_2FeAl_{0.5}Si_{0.5}$/Ag/$Co_2FeAl_{0.5}Si_{0.5}$ Thin Films and Devices

Since the mutilayer films in section 6.3 did not exhibit any layer-thickness dependent switching samples were deposited with 3 nm and 5 nm spacer layers of silver replacing the 1.2 nm tungsten spacer layer. These thicknesses are typical of optimised devices in previous work [21, 163, 164]. The maximum substrate temperature of T_S = 335 K was used to give the greatest coercivity in the thicker $Co_2FeAl_{0.5}Si_{0.5}$ layer which leads to a greater maximum coercivity difference between the two ferromagnetic layers. Figure 6.13 shows the out-of-plane *M-H* loops for the samples. Perpendicular anisotropy is maintained in the film despite the lack of a second interface with the tungsten in the 2.5 nm layer. However there is clear evidence of two individual switching regions for the two layer thicknesses with a clear switch at 500 Oe for the film with a 3 nm spacer layer and a nucleation at 1300 Oe for the sample with a 5 nm spacer.

The reversal in the sample with the 3 nm layer of silver is more appropriate for a device application due to the 50% greater value of squareness at $S_{3\text{ nm}} = 0.75$ compared to $S_{5\text{ nm}} = 0.5$. Secondly most of the rotation in the sample with the 5 nm spacer is indistinguishable between the two layers. The nucleation take place at a negative magnetisation and therefore there can be no antiparallel state near this rapid switch. As such a high GMR value would not be expected in a sample with this spacer layer and therefore the 3 nm thickness was used for devices.

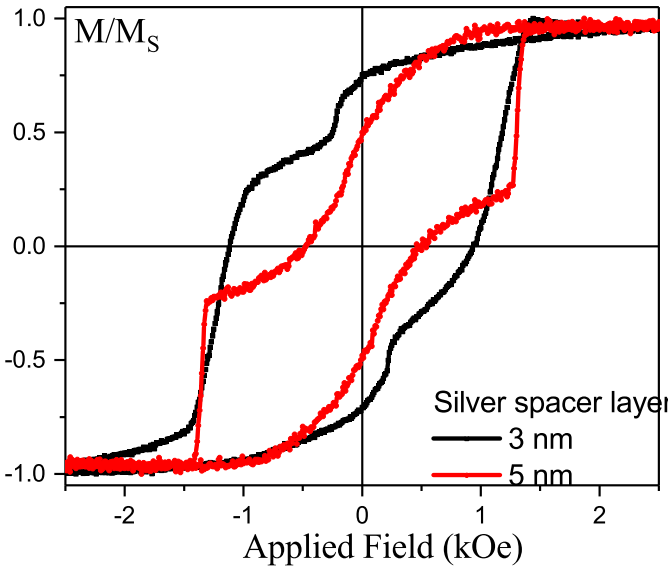

Figure 6.13: Out-of-plane *M-H* loops for a W/$Co_2FeAl_{0.5}Si_{0.5}$ multilayer with 3 nm and 5 nm spacer layers of silver.

Devices using this deposition temperature and structure were then deposited and patterned using the 3 nm silver spacer layer. The sizes of the patterned pillars varied from 1 µm by 0.5 µm down to 150 nm by 100 nm. Figure 6.14 shows the out-of-plane *MR*-curve for a sample with dimensions 1 µm by 0.5 µm. The switch corresponds perfectly to the *M-H* loop of the unpatterned film, with the maximum value of the resistance at 500 Oe. However the GMR value is extremely low at only 0.03%, independent of the size of the pillar.

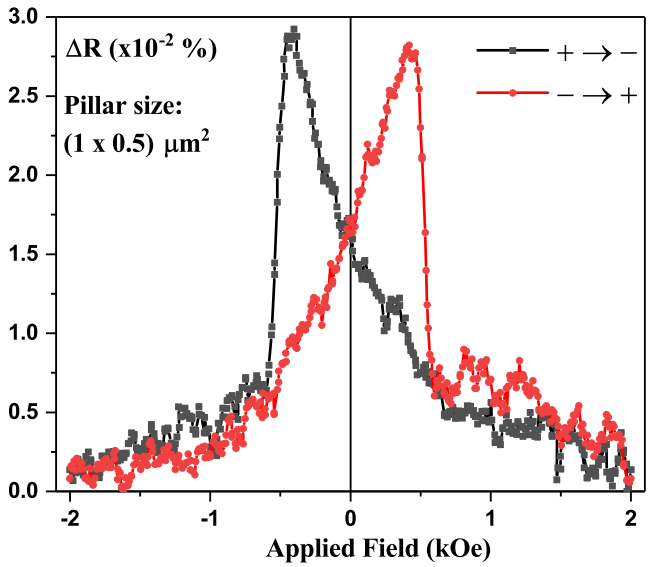

Figure 6.14: Out-of-plane *MR*-curve for a GMR device based on $Co_2FeAl_{0.5}Si_{0.5}$ with dimensions 1 µm by 0.5 µm.

There are several possible causes of the low GMR ratio. Firstly there is a rotation in the magnetisation of both layers before the nucleation reversal. This means

that no truly antiparallel state is achieved, creating a disproportionately low ΔR compared to the magnetisations of the layers. Secondly patterning may have damaged edges of the film, resulting in edge domains and a reduced magnetisation and therefore a low GMR.

Further post-annealing of the films did not improve the GMR ratio, in fact reducing it. Secondly there is a large decrease in the switching field observed in the *MR*-sweeps. These two effects are shown in fig. 6.15 after annealing at 350 °C for one hour. The GMR ratio has dropped by 100% and the switching field dropped to <150 Oe.

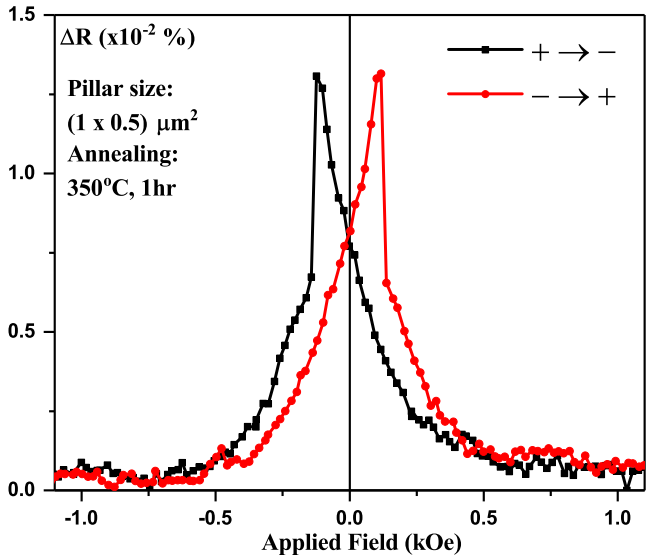

Figure 6.15: Out-of-plane *MR*-curve for a GMR device with dimensions 1 μm by 0.5 μm annealed at 350 °C for one hour.

The reduction in the sample properties could be due to intermixing between then layers creating low resistance paths through the pillar. The intermixing will also damage the magnetic ordering of the magnetic layers, decreasing the magnetisation and therefore the GMR ratio. Alternatively there could be oxidation of the ferromagnetic elemtns at the pillar edge where contact is made with Al_2O_3. This will cause a significant reduction in the GMR ratio due to reduction of the magnetisation. Furthermore the Heusler alloy films were not deposited in the ordered state. As such the half-metallicity of the structure is not realised meaning that the optimum potential of the GMR ratio is not reached.

While CPP-GMR devices with perpendicular anisotropy and operation can be created using Heusler alloy layers there is a requirement for further optimisation of the crystallographic properties. In spite of the anisotropy in the Heusler alloy layers the reduction in magnetisation and spin polarisation from the bulk limits the

potential of any GMR value. As such further work must be undertaken to improve the crystal order of the $Co_2FeAl_{0.5}Si_{0.5}$ layers whilst maintaining the perpendicular anisotropy achieved in this work.

7 Conclusion and Future Work

In chapter 1 it was discussed that the requirements for improved recording and memory densities in HDDs and MRAM are low *RA*, high MR devices with perpendicular anisotropy. In this project two distinct metallic seed layers, vanadium and tungsten, were used to try and induce these properties in Heusler alloy films. The conclusions of these two approaches are discussed in this order below.

7.1 Heusler Alloys with Vanadium Seed Layers

Polycrystalline vanadium layers can be grown with a strong {110} texture and a low roughness <0.5 nm at an optimised thickness of 25 nm. The addition of a chromium smoothing layer, which found great success when combined with silver seed layers, was found to prevent the formation of a textured vanadium film. The {110} texture of a vanadium seed layer was found to continue into a Co_2FeSi layer deposited on top. Annealing of this bilayer at a modest 300 °C was found to distinctly improve both the crystallinity and texture of both layers of the film.

Crystallographic analysis found that the properties of a 20 nm Co_2FeSi layer were strongly influenced by the vanadium layer, confirming its role as a seed. The texturing of the Co_2FeSi layer exactly matched that of the vanadium, and the crystallinity was also found to be directly related. Magnetically this lead to a large variability in the loop squareness of the samples, whereby the value of *S* decreased with the improved texture. However annealing of the very soft, textured samples leads to a square loop with a significant magnetisation of 860 emu/cm^3, 77% of the bulk value, but with no perpendicular magnetic anisotropy.

Variation in thickness of the Co_2FeSi layer lead to a large changes in the anisotropy of the sample, however the anisotropy of the Co_2FeSi layers remained in-plane.

Further reduction of the thickness of Co_2FeSi to 5 nm or less lead to evidence of some, but not dominant, perpendicular anisotropy in the samples which was most evident at a thickness of 4 nm. The anisotropy of the samples cannot be estimated due to the pinning and intergranular coupling in the films making any determination of H_K impossible. The increase in anisotropy was caused by the influence of strain at the interfaces have a greater effect in thinner films. The anisotropy was further increased by annealing the sample whereby the saturating field out-of-plane was reduced from 10 kOe to 4 kOe for a 5 nm film. The interfacial effects were further enhanced, and confirmed, by the addition of a second vanadium interface on top of the Co_2FeSi layer which lead to an increase in the perpendicular anisotropy of the Co_2FeSi and reducing the saturating field to 375 Oe.

As a result of this GMR stacks were deposited that had perpendicular anisotropy with layer thickness dependent switching, ideal for GMR application. The individual switching of layers does not require an antiferromagnet to achieve, leading to the possibility of GMR devices with a lower *RA* and cost. However the crystallisation of the Co_2FeSi is far from complete, with no evidence of the $L2_1$ phase which is required for the optimal GMR performance due to the 100% spin polarisation.

7.2 Heusler Alloys with Tungsten Seed Layers

High temperature deposition of tungsten creates a crystalline but 3D random film. When used as a seed layer for Co_2FeSi layers this promotes the crystallisation of the Heusler alloy even at a low thickness of 2.5 nm, equivalent to approximately 5 unit cells. A slight tetragonal distortion of the Heusler alloy leads to a strong perpendicular anisotropy, which is maintained in films with thicknesses up to 12.5 nm. Increased rotation, to over 50% of magnetisation, in the hysteresis loop indicates that the anisotropy energy is greater in thicker films, overcoming the intergranular exchange energy. However this is also due to a very high level of pinning strength and site number in the films.

The change in anisotropy with thickness in the Co_2FeSi layer allows for layer thickness dependent switching to occur in GMR stacks. As such, as in the vanadium seeded films, a GMR response whereby the layers can exhibit opposite magnetisations is possible without the presence of an antiferromagnetic layer. This effect is maximised by replacing the Co_2FeSi Heusler alloy with $Co_2FeAl_{0.5}Si_{0.5}$, a similar alloy with a lower crystallisation energy [168].

Lower temperature deposition of the tungsten seed layer also promotes crystallisation of both the seed layer and the $Co_2FeAl_{0.5}Si_{0.5}$. By heating the substrate to modest temperatures below 335 K before deposition a change from nanocrystalline to granular $Co_2FeAl_{0.5}Si_{0.5}$ takes place, with an increasing perpendicular anisotropy with temperature. However silver spacer layers must be used in combination with low temperature deposition to observe spin valve behaviour. This allows for devices with perpendicular anisotropy to exhibit giant magnetoresistance, albeit limited to 0.03%.

The results presented in this work show that perpendicular anisotropy can be achieved in Heusler alloys without the need for a MgO interface. CPP-GMR devices can be operated in a perpendicular orientation and spin valve behaviour observed without an antiferromagnetic pinning layer.

7.3 Future Work

In order to increase the GMR ratio in sputtered Heusler alloy devices with perpendicular anisotropy, further optimisation of the stack is required. Firstly a more thorough investigation with a wider range of deposition temperatures would possibly facilitate a greater degree of crystallisation in the Heusler alloy layer, increasing the magnetisation and therefore the MR. Furthermore this could promote the $L2_1$ or $B2$ structure in the Heusler layer which would improve the spin polarisation and therefore the GMR ratio would be further enhanced. Seed layer variation could also promote the growth of the {100} planes out-of-plane which will improve the spin polarisation compared to the {110} directions.

Since the origins of the anisotropy are interfacial in this work, further investigation could be carried out as to the effects of capping and spacer layers to enhance the anisotropy. This is especially true since effects such as enhanced GMR in Heusler alloy films with an iron insert layer have been observed [24] and the anisotropy of a p-MTJ is strongly affected by the capping layer [31]. Therefore variation of the metallic heavy layers as interface layers or insert layers could enhance the low GMR observed in this work. The capping layer or top interface is easily adapted and as such a simple avenue for improvement of anisotropy.

Alternative Heusler alloys, including recently suggested LiMgPdSn-type quaternary [? ?] or quinternary [?] pseudo-Heusler alloys, may lead to a greater

degree of crystallisation and/or magnetisation in the devices. Additionally a non-magnetic Heusler alloy could be used as a spacer layer in order to better match the electron energy levels throughout the CPP conduction. Furthermore antiferromagnetic Heusler alloys such as Ru_2MnGe could be incorporated into the stack for the formation of a pinned layer. Other Heusler-like Mn compounds have been the subject of interest due to versatile magnetic behaviour, such as ferro- or ferrimagnetic MnGa alloys [169**?**]. This would be of significant interest if the perpendicular anisotropy induced in the ferromagnetic Heusler alloys is obtained in an antiferromagnet or compensated ferrimagnet allowing for out-of-plane exchange bias devices.

Other alternatives are the popular materials MnN and Mn_3N, a very promising Heusler-like antiferromagnet [170]. However the thickness required is >30 nm which is very limiting for application, along with a high annealing or deposition temperature >400 °C.

There is therefore large scope for the optimisation of perpendicular CPP-GMR devices based Heusler alloys via the variation of materials and the refinement of crystallographic properties. Secondly the perpendicular anisotropy induced in the manner of this work could be used to enhance that anisotropy found in p-MTJs for application in TMR MRAM.

———————————————-

References

[1] W. Thomson, *Proc. R. Soc. London* **8**, 546 (1856).

[2] R. P. Hunt, *IEEE Trans. Magn.* **7**, 150 (1971).

[3] D. J. Mapps, *Sensors Actuators A* **59**, 9 (1997).

[4] M. J. Caruso, *Honeywell Inc.* (2010).

[5] C. Tsang, M. M. Chen, T. Yogi, K. Ju, *IEEE Trans. Magn.* **26**, 1689 (1990).

[6] C. Tsang, H. Santini, D. McCown, J. Lo, R. Lee, *IEEE Trans. Magn.* **32**, 7 (1996).

[7] C. Tsang, *et al.*, *IEEE Trans. Magn.* **33**, 2866 (1997).

[8] S. A. Wolf, *et al.*, Spintronics: A spin-based electronics vision for the future (2001).

[9] M. N. Baibich, *et al.*, *Phys. Rev. Lett.* **61**, 2472 (1988).

[10] P. Grünberg, *et al.*, *J. Appl. Phys.* **61**, 3750 (1987).

[11] B. Dieny, Giant magnetoresistance in spin-valve multilayers, *Tech. rep.* (1994).

[12] H. Kanai, *et al.*, *IEEE Trans. Magn.* **32**, 3368 (1996).

[13] S. S. Parkin, *et al.*, *Nat. Mater.* **3**, 862 (2004).

[14] Seagate Technology LLC, Seagate Reaches 1 Terabit Per Square Inch Milestone In Hard Drive Storage With New Technology Demonstration (2012).

[15] A. Hirohata, K. Takanashi, *J. Phys. D. Appl. Phys.* **47**, 193001 (2014).

[16] T. Graf, C. Felser, S. S. P. Parkin, *Prog. Solid State Chem.* **39**, 1 (2011).

[17] S. Wurmehl, *et al.*, *Phys. Rev. B* **72**, 184434 (2005).

[18] S. M. Thompson, *J. Phys. D. Appl. Phys.* **41**, 93001 (2008).

[19] I. Galanakis, P. Mavropoulos, P. H. Dederichs, *J. Phys. D. Appl. Phys.* **39**, 765 (2006).

[20] T. Iwase, *et al.*, *Appl. Phys. Express* **2**, 063003 (2009).

[21] T. Furubayashi, *et al.*, *Appl. Phys. Lett.* **93**, 122507 (2008).

[22] K. Suzuki, S. Matsui, Y. Ochiai, *Sub-Half-Micron Lithography for ULSIs* (Cambridge University Press, Cambridge, UK, 2000).

[23] J. Sagar, *et al.*, *IEEE Trans. Magn.* **48**, 4006 (2012).

[24] T. Kubota, Y. Ina, Z. Wen, K. Takanashi, *Materials (Basel).* **11** (2018).

[25] A. Hirohata, W. Frost, M. Samiepour, J.-Y. Kim, *Materials (Basel).* **11**, 105 (2018).

[26] T. Saito, N. Tezuka, S. Sugimoto, *Mater. Trans.* **52**, 370 (2011).

[27] Y. Cui, *et al.*, *Appl. Phys. Lett.* **102** (2013).

[28] H. Sukegawa, *et al.*, *Appl. Phys. Lett.* **110**, 112403 (2017).

[29] S. Ikeda, *et al.*, *Nat. Mater.* **9**, 721 (2010).

[30] S. Peng, *et al.*, *Sci. Rep.* **5**, 18173 (2015).

[31] Y.-W. Oh, K.-D. Lee, J.-R. Jeong, B.-G. Park, *J. Appl. Phys.* **115**, 17C724 (2014).

[32] R. Galceran, *et al.*, *Phys. Rev. B* **93**, 144417 (2016).

[33] I. Ikhtiar, *et al.*, *J. Appl. Phys.* (2014), vol. 115.

[34] A. Niesen, *et al.*, *J. Appl. Phys.* **118**, 243904 (2015).

[35] J. Jeong, *et al.*, *Nat. Commun.* **7**, 10276 (2016).

[36] S. Kämmerer, A. Thomas, A. Hütten, G. Reiss, *Appl. Phys. Lett.* **85**, 79 (2004).

[37] K. Nakajima, *et al.*, *J. Appl. Phys.* **97**, 10C904 (2005).

[38] W. Wang, *et al.*, *Phys. Rev. B* **71**, 1 (2005).

[39] Y. Nagamine, *et al.*, *Appl. Phys. Lett.* **89**, 162507 (2006).

[40] C. Rizal, E. E. Fullerton, *J. Phys. D. Appl. Phys.* **50** (2017).

[41] B. Dieny, M. Chshiev, *Rev. Mod. Phys.* **89** (2017).

[42] S. Husain, S. Akansel, A. Kumar, P. Svedlindh, S. Chaudhary, *Sci. Rep.* **6**, 28692 (2016).

[43] Y. Cao, *et al.*, *J. Magn. Magn. Mater.* **395**, 361 (2015).

[44] E. Stoner, E. Wohlfarth, *Phil. Trans. Roy.Soc.* **A-240**, 599 (1948).

[45] B. D. Cullity, C. D. Graham, *Introd. to Magn. Mater.* (Wiley, 2009), pp. 67–78, second edn.

[46] K. Krishnan, *Fundamentals and applications of magnetic materials* (Oxford University Press, Oxford, 2016), first edn.

[47] L. Néel, *J. Phys. le Radium* **11**, 49 (1950).

[48] C. P. Bean, J. D. Livingston, *J. Appl. Phys.* **301**, 120 (1959).

[49] R. Street, J. C. Woolley, P. B. Smith, *Proc. Phys. Soc. Sect. B* **65**, 679 (1952).

[50] S. Uren, K. O. Grady, R. W. Chantrelll, *Le J. Phys. Colloq.* **49**, 6 (1988).

[51] P. Gaunt, *J. Appl. Phys.* **591**, 245 (1986).

[52] M. El-Hilo, K. O 'Grady, R. W. Chantrell, D. P. E. Dickson, *J. Magn. Magn. Mater.* **123**, 30 (1993).

[53] M. El-Hilo, K. O'Grady, R. W. Chantrell, *J. Magn. Magn. Mater.* **109**, 164 (1992).

[54] R. Street, J. C. Woolley, *Proc. Phys. Soc. Sect. A* **62**, 562 (1949).

[55] S. Uren, M. Walker, K. O'Grady, R. W. Chantrell, *IEEE Trans. Magn.* **24**, 1808 (1988).

[56] L. Néel, *J. phys. radium* **12**, 339 (1951).

[57] E. Wohlfarth, *J. Phys. F Met. Phys.* **14**, L155 (1984).

[58] M. A. Ruderman, C. Kittel, *Phys. Rev.* **96**, 99 (1954).

[59] P. W. Anderson, *Phys. Rev.* **79**, 350 (1950).

[60] P. Dirac, *Roy. Soc. Proc* **112**, 661 (1926).

[61] W. Heisenberg, *Zeitschrift für Phys.* **38**, 411 (1926).

[62] L. Szunyogh, B. Lazarovits, L. Udvardi, J. Jackson, U. Nowak, *Phys. Rev. B - Condens. Matter Mater. Phys.* **79** (2009).

[63] B. D. Cullity, C. D. Graham, *Introd. to Magn. Mater.* (Wiley, 2009), pp. 197–239, second edn.

[64] F. Hellman, *et al.*, *Rev. Mod. Phys.* **89**, 025006 (2017).

[65] W. Yan, H. Wang, W. Du, J. Zhao, X. Zhang, *J. Phys. D Appl. Phys* **49**, 065005 (2016).

[66] M. Maret, M. Cadeville, W. Staiger, *Thin Solid Films* **275**, 224 (1996).

[67] H. Ju, B. Li, Z. Wu, F. Zhang, *Integr. Ferroelectr.* **160**, 153 (2015).

[68] L. Grenet, *et al.*, *ArXiv* p. 1110.2628v1 (2011).

[69] J. C. Read, P. M. Braganca, N. Robertson, J. R. Childress, *Appl. Phys. Lett. Mater.* **2**, 046109 (2014).

[70] M. El-Hilo, K. O'Grady, R. W. Chantrell, *J. Magn. Magn. Mater.* **248**, 360 (2002).

[71] J. D. Dutson, K. O'Grady, B. Lu, Y. Kubota, C. L. Platt, *IEEE Trans. Magn.* **39**, 2344 (2003).

[72] A. P. Ramirez, *J. Phys. Condens. Matter* **9**, 8171 (1997).

[73] S. Solin, T. Thio, D. Hines, J. Heremans, *Science* **289**, 1530 (2000).

[74] P. Wiśniewski, *Appl. Phys. Lett.* **90**, 192106 (2007).

[75] S. S. P. Parkin, *Phys. Rev. Lett.* **67**, 3598 (1991).

[76] C. Felser, A. Hirohata, eds., *Heusler Alloys*, vol. 222 of *Springer Series in Materials Science* (Springer International Publishing, Switzerland, 2016).

[77] M. Julliere, *Phys. Lett. A* **54**, 225 (1975).

[78] T. Miyazaki, N. Tezuka, Giant magnetic tunneling effect in Fe/Al2O3/Fe junction (1995).

[79] J. S. Moodera, L. R. Kinder, T. M. Wong, R. Meservey, *Phys. Rev. Lett.* **74**, 3273 (1995).

[80] S. Yuasa, T. Nagahama, A. Fukushima, Y. Suzuki, K. Ando, *Nat. Mater.* **3**, 868 (2004).

[81] S. Ikeda, *et al.*, *Appl. Phys. Lett.* **93**, 082508 (2008).

[82] W. H. Butler, X.-G. Zhang, T. C. Schulthess, J. M. Maclaren, *Phys. Rev. B* **63**, 054416 (2001).

[83] J. Mathon, A. Umerski, *Phys. Rev. B* **63**, 220403 (2001).

[84] F. Heusler, *Verhandlungen der Dtsch. Phys. Gesellschaft* **12**, 219 (1903).

[85] T. M. Nakatani, *et al.*, *J. Appl. Phys.* **102**, 033916 (2007).

[86] A. K. Nayak, *et al.*, *Nat. Mater.* **14**, 3 (2015).

[87] G. Y. Gao, K. L. Yao, *Appl. Phys. Lett.* **103** (2013).

[88] H. Van Leuken, R. A. De Groot, *Phys. Rev. Lett.* **74**, 1171 (1995).

[89] C. Felser, L. Wollmann, S. Chadov, G. H. Fecher, S. S. P. Parkin, *APL Mater.* **3** (2015).

[90] M. J. Otto, A. M. Van Woerden, P. J. Van Der Valk, G. E. Bacon, J. S. Plantt, *J. Phys. F Met. Phys.* **1** (1971).

[91] K. H. J. Buschow, P. G. van Engen, *J. Magn. Magn. Mater.* **25**, 90 (1981).

[92] H. Schneider, *et al.*, *Phys. Rev. B* **74**, 174426 (2006).

[93] H. C. Kandpal, G. H. Fecher, C. Felser, *J. Phys. D. Appl. Phys.* **40**, 1507 (2007).

[94] I. Galanakis, E. Şaşoğlu, *J. Appl. Phys.* **109** (2011).

[95] W. Zhu, B. Sinkovic, E. Vescovo, C. Tanaka, J. S. Moodera, *Phys. Rev. B - Condens. Matter Mater. Phys.* **64**, 604031 (2001).

[96] B. Zhang, *et al.*, *Phys. Rev. B - Condens. Matter Mater. Phys.* **88**, 014418 (2013).

[97] I. Galanakis, *New Dev. Ferromagn. Res.*, V. Murray, ed. (Nova Science Publishers, 2006), chap. 3, p. 83.

[98] I. Joffe, R. Heuberger, *Philos. Mag.* **29**, 1051 (1974).

[99] M. Walker, P. I. Mayo, K. Ogrady, S. W. Charles, R. W. Chantrell, *J. Physics-Condensed Matter* **5**, 2779 (1993).

[100] K. Munira, J. Romero, W. H. Butler, *J. Appl. Phys.* **115**, 17B731 (2014).

[101] H. Pandey, *et al.*, *Appl. Phys. Lett.* **104**, 022402 (2014).

[102] M. S. Gabor, T. Petrisor, C. Tiusan, M. Hehn, T. Petrisor, *Phys. Rev. B - Condens. Matter Mater. Phys.* **84** (2011).

[103] W. Frost, A. Hirohata, *IEEE Trans. Magn.* **52**, 2 (2016).

[104] J. Sagar, *et al.*, *Appl. Phys. Lett.* **105** (2014).

[105] J. Sagar, C. N. Yu, L. Lari, A. Hirohata, *J. Phys. D. Appl. Phys.* **47**, 265002 (2014).

[106] N. P. Aley, K. O'Grady, *J. Appl. Phys.* **109**, 07D719 (2011).

[107] M. Tsunoda, K. ichi Imakita, M. Naka, M. Takahashi, *J. Magn. Magn. Mater.* **304**, 55 (2006).

[108] N. P. Aley, *et al.*, *IEEE Trans. Magn.* (2008), vol. 44, pp. 2820–2823.

[109] K. Elphick, G. Vallejo-Fernandez, T. J. Klemmer, J. U. Thiele, K. O'Grady, *Appl. Phys. Lett.* **109**, 052402 (2016).

[110] J. Y. Chen, N. Thiyagarajah, H. J. Xu, J. M. D. Coey, *Appl. Phys. Lett.* **104**, 152405 (2014).

[111] Y. Sonobe, *et al.*, *J. Magn. Magn. Mater.* **303**, 292 (2006).

[112] B. A. Joyce, *Reports Prog. Phys.* **48**, 1637 (1985).

[113] A. Y. Cho, J. R. Arthur, *Prog. Solid State Chem.* **10**, 157 (1975).

[114] R. W. Johnson, A. Hultqvist, S. F. Bent, *Mater. Today* **17**, 236 (2014).

[115] P. R. Willmott, J. R. Huber, *Rev. Mod. Phys.* **72**, 315 (2000).

[116] M. N. R. Ashfold, F. Claeyssens, G. M. Fuge, S. J. Henley, *Chem. Soc. Rev.* **33**, 23 (2004).

[117] C. Mix, G. Jakob, *J. Appl. Phys.* **113**, 17 (2013).

[118] C. Mix, *et al.*, *J. Appl. Phys.* **115**, 193901 (2014).

[119] M. Vopsaroiu, M. J. Thwaites, S. Rand, P. J. Grundy, K. O'Grady, *IEEE Trans. Magn.* **40**, 2443 (2004).

[120] G. Betz, IUCr, *Acta Crystallogr. Sect. A* **38**, 399 (1982).

[121] P. J. Kelly, R. D. Arnell, *Vacuum* **56**, 159 (2000).

[122] Y. Sonobe, *et al.*, *J. Magn. Magn. Mater.* **235**, 424 (2001).

[123] J. Chureemart, *Ph.D. Thesis, Univ. York* p. 111 (2013).

[124] K. Wasa, *Handb. Sputter Depos. Technol. Fundam. Appl. Funct. Thin Film. Nano-Materials MEMS Second Ed.* (William Andrew, 2012), pp. 77–139.

[125] J. S. Colligon, *J. Vac. Sci. Technol. A Vacuum, Surfaces, Film.* **13**, 1649 (1995).

[126] S. Rossnagel, J. Cuomo, *Vacuum* **38**, 73 (1988).

[127] F. Adibi, *et al.*, *J. Appl. Phys.* **73** (1993).

[128] M. Thwaites, High Density Plasma UK Patent GB 2 343 992 B (2001).

[129] Y. K. Bu, *et al.*, *Seventh Int. Conf. Thin Film Phys. Appl.* **7995**, 79952H (2010).

[130] M. Vopsaroiu, *et al.*, *J. Optoelectron. Adv. Mater.* **7**, 2713 (2005).

[131] J. W. Dini, *Mater. Manuf. Process.* **12**, 437 (1997).

[132] J. Singh, D. E. Wolfe, *J. Mater. Sci.* **40**, 1 (2005).

[133] K. Suzuki, B. W. Smith, *Microlithography : science and technology* (CRC Press, 2007).

[134] B. D. Cullity, S. R. Stock, *Elements of X-Ray Diffraction* (Prentice Hall, 2001).

[135] K. Inaba, *Rigaku J.* **24**, 10 (2008).

[136] T. Mitsunaga, *Rigaku J.* **25**, 7 (2009).

[137] T. Konya, *Rigaku J.* **25**, 1 (2009).

[138] S. Kobayashi, *Rigaku J.* **26**, 3 (2010).

[139] M. Yasaka, *Rigaku J.* **26**, 1 (2010).

[140] A. Ogi, K. Inaba, *Rigaku J.* **27**, 1 (2011).

[141] K. Nagao, E. Kagami, *Rigaku J.* **27**, 6 (2011).

[142] S. Kobayashi, K. Inaba, *Rigaku J.* **28**, 8 (2012).

[143] D. B. Williams, C. B. Carter, *Transmission Electron Microscopy* (Springer International Publishing, 2009), second edn.

[144] W. H. Bragg, W. L. Bragg, *Proc. R. Soc. A Math. Phys. Eng. Sci.* **88**, 428 (1913).

[145] B. D. Cullity, S. R. Stock, *Elements of X-Ray Diffraction* (Prentice Hall, 2001), third edn.

[146] Intelligent X-ray diffraction (XRD) system | Rigaku.

[147] Rigaku, RIGAKU GlobalFit - Integrated thin film analysis software (2010).

[148] M. Björck, G. Andersson, *J. Appl. Crystallogr.* **40**, 1174 (2007).

[149] M. Björck, G. Andersson, GenX (2018).

[150] S. Foner, *Rev. Sci. Instrum.* **301** (1959).

[151] E. O. Samwel, T. Bolhuis, J. C. Lodder, *Rev. Sci. Instrum.* **69**, 1344 (1998).

[152] P. J. Flanders, *J. Appl. Phys.* **63**, 5262 (1988).

[153] R. Reevest, *Physics (College. Park. Md).* **5**, 547 (1972).

[154] K. O 'Grady, V. G. Lewis, D. P. E. Dickson, R. Goldfarb, *J. Appl. Phys.* **731**, 15110 (1993).

[155] B. Marchon, T. Pitchford, Y.-T. Hsia, S. Gangopadhyay, *Adv. Tribol.* **2013**, 1 (2013).

[156] Z. J. Zhou, *Handb. Microsc. Nanotechnol.* (Kluwer Academic Publishers, Boston, 2005), pp. 287–321.

[157] U. Geiersbach, A. Bergmann, K. Westerholt, *Thin Solid Films* **425**, 225 (2003).

[158] M. Belmeguenai, *et al.*, *Phys. Status Solidi Appl. Mater. Sci.* **209**, 1 (2012).

[159] S. Kämmerer, *et al.*, *J. Appl. Phys.* (2003), vol. 93, pp. 7945–7947.

[160] B. Rameev, *et al.*, *Phys. Status Solidi Appl. Mater. Sci.* **203**, 1503 (2006).

[161] Y. Takamura, T. Suzuki, Y. Fujino, S. Nakagawa, *J. Appl. Phys.* **115**, 7 (2014).

[162] B. M. Ludbrook, B. J. Ruck, S. Granville, *Appl. Phys. Lett.* **110**, 62408 (2017).

[163] Y. Sakuraba, M. Ueda, S. Bosu, K. Saito, K. Takanashi, *J. Magn. Soc. Japan* **38**, 45 (2014).

[164] Z. Diao, *et al.*, *J. Magn. Magn. Mater.* **356**, 73 (2014).

[165] R. A. Serway, *Principles of physics* (Saunders College Pub, 1998).

[166] W. D. Jung, F. A. Schmidt, G. C. Danielson, *Phys. Rev. B* **15**, 659 (1977).

[167] J. Sagar, L. R. Fleet, A. Hirohata, K. O'Grady, *IEEE Trans. Magn.* (2011), vol. 47, pp. 2440–2443.

[168] N. G. Szwacki, J. A. Majewski, *J. Magn. Magn. Mater.* **409**, 62 (2016).

[169] S. Mizukami, *et al.*, *Phys. Rev. B - Condens. Matter Mater. Phys.* **85** (2012).

[170] M. Dunz, J. Schmalhorst, M. Meinert, *AIP Adv.* **8**, 56304 (2018).